DOCTORAL THESIS

1993:129 D

DIVISION OF STRUCTURAL ENGINEERING

ISSN 0348 – 8373

ISRN: HLU - TH - T - - 1993 - 129 - D - - SE

TENSILE FRACTURE OF ICE

Test methods and fracture mechanics analysis

LARS STEHN

TEKNISKA HÖGSKOLAN I LULEÅ

LULEÅ UNIVERSITY OF TECHNOLOGY

Page/Position	Thesis text	Should be
p.63/2nd para., row 19	...on the *SRCN* specimen.	...on the *SRCN* specimen, see Figure 3.5(c).
p.73/top	**Fracture geomeries**	**Fracture geometries**
p.77/middle	**The Cevron...**	**The Chevron...**
p.84/2nd para., row2	$(\alpha_o^{SCB} \leq \alpha^{SCB} \leq 1)$	$(0 \leq \alpha^{SCB} \leq 1)$
p.87/2nd para., row 7	microstructual	microstructural
p.89/1st para., row5	eleven	seven
p.89/3rd para., row 6	microstrucural	microstructural
p.97/3rd para., row 8	...next sections will...	...next paragraphs will...
p.97/4th para., row 9	crack front can...	crack front width can...
p.104/3rd para., row 9	Similar theoretical predictions ...	By the same arguments as before (Figure 5.3) similar theoretical predictions of the fracturing behavior of the *CNT* can be made from the *GSF* plot shown in Figure 5.4.
p.117/3rd para., row 16	Formar	Formvar
p.126/5th para., row 2	layerd	layered
p.126/6th para., row 2	*Structtures*	*Structures*
p.127/4th para., row 2	om	of
p.127/5th para., row 1	Dempsy	Dempsey
p.130/6th para., row 2	*Canadien*	*Canadian*

ERRATA

Page/Position	Thesis text	Should be
p.iv/2nd para., row 6	Researcg	Research
	Nooo14-...	N00014-...
p.iv/2nd para., row 10	whises	wishes
p.v/2nd para., row 2	whos	whose
p.vii/1st para., row 7	dicipline	discipline
p.3/1st para., row 15	...of ice fracturing when.	...of ice fracturing.
p.5/1st para., row 8	Stehn et al., 1993	Stehn et al., 1993b
p.11, 45, 67, 91	S–951 87...	S–971 87...
p.16/1st para., row 10	enery	energy
p.21/3rd para., row 3	favourable	favorable
p.21/4rd para., row 6	batterys	batteries
p.30/Equation 2.11	$\frac{W^2}{G}\frac{\partial G}{\partial A} \geq$...	$\frac{W^2}{G}\frac{\partial G}{\partial A} =$...
p.31/footnote 4, row 2	...crack growth stability as...	...crack growth stability for specimens with negative *gsf*s as...
p.39/Figure 2.11(b)	$\beta_f = 1.06$	$\beta_f = 0.441$
	$\beta_f = 0.3$	$\beta_f = 0.15$
	$\beta_f = 0.1$	$\beta_f = 0.05$
p.41/2nd para., row7	...*FIFT* on *PMMA RTCLWL*...	...*FIFT* on *PMMA RT*...
p.48/1st para., row 4	Hovewer	However
p.49/2nd para., row 6	polypropelene	*PMMA*
p.53/Equation 3.5	$G_I = \frac{F^2}{2h}$...	$G_I = \frac{F^2}{2t}$...
p.58/middle	**Result**...	**Results**...
p.63/1st para., row 8	vesion	version
p.63/1st para., row 21	occuring	occurring

DOCTORAL THESIS 1993:129 D

TENSILE FRACTURE OF ICE

Test Methods and Fracture Mechanics Analysis

by

Lars Stehn

Department of Civil and Mining Engineering
Division of Structural Engineering
Luleå University of Technology
S–971 87 Luleå
Sweden

September 1993

Preface

The work presented in this thesis has been carried out between 1988 to 1993 at the Division of Structural Engineering, Luleå University of Technology and from January to May 1992 at the Department of Civil and Environmental Engineering, Clarkson University, USA.

This doctoral thesis comprises an introductory part and four parts based on papers which have been accepted or submitted for publication in different international journals. The four papers are

Paper A: Stehn L., 1993. Fracture toughness and crack growth of brackish ice using chevron notched specimens, *Journal of Glaciology*, (accepted for publication).

Paper B: Stehn L.M., DeFranco S.J. and Dempsey J.P. Specimen geometry effects on the fracture of warm pond (S1) ice, *ASCE Journal of Engineering Mechanics*, (submitted for publication)

Paper C: Stehn L.M., DeFranco S.J. and Dempsey J.P. Orientation effects on the fracture of pond (S1) ice, *International Journal of Rock Mechanics and Mining Science & Geomechanics Abstracts*, (submitted for publication)

Paper D: Stehn L.M., DeFranco S.J. and Dempsey J.P. Fracture resistance determination of freshwater ice using a chevron notched tension specimen, *International Journal of Fracture*, (submitted for publication)

The work has received financial support in several different projects, each project or combination of projects is represented by the four papers. Also, several colleagues have supported me in different ways in these projects. Thus, I am glad to acknowledge the financial and personal support given in:

Paper A. This research was supported by the Swedish National Industrial board (SIND), Coldtech, the Swedish Council for Building Research (BFR), the Research Council of Norrbotten (Norrbottens Forskningsråd) and Skanska AB.

I want to thank Dr. Finn Ouchterlony at the Swedish Detonic Research Foundation for his help with the experimental compliance calibration and discussions concerning basic theoretical fracture mechanics evaluations and Dr. Bruce Parsons at IMD, National Research Council Canada, New Foundland, for the discussions concerning *stable* crack growth and crack velocity.

Papers B, C and D. The experiments reported in these papers were conducted at Ice Mechanics Research Laboratory at Clarkson University. This research was supported in part by the U.S. National Science Foundation [Grant No. MSS-90-07921], the U.S. Office of Naval Research through its Sea Ice Mechanics Accelerated Researcg Initiative [Grant No. Nooo14-90-J-1360], Coldtech (Sweden), the Research Council of Norrbotten (Norrbottens Forskningsråd, Sweden) and the Swedish Council for Building Research (BFR) respectively.

The author whises to thank Mr. Jose Lazo for his assistance with the experimental parts of these studies and Lic. Tech. Mikael Nyström for his help with the 3–D FE meshing.

Many people have helped me with this work over the years; I am especially grateful for the skillful help of Dr. Thomas Olofsson, Lic. Tech. Per Anders Daerga and Lab. Eng. Lars Åström all at the Division of Structural Engineering, Luleå University of Technology. Furthermore, I appreciate the friendly and professional atmosphere created by friends and colleagues at the Division of Structural Engineering, Division of Steel Structures and Division of Structural Mechanics.

There are also several persons who have contributed in a more personal way to the creation of this thesis. All have supported me in different ways and during different periods of the research process. Specifically I want to thank: **Professor Lennart Elfgren** my supervisor and head of the Division of Structural Engineering, Luleå University of Technology, for his moral support and for giving me the possibility to conduct my research in an independent way; **Dr. Lennart Fransson** at the Division of Structural Engineering, Luleå University of Technology, who initiated this work in 1988 and

since then has supported me during the whole course of my research. Most of all I appreciate his never ending enthusiasm and inspiration; **Professor John Dempsey** at the Department of Civil and Environmental Engineering, Clarkson University, USA, for inviting me to join his research group–without him I would never have come this far, at least not yet–and for all interesting and educative discussions on the topic on fracture of ice; **Dr. Sam DeFranco** at the Department of Civil and Environmental Engineering, Clarkson University, USA (now at Offshore, Arctic and Facilities Technologies, Amoco Production Company, OK, USA) for his *invaluable* help with the experiments, his stirring enthusiasm for ice research and for the continued fruitful discussions we have had since I left Clarkson.

Last, but not least, I want to thank my beloved wife **Katarina** without whos *absolute* and *encouraging* support my work would never have been completed. Not only did she put everything else aside (a new house, an interesting job, friends) to accompany me to USA with our two baby daughters but she has also been *very* patient about my periods of mental absence during these years.

Luleå, September 1993

Lars Stehn

Abstract

This thesis is concerned with several aspects of fracture of both brackish (low salinity) sea ice and freshwater ice. The tests and analyses are confined to tensile, or in fracture mechanics language, *Mode I*, fracture. A large part of this thesis is dedicated to demonstrate that Linear Elastic Fracture Mechanics (*LEFM*) can be applicable on ice by laboratory and in–situ tests of defined specimens. All interpretations are made using the dicipline of *LEFM*.

First, the development of a field test equipment called the *FIFT* (a Field Instrument for Fracture toughness Tests on ice) is described. The *FIFT* is used in both field and laboratory fracture toughness tests on brackish sea ice from the Gulf of Bothnia to describe porosity effects on the apparent fracture toughness, K_Q, and estimate crack velocities. An appropriate specimen size, in terms of notch sensitivity, is then provided valid for grain sizes ranging from 1.6 to nearly 100 mm.

An augmented use of the *FIFT* is then described where fracture toughness tests are performed on S1 type freshwater ice to investigate if similarities exist in the local K_I fields for three different fracture geometries. The results indicate that, under comparable conditions, K_Q is similar for all of the geometries. However, the type of specimen, has a marked influence on the character of the fracture surface.

Then, the influence of structural anisotropy on the fracture toughness of S1 ice is investigated by fabricating and testing three different fracture geometries from a single ice core. This approach is suitable for both field and, as in this work, laboratory studies. There is a wide scatter in the K_Q values. Possible explanations to the results are discussed in terms of the microstructural influences and specimen size effects.

Finally, crack growth resistance measurements on large grained S1 ice is conducted. A new fracture geometry is used which is found to be extremely favorable of promoting stable, *stick–slip*, crack growth over a large portion of the uncracked ligament. Now, a complete characterization of the fracture resistance curve is therefore possible. A negative fracture resistance K_R–curve is evaluated for the S1 ice at -16°C.

Contents

Chapter 1

Introduction

The behavior of ice when under stress is an important subject for an engineer. Fixed or mobile structures in cold regions must often be designed to withstand forces that are exerted by ice. Sometimes, also the bearing capacity of floating ice covers is used for transportation purposes for example as winter roads. During an ice/structure interaction several ice failure mechanisms are possible. The ice can fail by a continuum mode of failure (elastic buckling, creep buckling or ductile indentation) or by a fracture mode of failure (crushing, spalling, radial or circumferential cracking). This wide range of behaviors complicates the prediction of ice forces. Field observations show that fracturing of ice caused by environmental forces or interactions with a stationary structure is extensive. Ice around an offshore structure often presents a chaotic picture of multifariously fractured sheets and blocks. An icebreaker passing through an ice sheet also causes a great deal of ice fracturing when. In these cases, fracture appears to be the dominant failure mode in nature. There is very little apparent evidence of continuum deformations. They do exist but are not the norm. Global splitting or fracture has been proposed as a possible load limiting process (Blanchet, 1990). However, the conditions under which fracture events occur have not been well defined and the influence of variations in fracture toughness, tensile strength and the geometrical size scale needs to be addressed. Scale effects also make it difficult to extrapolate laboratory experiments to the full-scale case. Practical applications of fracture mechanics to the study of failure of ice makes it possible

to incorporate the effects of fracturing into ice load calculations. It also provides parameters for both the classification and the description of the mechanical behavior of ice.

A growing number of measurements on the fracture toughness of ice is reported in the literature. Recent reviews are found in Dempsey (1989), Dempsey et al. (1992), Parsons (1990) and Stehn (1990). Materials such as concrete, rock, ceramics and ice have an aggregate or grain size that is several orders of magnitude larger than typical metals. Because of this inhomogeneity, these materials do not strictly meet the assumptions of continuum mechanics in the sense that a suitable large specimen size must be tested in order that to mobilize polycrystallinity. However, many previous fracture toughness investigations adopt the discipline of Linear Elastic Fracture Mechanics (*LEFM*) without ensuring that the conditions of small–scale yielding are fulfilled, ASTM E-399 (1985). Based on crack length and specimen size considerations, Dempsey (1989) and Dempsey et al. (1992) *suggest* that almost all previous fracture tests on freshwater columnar ice have used sub-sized specimens. Only a few investigators have used a sufficiently sharp crack with large enough crack length to get reliable tests, i.e., tests that are notch sensitive. However, based on a similar notch sensitivity study, Parsons et al. (1993) concludes that the earlier tests were valid. The question is still open.

The survey of previous fracture toughness tests on both freshwater and sea ice shows considerable scatter in the reported data. Meaningful comparisons are hard to make because of the different test methods and ice types used. A certain amount of scatter in the results is expected since different loading rates, temperatures, grain sizes and crack orientations were used. In addition, the results are influenced by the methods, or lack of methods, used to fabricate and sharpen the cracks. Early studies often measured values aiming to determine the effect of loading rate, temperature, anisotropy and porosity on the fracture toughness. Lately, more concern has been directed towards determining whether or not *LEFM* can be applied to ice, both as a tool in evaluating toughness values from different fracture specimens and to calculate loads in ice/structure interaction models. To date, the emphasis has been on determining

the fracture toughness corresponding to the initiation of a stationary macrocrack. For toughness tests not considering crack growth stability, only the determination of K_{Ic} (the plane strain fracture toughness) is possible. The physical mechanisms of cracking in ice, crack stability and crack growth in ice have received attention only recently (Dempsey et al., 1986; Bentley, 1988; Parsons et al., 1988 and 1989; DeFranco and Dempsey, 1990, 1991 and 1993; Stehn, 1993 and Stehn et al., 1993). The following conclusions can be made:

- The *LEFM* approach is valid provided that three essential conditions are met; (A) the crack tip is sharp; (B) the crack length is large in comparison with the grain size (polycrystallinity); and (C) the specimen size (width, crack length and uncracked ligament) is sufficiently large in comparison to the crack tip process zone for the stress and deformation fields surrounding the crack to be grossly elastic.

- The precise meaning of the plane strain critical stress intensity factor, K_{Ic}, is only defined for metallic materials in the ASTM E399 (1985). No such standard exists for ice and most of the criteria of validity are unrealistic. Due to this lack of a fracture toughness testing standard for ice, the notation K_Q should be used to denote an apparent fracture toughness value, to symbolically represent the inherent assumptions involved. According to Dempsey et al. (1988)

$$K_Q = K(a_e, \rho, F_Q) \tag{1.1}$$

  where a_e is the effective crack length, ρ is the fabricated crack–tip radius and F_Q the failure load. The notation in equation (1.1) has long been used in the fracture toughness testing of rock, e.g., Ouchterlony (1982).

- In some cases during an ice/structure interaction, a limited amount of slow crack growth may occur under increasing load. This is followed by unstable crack propagation and a dramatic drop in the ice load on the structure. This type of fracture

cannot be quantified solely by K_{Ic}; instead, a different approach based on the energy absorption capability of ice with crack growth is necessary (DeFranco and Dempsey, 1993). Therefore, it is apparent, that a methodical investigation of fracture resistance behavior of ice is needed.

- Before fracture mechanics can be safely applied to ice engineering problems, further basic understanding of the material behavior of both freshwater and sea ice is needed. Ice is ideal for performing in-situ fracture experiments due primarily to its availability and low fracture toughness compared to concrete or metals. This permits the use of portable loading systems capable of providing sufficient failure loads. An immediate consequence is the possibility to experimentally verify full-scale fracture loads based on laboratory size effect tests.

This thesis is concerned with several aspects of fracture of both brackish (low salinity) sea ice and freshwater ice. Referring to the title *Tensile fracture of ice: Test methods and fracture mechanics analysis*, the tests and analyses are confined to the case of tensile, or in fracture mechanics language, *Mode I*, fracture. This mode is the simplest case of fracture but probably the most common in nature. Laboratory and in–situ tests were conducted on defined specimens. All interpretations are made using linear elastic fracture mechanics. Therefore, a large part of this thesis is assigned to demonstrate that *LEFM* can be applicable on ice.

Chapter 2 presents a field test equipment called *FIFT* (a Field Instrument for Fracture toughness Tests on ice). The use of the short rod chevron notched specimen is evaluated and the necessary requirements for a valid *LEFM* measurement are described. Special attention is directed to the effect of porosity on the apparent fracture toughness and on the stability of crack growth in brackish ice. An augmented use of the *FIFT* is described in **Chapter 3** where, again, aspects of *LEFM* are examined. To jointly combine a small-scale investigation with an on–going large–scale field program, experiments were performed on freshwater ice to investigate if similarities exist in the local K_I fields for three different

fracture geometries. Of real importance to field studies is the development of a reliable fracture measuring methodology. This will be addressed in **Chapter 4** where the effect of anisotropy on the fracture of freshwater ice using core specimens are described. Finally, in **Chapter 5** a new and stable fracture geometry is developed and crack growth resistance, K_R–curves, for freshwater ice are presented. The issue of stability is again addressed whence it can be concluded that stable cracking in cold large grained freshwater ice occur incrementally by so called *stick–slip* cracking.

1.1 Properties of ice

Ice forms, of course, when water freezes. Only one type of ice is formed at atmospheric pressure and temperature, the so–called ordinary ice I_h which has a hexagonal close packed structure. The atomic structure of ice depends on the geometry of the water molecule: each oxygen atom is bonded by its two hydrogen atoms to four other oxygen atoms. The oxygen atoms bonds firmly in layers of hexagonal symmetry but only forms one bond across to the next layer, see Figure 1.1. This defines a basal plane (the preferred slip plane), parallel to the layer structure. The number of molecular bonds to be broken for deformation, e.g., creep or fracturing, parallel to the basal planes are less than in other directions. The axis of symmetry, perpendicular to the basal plane, is called the c–axis; it coincides with the optical axis of each ice crystal. Depending on the stress rate and the orientation of the basal plane in combination with the stress direction , ice displays a combination of responses: it shows elastic response but also immediately begins to creep. In addition, ice exhibit creep (ductile) deformation mechanisms but is also an extremely brittle material if the applied stress or stress rate is sufficiently high. For instance, it can fracture in a brittle manner, even very near the melt temperature. Failure in ice is often caused by a combination of creep and fracture.

Ice crystals are generally of extremely high purity. This is because very few impurity atoms have the right size to occupy lattice sites in the atomic structure of an ice crystal. This is an important point to recognize when dealing with sea ice: although formed

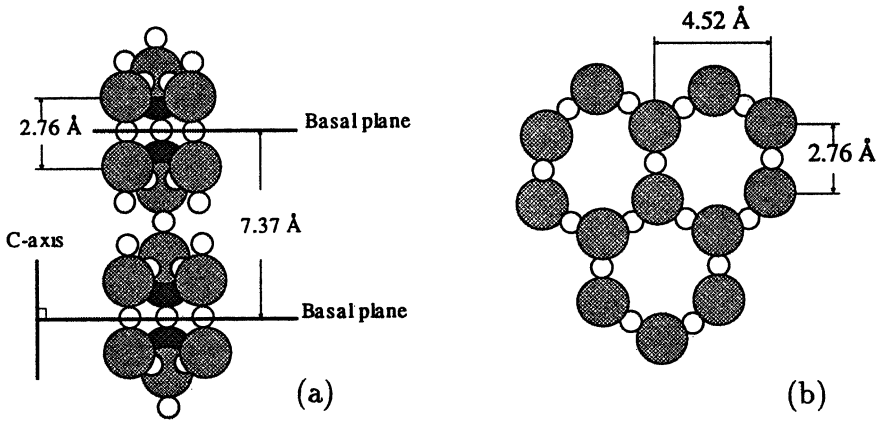

Figure 1.1: View of crystal lattice of ice. Large circles refer to oxygen atoms and small circles to hydrogen bondings; (a) View perpendicular to the c–axis, (b) View looking along the c–axis.

from a strong saline solution, the solid ice itself contains a negligible amount of salt. This implies that the mechanical behavior for low salinity sea ice and cold sea ice will be dominated by the freshwater ice characteristics.

The formation of ice is divided into two separate stages: To nucleate the first needle–like ice crystals a certain amount of supercooling and (foreign) nuclei are needed. As freezing progresses, ice bridges develop between neighboring crystals and a skim ice layer is formed. The second stage is the ice crystal growth induced by the heat exchange between the air–water–ice interfaces. During the freezing process the direction of heat flux is vertical, causing a downwards growth of wedge-shaped grains. These grains are composed of pure ice platelets, about 0.5 mm thick. When sea water freezes, these ice platelets are separated by layers of fine brine pockets. Part of the brine drains away from the growth boundary of the ice, but some is mechanically entrapped in the ice structure giving the sea ice a net salinity. Numerous brine pockets forms along the boundaries both between the ice platelets and between the grains. The pockets often form brine channels, which can extend vertically throughout the entire ice sheet. The channels serve as effective liquid brine drainage paths back into the sea water. In granular

ice, brine pockets only forms between the grain boundaries. This is probably because that randomly oriented grains produce less brine channels than columnar grains. The fluid brine exists in a complex stable equilibrium with the surrounding ice. At a given temperature the fluid within the pockets must have a typical salt concentration to be able to coexist with the pure ice. With a lowering of the temperature, part of the salt in the brine precipitates and is incorporated into the solid ice structure. Equations incorporating the effects of temperature, salinity and density on the air and brine volumes can be found in Cox and Weeks (1983).

A general presentation of ice properties is given in e.g. Weeks and Ackley (1982), Mellor (1983) and Sanderson (1988).

In Sweden ice properties have earlier been studied from an engineering point of view by e.g. Löfquist (1944, 1952), Bergdahl (1978), Cederwall (1981), Billfalk (1982) and Fransson (1984, 1988).

Paper **A**

Fracture toughness and crack growth of brackish ice using chevron notched specimens

Lars M. Stehn
Department of Civil Engineering
Luleå University of Technology
S-951 87 Luleå, Sweden

The following chapter is a version of a paper where the original text has been formatted and some minor errors have been corrected. The paper has been accepted for publication in:

Stehn L., 1993. Fracture toughness and crack growth of brackish ice using chevron notched specimens, *Journal of Glaciology*

Chapter 2

Fracture of brackish ice

2.1 Abstract

Field test equipment called *FIFT* (a Field Instrument for Fracture toughness Tests on ice) was used in both field and laboratory fracture toughness tests on brackish sea ice from the Gulf of Bothnia. An experimental calibration was performed and a compliance expression was then derived for the Short Rod Chevron Notched (*SRCN*) specimen. Using the *SRCN* configuration, for which the initial crack growth is shown to be stable, and measured load-point displacements, preliminary crack growth velocities are found. The obtained estimated crack velocity is, on average, $\dot{a}_e = 20\,\mathrm{ms}^{-1}$, albeit with a large standard deviation. The results indicate that critical crack (crack jumping) growth occurs. The apparent fracture toughness, K_Q, was found to have a pronounced dependency on porosity, in the form of brine volume. The results obtained are derived from a linearly elastic fracture mechanics (*LEFM*) theory. Consequently the tests were designed to satisfy small scale yielding requirements in terms of notch sensitivity and brittleness. The linearity of the load versus crack opening displacement curves together with a size effect study, showing that the specimen is notch sensitive for grain sizes ranging from 1.6 to nearly 100 mm, indicate that *LEFM* could be applicable.

2.2 Introduction

Ice/structure interaction results in loads. Structures in cold regions must be designed to withstand forces that ice can exert. A number of investigations have studied the mechanisms of ice failure. Ice can fail by a continuum mode of failure or by a fracture mode of failure. Fracture appears to be the dominant failure mode in nature and the presence and growth of cracks are of great importance to the final loading level, e.g., Fransson et al. (1991). Thus, the study of fracture mechanics is important in ice engineering problems in order to obtain the necessary knowledge regarding the physics of fracture in laboratory grown and naturally occurring ice. A survey of recent fracture toughness tests on sea ice is summarized in Stehn (1991); it is clearly evident that before fracture mechanics can be safely applied to ice engineering problems, further basic understanding of the mechanical behavior of sea ice is needed.

In the field, cracks are exposed to sublimation, free water and creep deformation in the vicinity of the crack-tip that makes them heal and blunt. Parsons (1990) demonstrates that a crack in ice can remain atomically (mathematically) sharp and that cracks do not extend slowly through creep. Dempsey et al. (1990) and DeFranco et al. (1991) found that there is a necessary minimum notch tip radius that must be attained if fracture toughness tests on fresh-water ice and saline ice are to be interpreted in terms of Linear Elastic Fracture Mechanics (*LEFM*). In the light of these findings it is clear that in fracture toughness testing it is essential to prepare a crack that is truly sharp[1]. A sharp crack is a necessary but not sufficient condition for the applicability of *LEFM* which also relies upon the energy dissipation process in the body being near local to the crack-tip in order not to affect the overall elastic response, the so called case of small-scale yielding. For metals, small-scale yielding is stated in ASTM E399 (1985) and requires a large crack length compared with the grain size. However, for cracks compa-

[1]The considerable scatter for the fracture toughness found in the literature is not unexpected since different loading rates, temperatures, grain sizes, crack orientations and loading geometries were used. In addition, the results are highly influenced by the methods, or lack of methods, to fabricate and sharpen the cracks.

rable to the grain size (as often can be the case for fracture testing on ice) the toughness obtained can only be regarded as a quasi-polycrystalline value which in no way fulfills the requirements for *LEFM*. Thus, the geometrical dimensions of the test specimen must be large enough to be notch sensitive. In this context the geometry is considered notch sensitive if the net failure stress stays constant with increasing crack length (at least within a certain crack length interval). Specimens having cracks outside this interval may experience a strength failure instead of an *LEFM* type fracture failure, and is referred to an notch ***insensitive***, Dempsey et al. (1992).

The specimen selected for this study is the Short Rod Chevron Notched (*SRCN*) specimen, see Figure 2.1. The apparent fracture toughness, K_Q,[2] for chevron notched specimens in general, herein the *SRCN* specimen, is determined from a quasi-statically growing macro crack. An initial crack of length a_o initiates from the chevron tip upon loading. For materials such as aluminum, Shannon and Munz (1984), and rock, Ouchterlony (1989a), the crack advances in a ***stable*** manner under increasing load due to the special geometry of the chevron notch. This initial quasi-stable crack growth will produce a sharp macro crack. Unstable crack growth occurs at the maximum load corresponding to a critical crack length, a_c, which is a function of the specimen geometry alone[3]. Thus, the *SRCN* specimen appears to be well suited for obtaining near K_{Ic} values for rate dependent materials since no crack-tip sharpening method should, in theory, be needed.

To date, the emphasis has been on determining the fracture toughness corresponding to the initiation of a stationary macro crack. For toughness tests without the consideration of crack growth stability, only single determination of K_{Ic} is possible. The stable crack growth characteristic of sea ice and freshwater ice is desirable for a number of reasons: it permits the crack-growth resistance, R,

[2]Due to the lack of a fracture toughness testing standard for ice, the notation K_Q should be used to denote an apparent fracture toughness, Dempsey (1989). This type of notation has long been used in the fracture toughness testing of rock, e.g., Ouchterlony (1982).

[3]Only for materials with flat crack-growth resistance curves, *R-curves*, does the maximum load correspond to the critical crack length a_c. For materials with rising R-curves, maximum load do not occur coincidently at a_c.

to be determined as a function of crack velocity, $\dot{a}$, and amount of crack growth, Δa; it permits the design of controlled experiments; it permits the toughening effect of the microstructure on the crack growth to be determined and it permits the evaluation of the critical energy release rate, G_{Ic}. Crack stability and growth on ice have only lately received any attention (Parsons et al., 1988 and 1989, DeFranco and Dempsey, 1990 and 1991). Controlled crack propagation may often be achieved simply by the choice of the appropriate specimen geometry. The *SRCN* specimen is known to promote quasi-stable crack growth which is also clear from enery balance calculations. From this discussion, the *SRCN* concept is felt to be especially suitable for fracture studies on ice. Three main conclusions can be made:

- The *LEFM* approach is valid provided that three essential conditions are met; (A) the crack-tip is sharp, (B) the crack length must be large in comparison with the grain size, and (C) the specimen size must be sufficiently large in comparison with the crack-tip energy dissipation zone for the stress and deformation fields surrounding the crack to be elastic.

- Further basic understanding of the fracture behavior of sea ice is needed. This knowledge is best gained from a combination of field measurements and laboratory studies.

- The *SRCN* geometry offers several advantages: the cylindrical form is obtained from ordinary core drilling and the shaping of the desired form can easily be carried out in–situ; it gives quasi-static crack growth in other brittle solids and has a favorable design for a minimum of released strain energy.

The present work includes: the development (with the above conclusions in mind) of a test system called *FIFT* (a Field Instrument for Fracture toughness Tests on ice) using the *SRCN* specimen geometry; the crack growth stability and velocity; a minimum specimen size criterion parallel to Dempsey (1989) in terms of notch sensitivity and brittleness; the influence of porosity on the apparent fracture toughness with respect to first year granular and columnar (often warm and rafted) brackish sea ice from the Gulf of Bothnia.

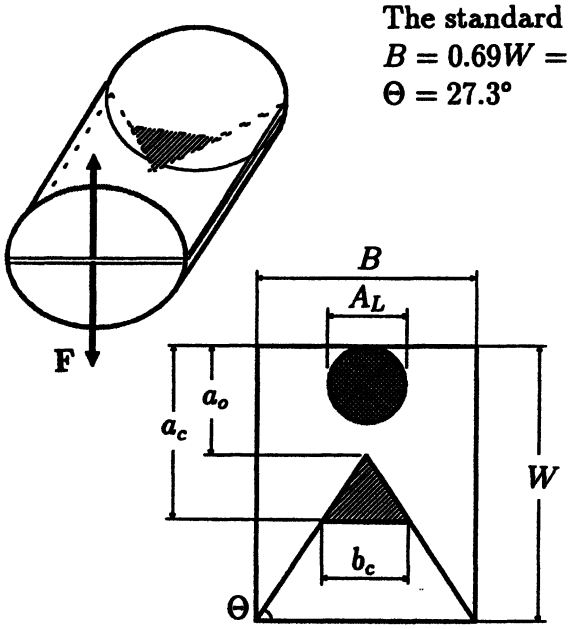

Figure 2.1: The Short Rod Chevron Notched, *SRCN*, specimen geometry with standard configuration according to ISRM (1988).

2.3 SRCN Specimen geometry and calibration

The *SRCN* with basic notation is shown in Figure 2.1. In this study the specimen configuration suggested by the International Society for Rock Mechanics, ISRM (1988), will be used. With the specimen diameter, B, as the measure of the specimen size, four independent parameters describe the uncracked geometry. The mode I energy release rate, G_I is given by

$$G_I = \frac{F^2}{2b}\frac{\partial C}{\partial a} \tag{2.1}$$

where C is the elastic compliance (δ_F/F) and δ_F the load-point displacement and b the trapezoidal crack front width which for a given dimensionless crack length, $\alpha = a/W$, (a is the crack length)

is given by $b = B[(\alpha - \alpha_o)/(1 - \alpha_o)]$. Accordingly, rearrangement of equation (2.1) in terms of the linear elastic stress intensity factor, $K_I^2 = GE'$, to obtain the shape function gives

$$Y_{SR} = \left[\frac{1}{2}\frac{\partial \hat{C}}{\partial \alpha}\frac{1-\alpha_o}{\alpha - \alpha_o}\right]^{1/2} = \frac{K_I B\sqrt{W}}{F} \tag{2.2}$$

Here, $\hat{C}$ is the dimensionless compliance, $\hat{C} = CE'B$, where E' is the effective elastic modules $= E$ for plane stress, $= E/(1-\nu^2)$ for plane strain. For a sufficiently brittle material the stress intensity factor attains its critical value when the load reaches a maximum: F_{max} at $Y_{SR} = Y_{min}(W/B, \alpha_c, \alpha_o)$ where α_c is the dimensionless critical crack length.

$$K_Q = \frac{F_{max}}{B\sqrt{W}} Y_{min}(W/B, \alpha_c, \alpha_o) \tag{2.3}$$

To the author's knowledge, no analytical solution for the shape function is available. Various calibrations are therefore necessary for the derivation of Y_{min}. The most complete calibrations are found in Bubsey et al. (1982) and Shannon et al. (1982) and in Matsuki et al. (1991). For the application to *FIFT*, where a pressure is applied over a circular load area, the *SRCN* specimen was calibrated for a load area loading, see Stehn (1990). Three specimens were taken from a 200 mm diameter polypropylene cylinder. The sizes of the diameter B and the length W were varied to provide load area to diameter ratios of $A_L/B = 0.27$, 0.54 and 0.81. The crack length was increased in steps so that $\Delta\alpha \approx 0.05$ for $\alpha_o \leq \alpha \leq 0.95$. To reduce errors, slope (compliance) measurements were taken as averages over two load cycles. A value was obtained during loading and unloading in each cycle.

It became clear that both Y_{min} and α_c are rather insensitive to variations in A_L/B. The maximum deviation in Y_{min}, compared to the *ISRM* standard, was found to be about 1.5%, which is negligible compared with the uncertainties in the measured values. A change in the type of loading appears to alter the shape function in the manner described by Ingraeffa (1984) and Matsuki et al. (1991).

The curve that best fitted the compliance data plotted in Figure

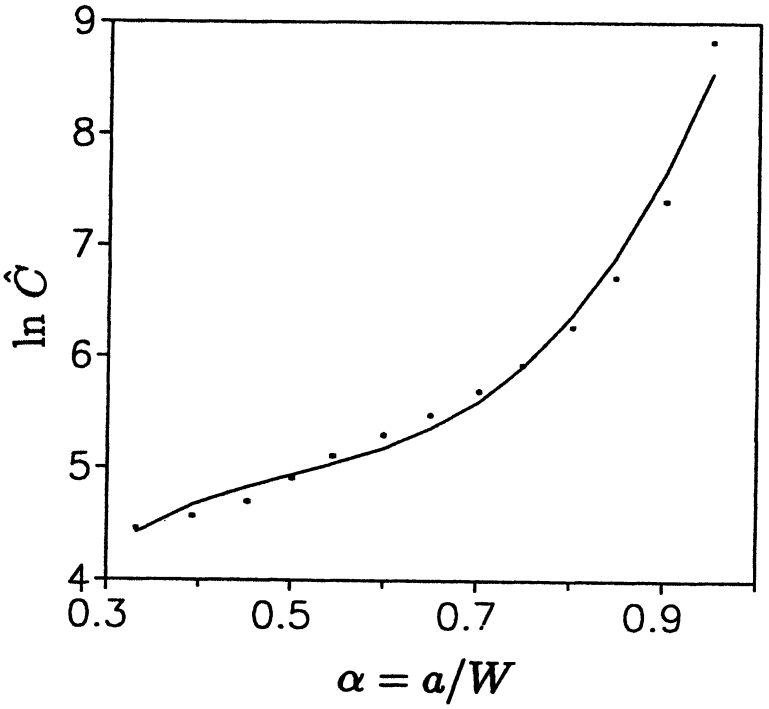

Figure 2.2: Experimental load-point compliance for $A_L/B = 0.27$ plotted in a $ln\hat{C}$ versus α curve.

2.2 was to be:

$$\hat{C}_{SR} = e^{(25.08\alpha - 45.37\alpha^2 + 29.94\alpha^3)} \tag{2.4}$$

Thus, Y_{SR} using *FIFT* may be calculated according to equation (2.2) as

$$Y_{SR} = [\hat{C}_{SR}(12.54 - 45.37\alpha + 44.91\alpha^2)(1 - \alpha_o)/(\alpha - \alpha_o)]^{1/2} \tag{2.5}$$

The critical crack length α_c is found by interpolating and extrapolating the values from Shannon et al. (1982), see Stehn (1990). Using the technique in Ouchterlony (1985), this results in:

$$\alpha_c = 0.570(1 - 0.068\frac{\Delta W}{B} + 0.636\frac{\Delta a_o}{B}) \tag{2.6}$$

where, for the variations in W and a_o, we have:

$$\frac{\Delta W}{B} = \frac{W}{B} - 1.45 \ , \ \frac{\Delta a_o}{B} = 0.481 - \frac{a_o}{B} \tag{2.7}$$

The initial dimensionless compliance, $\hat{C}_o$ when $\alpha = \alpha_o$, is given by Ouchterlony (1989b)

$$\hat{C}_o = 84.5(1 + 2.901\frac{\Delta a_o}{B} + 2.527(\frac{t}{B} - 0.012)) \tag{2.8}$$

where t is the chevron notch thickness. The elastic modules when bending the specimen material is thus given by:

$$E' = \frac{\hat{C}_o}{C_o B} \tag{2.9}$$

where C_o is the initial tangent slope in a $(F - \delta_F)$ plot.

2.4 FIFT– A field instrument for fracture toughness tests on ice

A complete facility for fracture toughness testing on ice should contain two separate parts: A laboratory test facility and field test equipment. An in–situ test can never give more accurate results

than the laboratory counterpart. However, ice engineering problems require *real* ice properties measured in the field. In line with that developed by Fransson et al. (1989a) and (1989b), a field instrument for fracture toughness tests on ice has been developed, Stehn and Fransson (1989) and Stehn (1990). The key design requirements for *FIFT* were:

- The test procedure must be simple enough for two men to handle in the field. No complex load frame or power supply were to be required.
- A high system stiffness. Naturally, it must be stiffer than the elastic modulus of ice, $E \approx 5 - 9$ GPa, but also stiff enough to present a loading condition favourable to stable crack growth.

The design of *FIFT* is shown in Figure 2.3. *FIFT* has two basic components: a field instrument and a data acquisition system. The length of the field instrument is 430 mm. Together with the portable data acquisition system the total weight is about 15 kg. Field conditions are wet and cold, so all temperature sensitive equipment (amplifier, data acquisition unit and the batterys) is placed inside an insulated box that is heated with a simple chemical heating system.

In principle, the instrument consists of a house attached to a hydraulic load cushion. The house is a threaded, hollow pipe filled with fluid. A simple hand-held electrical drilling machine is used to rotate a screw that via a piston depresses the fluid from the house into the load cushion. The load cushion is fitted into a slot of the *SRCN* specimen. This is schematically shown by the shaded, circular, area in Figure 2.1. When the fluid (antifreezing mixture of water and glycol) is compressed into the cushion, one side stays motionless while the other expands, linearly, and applies force on the specimen. The drilling machine develops a torque of 11 Nm and rotates at 1100 revolutions per minute. This is powerful enough for the loading rate to be fairly constant at around 200Ns^{-1}. The load is measured directly via a small 1000 N load cell (Kyowa LM-100KA).

Several tests have been performed in cold rooms to check the reliability of the instrument. The cushion is designed to sustain very

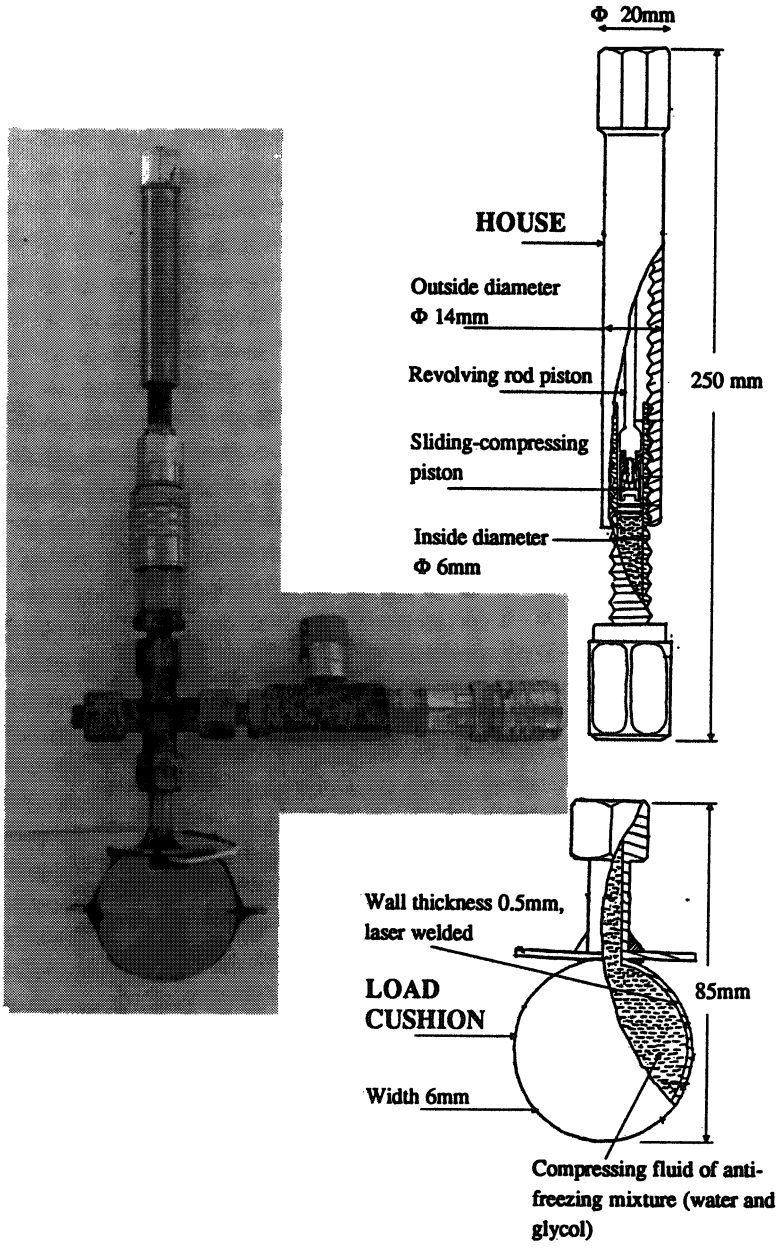

Figure 2.3: Layout of *FIFT*: General outline, detail of loading arrangement and detail of cushion.

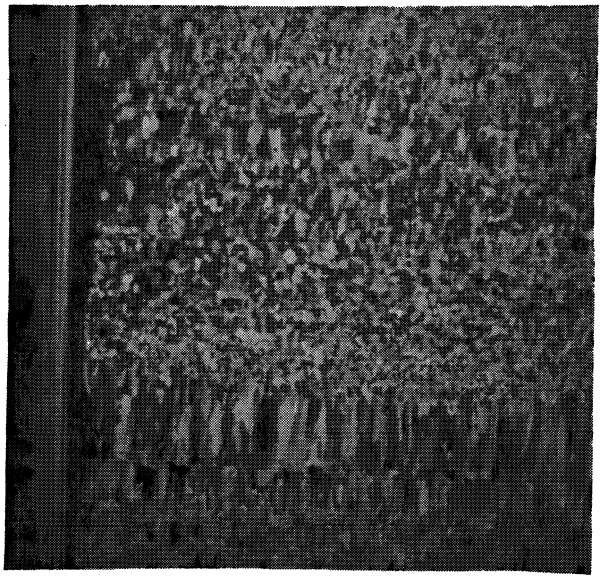

Figure 2.4: Vertical thin section photographed between crossed polaroids.

high pressures and to verify this it was subjected to a pressure of 800 kPa. The cushion did not leak or burst. The reaction at different temperatures was examined, with emphasis on the function of the load–cell and load housing. No drastic changes were found.

2.5 Experimental procedure and test results

These fracture tests were conducted on ice from the Gulf of Bothnia on three separate occasions, February to March of 1988, April of 1990 and January to April of 1991. The ice from 1988 was used in preliminary *FIFT* tests. The grain structure of the ice was determined from thin vertical and horizontal sections. The structure was found to be predominantly granular, with layers of columnar ice 15-20 cm apart, see Figure 2.4. This indicates that the ice was rafted. Some samples were collected and tested at lighthouses further out in the Gulf and they had a columnar structure. Two samples, no. 5.3 and 5.4, see Table 2.1, had grown under calm conditions and consisted of very large columnar grains.

The specimens were made from cores with a diameter of 193 mm. The *SRCN* specimen slot with its chevron notch was machined with a band saw and a milling machine. In the field, the specimens were manufactured with a hand held saw and milling machine. In all cases except test no. 4.8, 5.3 and 5.4 the crack front was perpendicular to the direction of the crystal growth. For the tests mentioned the crack front was parallel to the columnar grains, i.e., the same as radial cracking. Average grain size was estimated using the mean linear intercept method and ranged from 1.6 to nearly 100 mm. The ice was rather porous as demonstrated by the average densities of 875±7 kgm^{-3} at -1°C for series 1, 883±22 kgm^{-3} at -5°C for series 2, 883±5 kgm^{-3} at -3°C for series 3 and 894±9 kgm^{-3} at -10°C for series 4-6. The temperatures during the tests varied between -10°C and -1.5°C. Loading rates were difficult to estimate, but the time to fracture ranged from 0.7 to 3.8 seconds.

After testing, the dimensions of the specimens were measured and each specimen was carefully examined. The temperature was measured immediately after the test in a small hole drilled into the specimen approximately at a_c. With the exception of no. 1.2 and 3.6 the specimens cracked along the chevron notch. In the above mentioned tests, a transverse failure occurred before a proper evaluation of the fracture toughness could be made. This appears as a broken *arm* where the crack had veered of from the chevron plane and out into the arm. Ouchterlony (1985) has described this phenomenon with regard to rock specimens.

The fracture surfaces were visually examined. The critical crack length was clearly visible in most cases. Furthermore, very interesting features of the fracture of sea ice could be seen, just by the naked eye. In the upper triangular part of the notch the surface had a wavy appearance showing evidences of conchoidal brittle fracture. The lower part of the chevron notch evidenced a smoother surface with horizontal lines extending over the whole width of the notch. The lines came closer together towards the bottom of the specimen. This suggests that the crack was propagating through the mechanism of continuous cleavage fracture, in other words through the mechanism of irregular brittle crack growth (crack jumping). This behavior has been observed on freshwater ice and cold saline ice

(see introduction). It is recognized that these observations are only based on what could be detected visually.

The δ_F was measured, in some tests in series 1 and 2, with two Linear Variable Displacement Transducers (*LVDTs*). In series 6, δ_F was measured using two clip gauges. The load and load-point displacement for series 1 through 3 were measured using a 20 MHz storage oscilloscope, while for series 4,5 and 6 the signals were processed by a 16 bit analog-to-digital converter, set in a DARTEC testing machine in series with a 386SX microcomputer. Data was received at the rate of 300 readings per second. The load and δ_F versus time and the load versus δ_F results for test no. 6.2 are shown in Figure 2.5. The crack growth commences at the distinct change of slope, for both F and δ_F , as shown in Figure 2.5(a). This is a typical feature of all $(F-\delta_F)$ records, where in some cases evidence of non-linear processes appeared as a non-linear slope after the crack initiation. Figure 2.5(b) also shows crack initiation in more detail.

The experimental results from the 42 fracture tests are summarized in Table 2.1 and Table 2.2. Each test is identified by a group and a sequence number followed by an a_c/d_{av} ratio, i.e., critical crack length/average grain size. S is the salinity deduced from measured melt water conductivity at 20°C, T is the test temperature, F_{max} is identified as the maximum load from load versus time records, t_f is the time to failure. In Table 2.2 E is the effective elastic modulus in bending based on the initial compliance. G_{Ic}, the energy release rate, is calculated according to equation (2.1) and $G_Q = K_Q^2/E$ is the apparent critical energy release rate. It is important to note that the grain size, temperature and loading rate were not kept constant between the tests and this causes a significant scatter in the results. However, similarities between G_{Ic} and G_Q (Table 2.2) indicate that this low saline granular ice is quite isotropic and homogeneous and the selected specimen size was probably large enough, compared to the relatively small average grain size, not to contribute to the scatter.

Figure 2.6 shows the apparent fracture toughness versus the temperature. Figure 2.7 shows the apparent fracture toughness versus the average grain size. In the Figure we see that K_Q is rising

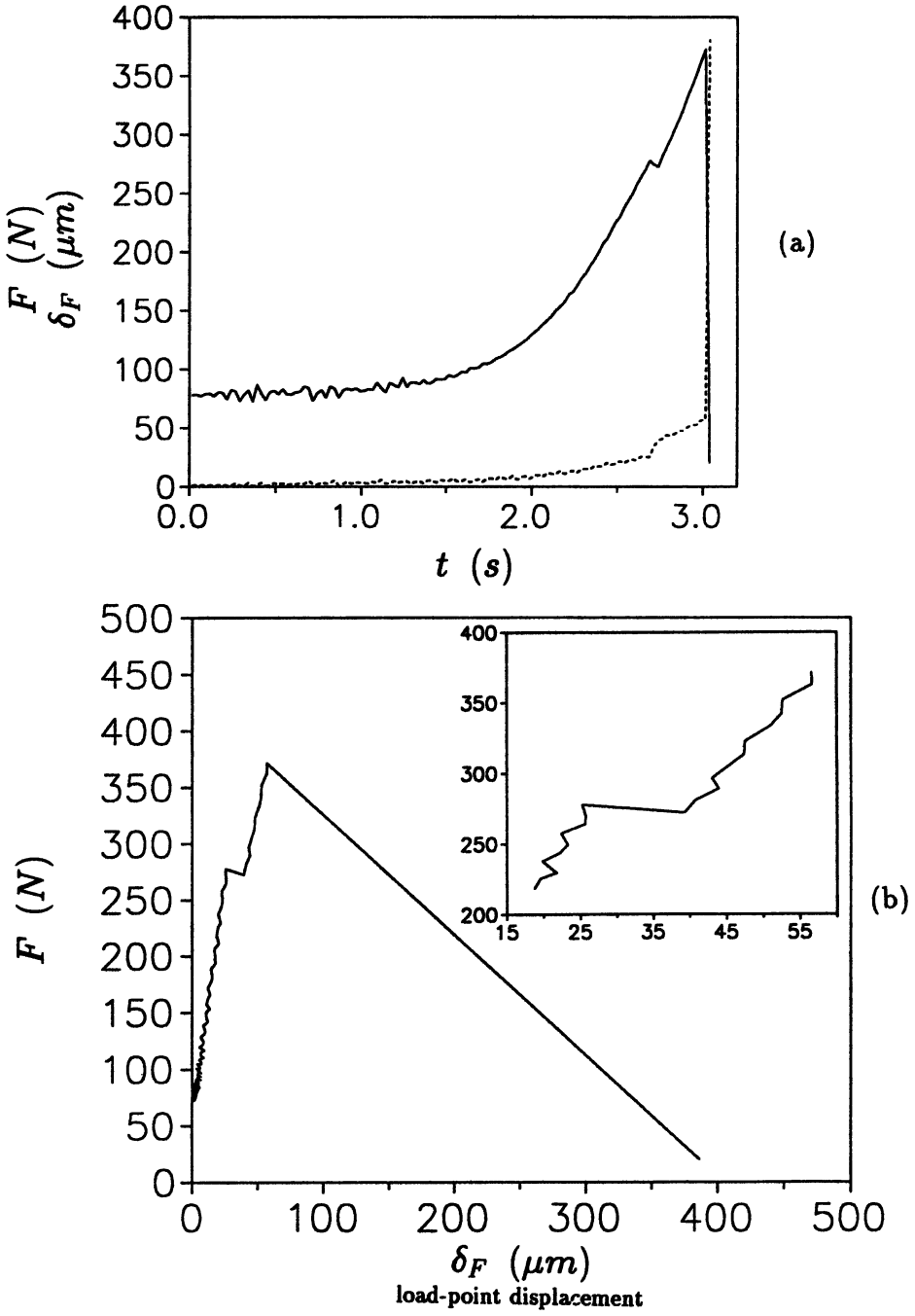

Figure 2.5: (a) F and δ_F versus time, and (b) $(F - \delta_F)$ record for test no. 6.2.

no.	a_c/d_{av} (mm/mm)	S (ppt)	T (-°C)	F_{max} (N)	t_f (s)	K_Q (kPa$\sqrt{\text{m}}$)
1.1	199/2.7^g=74	0.12	5.0	287.0	2.0	98
1.2	163/1.7^g=96	0.14	5.0	208.0	2.3	64
1.3	198/3.7^g=54	0.08	5.0	329.8	1.9	112
1.4	194/2.9^g=67	0.07	5.0	299.7	2.0	103
1.5	192/3.0^g=64	0.09	5.0	325.4	2.0	108
1.6	186/-	0.08	7.5	339.4	1.7	97
1.7	175/-	0.23	7.5	309.0	1.6	88
1.8	198/-	0.33	7.5	241.3	2.3	70
2.1	175/4.6^g=38	0.22	10.0	294.4	1.4	87
2.2	169/3.3^g=41	0.22	10.0	273.2	2.8	95
2.3	177/3.9^g=45	0.31	10.0	266.3	1.5	73
2.4	171/4.4^g=39	0.24	10.0	246.6	1.4	85
3.1	178/1.9^g=94	0.11	5.1	254.2	1.2	73
3.2	183/1.9^g=96	0.30	4.1	178.9	1.3	54
3.3	185/3.3^g=56	0.05	3.8	357.2	2.2	107
3.4	203/2.0^g=102	0.17	4.1	257.6	1.7	80
3.5	178/3.4^g=52	0.31	3.8	192.7	1.5	55
3.6	197/1.4^g=141	0.12	4.2	60.6	2.3	21
3.7	179/2.8^g=64	0.15	4.3	284.2	1.2	82
3.8	176/1.8^g=98	0.22	3.5	167.2	1.5	48
3.9	181/3.3^g=55	0.13	3.2	328.6	1.8	94
3.10	179/1.9^g=94	0.31	3.8	172.0	1.3	53
3.11	180/1.6^g=112	0.41	4.2	118.0	1.2	33
3.12	181/2.0^g=90	0.38	2.1	152.9	1.2	46
4.1	167/3.3^g=51	0.02	2.0	408.8	1.5	137
4.2	155/4.3^g=36	0.01	2.9	588.2	1.6	143
4.3	173/19.8^c=9	0.06	5.3	350.6	1.8	112
4.4	168/22.2^c=8	0.09	3.4	481.8	2.0	153
4.5	167/30.0^c=6	0.02	3.4	503.8	2.1	168
4.6	159/17.5^c=9	0.02	2.9	349.9	1.8	103
4.7	160/10.8^c=15	0.12	4.7	301.1	1.4	84
4.8	167/6.4^g=26	0.08	1.2	375.2	1.2	112
5.1	157/52.9^c=3	0.05	8.9	482.5	1.2	127
5.2	163/4.7^g=35	0.11	9.0	369.7	1.0	111
5.3	158/90^{mc}=2	0.20	9.0	304.9	1.3	83
5.4	154/100^{mc}=2	0.04	9.0	276.8	0.7	72
6.1	158/2.7^g=59	0.04	10.0	475.6	1.4	136
6.2	155/2.7^g=57	0.04	10.0	316.5	1.4	83
6.3	155/3.1^g=50	0.10	10.0	356.3	3.0	99
6.4	153/2.8^g=55	0.04	10.0	313.5	3.8	73
6.5	152/2.1^g=72	0.02	10.0	516.4	1.0	124
6.6	152/3.4^g=45	0.04	10.0	377.8	1.5	88

Table 2.1: Test data and results for sea ice SRCN specimens. Notes: (g) granular; (c)columnar; (mc) monocrystal.

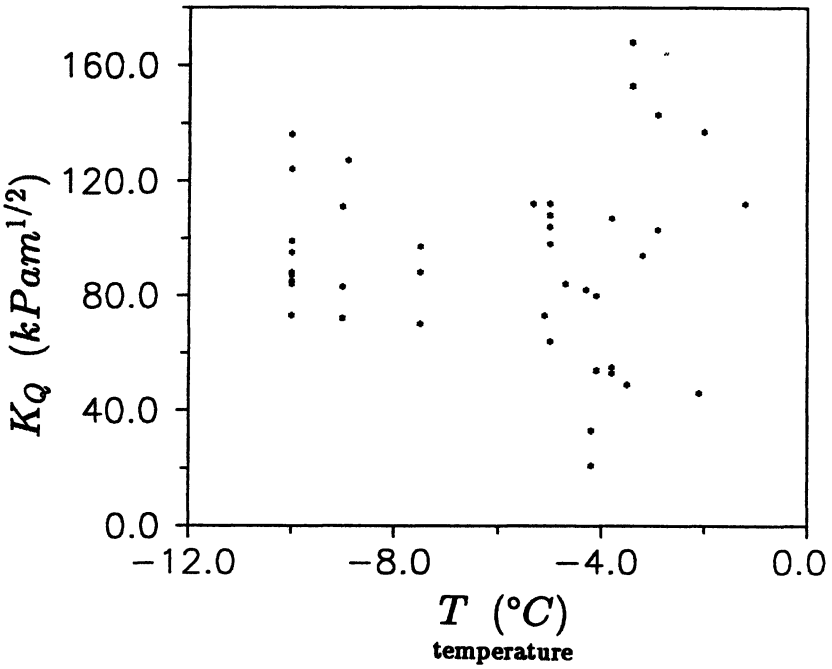

Figure 2.6: Apparent fracture toughness versus temperature.

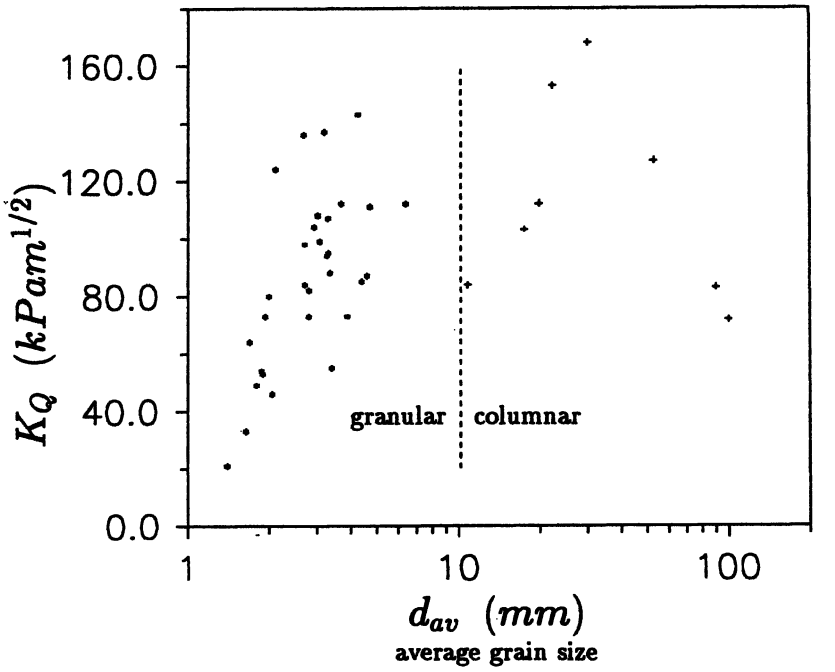

Figure 2.7: Apparent fracture toughness versus average grain size.

no.	E (GPa)	G_{Ic}/G_Q (Jm^{-2})
1.1	5.9	1.2/1.6
1.2	3.8	0.6/1.1
1.3	7.6	1.2/1.6
1.4	5.3	1.4/2.0
2.1	6.4	0.6/1.2
2.2	6.1	0.8/1.5
2.3	5.4	0.6/1.0
2.4	8.7	0.5/0.8
6.1	3.1	4.1/6.0
6.2	4.2	1.4/1.6
6.3	7.6	1.0/1.3
6.4	3.3	2.0/1.6
6.5	7.3	2.4/2.1
6.6	4.0	2.5/1.9

Table 2.2: Test results for sea ice SRCN specimens.

to a maximum and then subsequently decreasing as d_{av} increases. Dempsey and Wei (1989) discussed this type of grain size dependence for ice and Rice et al. (1978) for non-cubic ceramics. The break point is indicated to depend on a crystal structure–thermal expansion and strain mismatch effect.

2.6 Stable crack growth

Various parameters affect crack growth: method of loading (displacement or stroke control), loading rate, specimen geometry (reflected through its G) and the material. Stable crack growth, in the situation of continuous quasi-static growth, has not been obtained in ice. Instead, crack jumping is observed where the crack grows abruptly over a distance and then arrests, (DeFranco and Dempsey, 1990 and 1991, and Parsons et al., 1988 and 1989) on both fresh and sea ice. This behavior may be attributed to a decreasing crack growth resistance of the ice.

In stable crack propagation crack velocity is low and the extension may be tracked visually. Unstable crack propagation is asso-

ciated with an abrupt load drop at fracture, and that a crack that accelerates quickly generates considerable kinetic energy. Crack growth stability requires that the crack driving force and the crack-growth resistance are equal. On the other hand, in dynamic conditions, crack growth stability occurs when the rate of change in the crack driving force is equal to the sum of the rate of change in the resistance to fracture and the kinetic energy. This type of simplified dynamic energy rate balance presupposes the following: the displacements and crack area are the same as for static conditions and the elastic crack speed is low so that the crack propagates under continuous quasi-static conditions. The requirements for stable crack growth may thus be formulated as:

$$G = R + \frac{\partial H}{\partial A} \quad \text{and} \quad \frac{\partial G}{\partial A} = \frac{\partial R}{\partial \Delta A} + \frac{\partial^2 H}{\partial A^2} \tag{2.10}$$

where A denotes the crack area and H the specimen's kinetic energy. For quasi-static cracking the rate of change in the specimen's kinetic energy $(\partial H/\partial A)$=0.

Stable crack propagation may be quantified using the concept of geometric stability factor (*gsf*), Mai and Atkins (1980). If the test geometry has an adequately negative *gsf*, it should be capable of coping with the observed $\partial R/\partial \Delta a$ negative characteristics of ice. By the use of equation (2.1), differentiated with respect to A, and equation (2.10), the normalized *gsf* for a displacement controlled test on the *SRCN* geometry is:

$$\frac{W^2}{G}\frac{\partial G}{\partial A} \geq f(W/B, \alpha, \alpha_o)\left(\frac{d^2\hat{C}/d\alpha^2}{d\hat{C}/d\alpha} - 2\frac{d\hat{C}/d\alpha}{\hat{C}}\right) - g(W/B, \alpha, \alpha_o) \tag{2.11}$$

where

$$f = \left(\frac{W}{B}\right)\frac{1-\alpha_o}{2\alpha - \alpha_o}$$

$$g = \left(\frac{W}{B}\right)\frac{(1-\alpha_o)^3(2\alpha-\alpha_o)(3\alpha-\alpha_o)}{\alpha(\alpha-\alpha_o)[(\alpha-\alpha_o)(1-\alpha_o)+\alpha(\alpha-\alpha_o)^2]^2} \tag{2.12}$$

The third term on the right hand side of equation (2.11) arises from the effect of the increasing crack front length with crack growth.

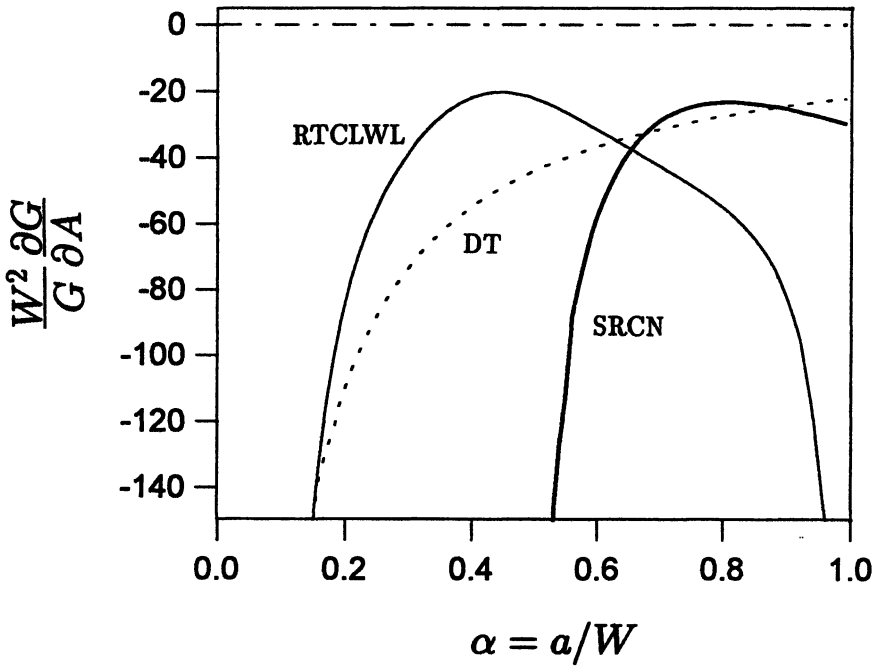

Figure 2.8: Normalized gsf's versus α.

The above concept has been used both for the Double Torsion (*DT*) specimen, Parson et al. (1989), and for the Reverse Tapered Crack Line Wedge Loaded (*RTCLWL*) geometry developed by DeFranco and Dempsey (1991)[4]. Figure 2.8 shows a plot of the normalized *gsf's* for the *DT*, *RTCLWL* and *SRCN*, cf. DeFranco and Dempsey (1991). It is instructive to note that the geometry of every specimen shows negative *gsf's* for all crack lengths. The *RTCLW* and the *SRCN* both promote stable, even for a strong rate sensitivity of crack propagation, crack growth.

Assuming that the underlying independent test variable is time,

[4]It may be of passing interest to recognize that a smaller thickness has a positive effect on crack growth stability as can be found by differentiating the requirements for stable crack growth with respect to A instead of a (that is only applicable for specimens with constant crack widths). The original *gsf* equations for the *DT* and *RTCLWL* specimens, presented in Figure 2.8, was multiplied with the ratio (W/b). With this alternative formulation it is readily discerned that a thin specimen promotes crack growth stability

then in a displacement controlled test $\delta_F = \dot{\delta}_F \cdot t$ and $F = F(\delta_F)$. If the compliance is differentiated under the conditions of steady-state crack growth and the assumption that crack length a increases monotonically with δ_F, the result is:

$$\dot{C} = \frac{\dot{\delta}_F}{F}(1 - \frac{\partial F}{\partial \delta_F}C) = \frac{\dot{a}_e}{WBE}\frac{\partial \hat{C}}{\partial \alpha} \tag{2.13}$$

Hence by using $F = F_{max}$ according to equation (2.3), the estimated crack velocity for the *SRCN* specimen can be written as:

$$\dot{a}_e = \frac{Y_{min}}{\partial \hat{C}/\partial \alpha}\frac{E\sqrt{W}}{K_Q}(1 - \frac{\partial F}{\partial \delta_F}C)\dot{\delta}_F \tag{2.14}$$

It is important to note that the $(F - \delta_F)$ plot is of paramount importance since E, $\partial F/\partial \delta_F$ and $\dot{\delta}_F$ directly relies upon it. $\partial F/\partial \delta_F$ is taken as the slope immediately prior to the maximum load. This simplification is reasonable since the critical toughness value is representative in a relatively wide region around the load maximum. Another simplification is to assume a *smooth load maximum* implying that $\partial F/\partial \delta_F = 0$ at $F = F_{max}$. This yields an estimated crack velocity as:

$$\dot{a}_e = \frac{Y_{min}}{\partial \hat{C}/\partial \alpha}\frac{E\sqrt{W}}{K_Q}\dot{\delta}_F \tag{2.15}$$

A smooth load maximum did not occur in any of the tests, as is evident from the typical test displayed in Figure 2.5. By making this kind of simplification the crack speed is overestimated by 22% on average.

A way of quantitatively determining the stability and dynamics of the calculated crack velocities, in terms of imparted kinetic energy, is given by Gurney and Ngan (1971). They set up a criterion for stability where only 5% of the stored strain energy is transformed into the kinetic energy of the specimen. By using equation (2.10) and the simple one–dimensional *SRCN* beam theory model in Stehn (1992) recalculated according to equation (2.10), a crack velocity when kinetic energy is not negligible is calculated as:

$$\dot{a}_H \approx 0.64c \tag{2.16}$$

#	$\dot{\delta}_F$ (mms^{-1})	$\dot{a}_e$ (ms^{-1})	Δ (%)
1.1	10	9	0.5
1.2	14	30	2.2
1.3	15	12	0.6
1.4	12	9	0.6
2.1	19	37	2.2
2.2	6	10	0.6
2.3	18	31	1.9
2.4	6	16	0.8
6.1	23	23	1.9
6.2	12	19	1.3
6.3	3	7	0.4
6.4	30	39	3.2
6.5	11	20	1.1
6.6	9	15	1.1

Table 2.3: Estimated crack velocities.

where $c = (E/\rho)^{1/2}$ is the speed of a longitudinal wave in the ice beam. An actual crack velocity can thus be compared with $\dot{a}_H$ to determine if the crack is growing in a stable manner by the 5% definition quoted above.

The load-point displacement rate, the crack velocity calculated from equation (2.14), and Δ, the percentage of the crack speed going into kinetic energy, i.e., $\dot{a}_e/\dot{a}_H$, are given in Table 2.3.

The values in the Table for crack velocity exhibits a large variability, something not uncommon for ice parameters. The average value for crack velocity is found to be $\dot{a}_e = 20\,\mathrm{ms}^{-1} \pm 11$. Parsons et al. (1987) also obtained a velocity of approximately 20 ms^{-1} measured on first year sea ice double cantilever beams. By the Gurney and Ngan definition it is clear that stable crack propagation is occurring. A multiple regression analysis performed on the data revealed that $\dot{\delta}_F$ had the greatest influence on crack velocity, which, in view of the theoretical work by Sigl (1991) on brittle solids, should be the case. The experimental values are presented in Figure 2.9 as K_Q versus estimated crack velocity. The scatter in

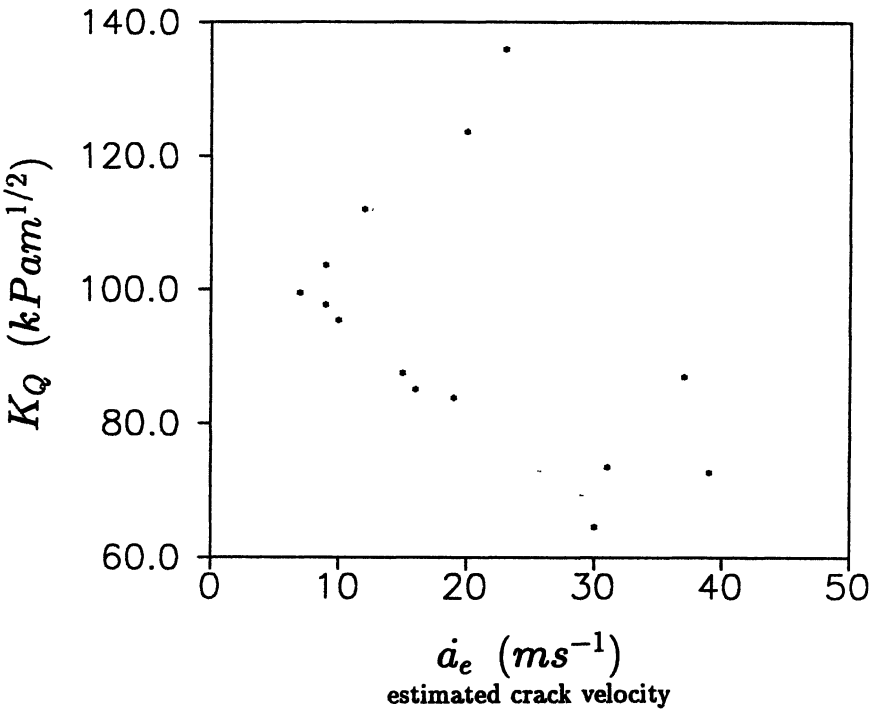

Figure 2.9: Apparent fracture toughness versus estimated crack velocity.

the Figure is substantial.

2.7 Porosity effects on fracture toughness

Pores in ice, as in other brittle materials, may affect the mechanical properties. Pores occur naturally during formation of the sea ice cover in the form of air and brine pockets. Air bubbles are comparatively large with a heterogeneous spatial distribution. To determine the actual distribution and size, back lighted sections, 5-8 mm thick , were studied using several specimens . The bubbles were of the same size as the granular grains, i.e., 0.5– 4mm, and 5-20 mm apart. However, sometimes the air bubbles were arrayed in vertical bubble pipes (typically in the granular-columnar boundary zone). This may have had a considerable weakening effect on the ice. The brine pockets showed a completely different distribution. The substructure of sea ice shows pure ice platelets, about 0.5 mm thick, separated by layers of brine pockets. The important influence of the substructure of saline ice is shown by DeFranco et al. (1991). For cold (-25°C) saline ice *SENB* tests using 4-pt bending, the observed fracture developed, in most of the cases, parallel to the long directions of the ice platelets.

The influence of porosity on cold, *columnar*, sea ice reported to date is mentioned in the works by Vaudery (1977), Timco and Frederking (1982) and Urabe et al. (1980) and is shown in Figure 2.10(b).

An assumption that may be made is that the crack will seek the path having the *minimum* solid area, i.e., the maximum area of porosity. In this case, fracture energy is proportional to the actual solid area fractured. This approach[5] results in the non-linear porosity dependent fracture toughness given by Rice (1977) in the following form, $K_{QP} = K_O e^{-m\Psi}$, where K_{QP} is the apparent porous fracture toughness, K_O is the toughness for zero porosity, Ψ, and

[5]Models by Kristic and Erickson (1987), Goldstein and Osipenko (1991) that assumes that the pores act as flaws, were tested but were discarded due to the physical assumptions they required.

m is an empirical exponent which depends on pore location, shape and size. Knudsen (1959) found that experiments on porous aluminum, steel and iron follow this type of relationship, and the same is indicated by Rice et al. (1978) for various ceramics.

A reasonable assumption is that for warm, spring, sea ice, pore shapes are (air) spheres and (brine) cylinders. Following the discussion in Brown et al. (1964), a composite m_c–value can be calculated where the contribution made by the two pore types is incorporated, see also Rice et al. (1978) and Stehn (1990). For each specimen, calculations of relative air and brine volume, V_b were carried out using the equations in Cox and Weeks (1982). Due to the distribution and hence influence of the different pores discussed above, it was assumed that the air pores only contribute to the total porosity but not as a fracture energy sink. The average of all 42 tests, gave $m_c = 0.28 \pm 0.13$. Thus, the theoretical model for the dependence of the brackish sea ice apparent fracture toughness on porosity, in form of brine volume, becomes:

$$K_{QP} = K_O e^{-0.28 \cdot V_b} \tag{2.17}$$

The resulting curve is plotted in Figure 2.10(a), where $K_O = 119\text{kPa}$ is determined from a regression analysis based on equation (2.17).

Evidently the experimental results are very well described by the theoretical relationship. The exponent m_c is related to the porosity characteristics. The numerical value found is interesting since Rice (1977) shows that m values in the range of 0.1 to 0.4 are connected with a homogeneous spatial distribution and shape of the pores and that pore location is important. This is consistent for brine in granular ice since the brine inclusions are in the form of fine pockets, evenly spread and concentrated around grain boundaries. This can be considerably more serious than pores located elsewhere. It should be noted that this model is only accurate for low brine volume values, i.e., for brackish sea ice, since for $V_b \approx 18\,\text{ppt}$ the model predicts zero strength.

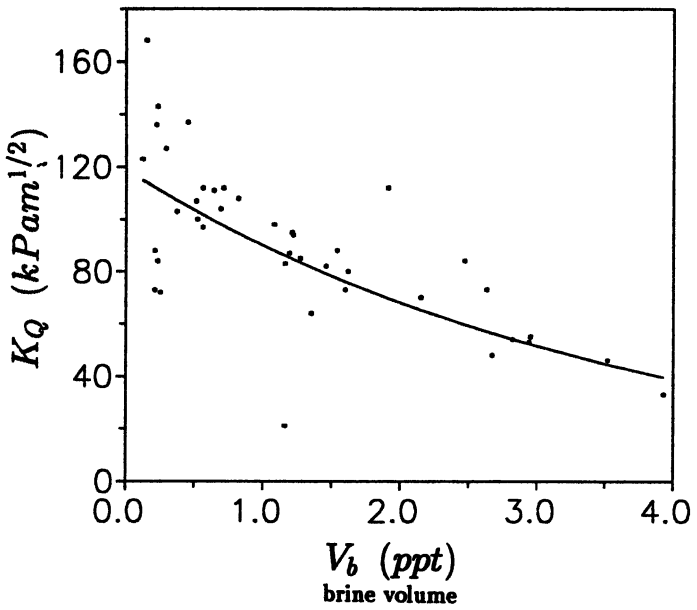

(a)

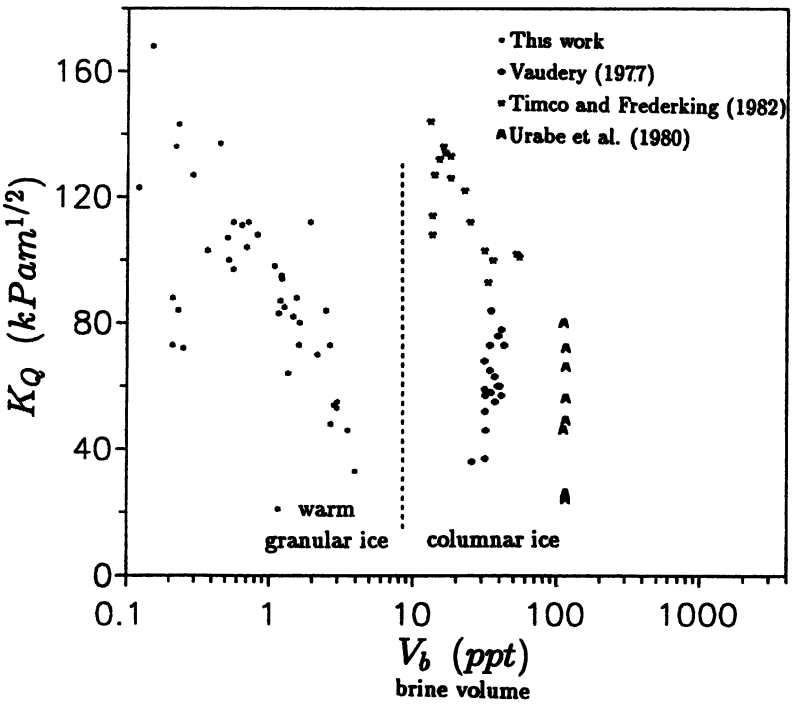

(b)

Figure 2.10: Apparent fracture toughness versus brine volume. (a) Experimental results. (b) Previous investigations.

2.8 Notch sensitivity

According to Dempsey (1989) many of the previous studies on both fresh and sea ice have used sub-sized specimens that are notch insensitive. If a specimen is to be referred to as notch sensitive the crack and uncracked ligament must be sufficiently long. The above study by Dempsey put forward analytical calculations regarding the dependence of the notch sensitivity and the brittleness on the specimen size. This approach provides a tool for a similar derivation for the *SRCN* specimen.

The peak nominal tensile stress, σ_N, acting on the net section at failure, is derived assuming a linear stress distribution throughout the uncracked ligament as:

$$\sigma_N = \frac{F_{max}}{WB} Z_{SR}(\alpha_o, \alpha_c) \tag{2.18}$$

Strictly $\alpha_c = \alpha_c(\alpha_o)$ but for α_c=0.570

$$Z_{SR} = 35.7 \frac{(\alpha_o^2 - 1.98\alpha_o + 0.83)}{(\alpha_o^2 - 1.62\alpha_o + 0.64)} \tag{2.19}$$

The ratio of σ_N to the tensile strength, σ_t becomes:

$$\frac{\sigma_N}{\sigma_t} = \frac{K_Q}{\sigma_t \sqrt{W}} \frac{Z_{SR}}{Y_{SR}} = \beta_f \cdot C_{NSR} \tag{2.20}$$

where $C_{NSR}(\alpha_o)$ is an *SRCN* geometry function. It is useful to note that β_f is related to the characteristic length, introduced by Hillerborg et al. (1976), as $\beta_f \equiv l_{ch}/W = E'G_{Ic}/W\sigma_t^2$. The characteristic length may be looked upon as a measure of the brittleness of a material since it relates the crack resistance energy to the elastic energy. Therefore, the parameter β_f could be called a *brittleness number*. Dempsey uses β_f to propose a requisite *LEFM* specimen width as σ_N/σ_t <0.4. But, and it is important to note this, he points out that no experimental work supports this and a thorough size effect study, involving different grain sizes, ice types, loading configurations, temperatures, etc., is required before this can be fully accepted.

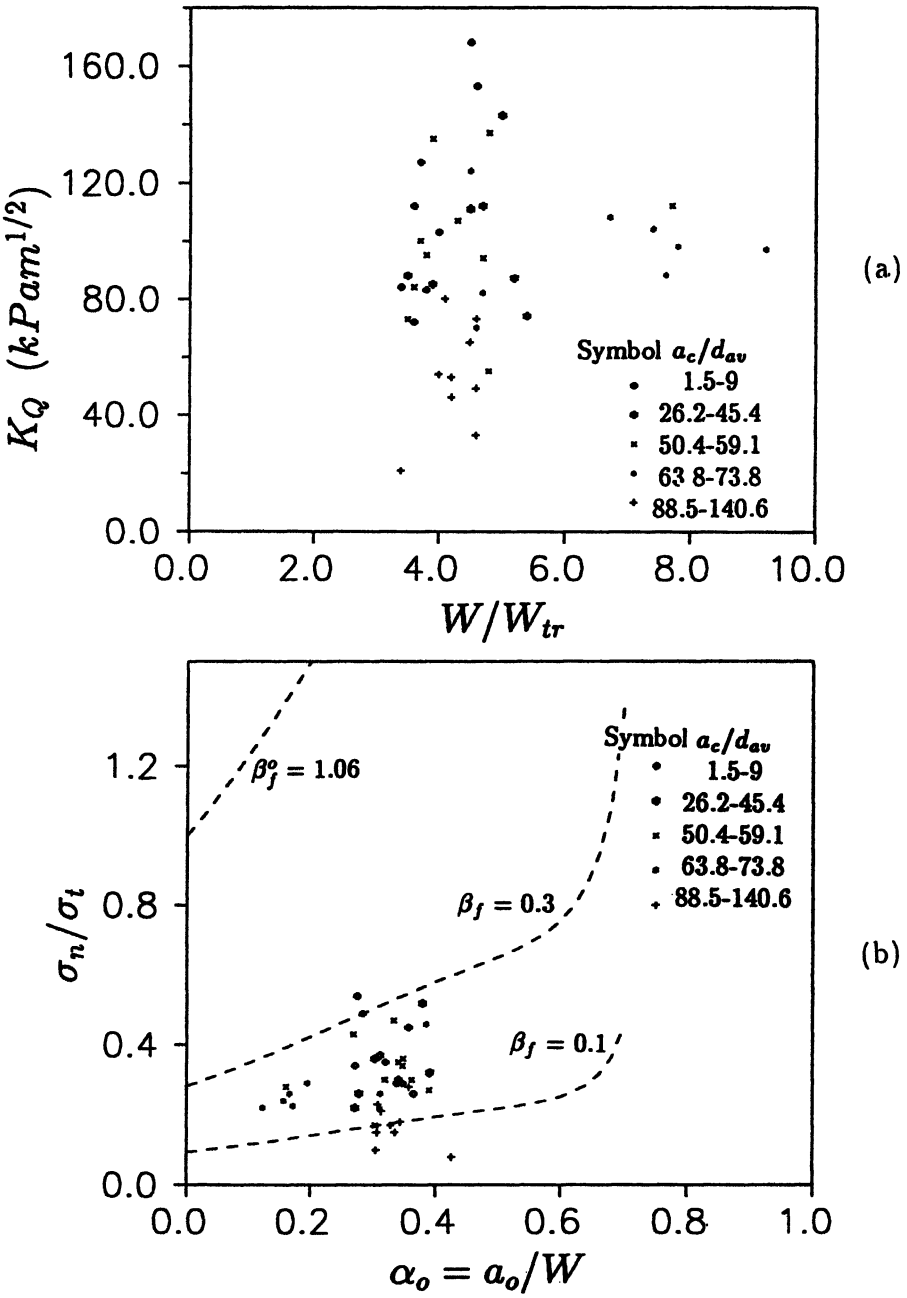

Figure 2.11: (a) Apparent fracture toughness versus specimen length to transitional length (W/W_{tr}), and (b) σ_N/σ_t versus initial crack length to specimen length (a_o/W). The dashed lines are lines of constant brittleness numbers, β_f, where a lower brittleness number means increased notch sensitive. For $\beta_f > \beta_f^o$ a strength failure will occur prior to the attainment of a critical stress intensity factor.

Following the procedure in Dempsey, K_Q is plotted versus the ratio of the actual specimen length to the transitional length[6] (W/W_{tr}) in Figure 2.11(a). The largest ratio occurs for $a_c/d_{av} \approx$ 26-74. This means that the appropriate initial crack length is $0.17 \leq a_o/W \leq 0.28$. Using the above expressions, the ratio of (σ_N/σ_t) is plotted versus the ratios of the initial crack length to the specimen length (a_o/W) in Figure 2.11(b). It is clear that the specimens were sufficiently large, i.e., notch sensitive enough, to keep the ratio σ_N/σ_t below 0.4. In terms of equation (2.20) it is equivalent to requiring that:

$$W^{\infty} \geq (2.5C_{NSR})^2 \left(\frac{K_Q}{\sigma_t}\right)^2 \tag{2.21}$$

where W^{∞} is the requisite *LEFM* size. Using the standard value of Y_{SR} and α_o=0.332 the geometry function C_{NSR}=1.633. The tensile strength for freshwater ice with d_{av} = 4mm = 0.9MPa, Currier and Schulson (1982). Assuming that K_Q = 100 kPam$^{1/2}$, the required specimen size for the *SRCN* specimen is given by:

$$W^{\infty} \geq 206 \text{ mm}$$

or taking Figure 2.11(a) into account, given that the average grain size within the largest W/W_{tr} ratios is 4.4 mm:

$$W^{\infty}/d_{av} \geq 47 \tag{2.22}$$

A clear picture depicted from Table 2.1 is that almost all, with the exception of the large columnar grained ice tested, specimens fulfill the size requirement stated in equation (2.22).

2.9 Discussion and conclusions

The test system operates very satisfactorily in the field. Field and laboratory test programs show that the system is reliable and the results obtained compare favorably with those presented in other

[6]The transitional length is the size for which if $W > W_{tr}$ a fracture failure will occur. However, the requisite *LEFM* size is bigger than W_{tr} due, mainly, to the facts (B) and (C) in the introduction.

studies. The simple test procedure, including the preparation of ice specimens and the necessary measurements (failure load and geometrical configuration), makes it possible to obtain representative toughness values directly. The field instrument is surprisingly stiff, as indicated by the fracture energy tests and recent tests on freshwater ice where irregular crack jumping was observed.

Included in the compliance calibration is also the compliance of *FIFT* as $C = C_{FIFT} + C_{SRCN}$. It is of utmost importance to minimize the contribution from the loading device. As stated above, only a 1.5% difference was detected using *FIFT* instead of the test setup used on *Al* specimens by Bubsey et al. (1982), and Shannon et al. (1982). Furthermore, in recent tests, a 40% increase in compliance was found when calibrating *FIFT* on a *PMMA RTCLWL* specimen compared with the compliance obtained using the stiff loading device of DeFranco and Dempsey (1991). This situation can be improved. Two instrument design details reduce the stiffness: the housing is not perfectly sealed and the most important fault is that the cushion expands, where it should be rigid, after the instability point has been reached. Another drawback with *FIFT* is the difficulty in controlling the loading rate.

The *SRCN* specimen does not generate high crack velocities when tested under displacement control. Due to the (sufficiently?) negative *gsf* the loading geometry promotes stable crack growth. Since the right hand side of equation (2.11) always is negative any instability must be due to the ice properties, i.e., a consequence of negative $dR/d\dot{a}$, and a lack of stiffness in *FIFT*.

The test results obtained on the estimated crack velocity show a large variability. It must be noted that, while the tested ice density, average grain size and brine volume did differ slightly, the test temperature for series 1 was -5°C while it was -10°C for series 2 and 6. Furthermore, the crack velocities presented are not measured but calculated using equation (2.14) so because of assumptions and approximations these results must be regarded with caution.

The fracture toughness crack velocity dependency, i.e., greater toughness at slower crack growth rate, found is very weak. In fact, Figure 2.9 shows virtually no trend at all. It is therefore likely that the *dependency* is a feature of the large variability of the sea ice

parameters involved. A consequence such a rate dependency of the toughness is that $dR/d\dot{a} < 0$.

Is the observed crack growth stable? Many different concepts are evoked by the use of the word stable. The equation (2.16) gives the upper limit for the crack velocity when kinetic energy is not negligible. Equally, in the sense of imparted kinetic energy, the growth rate is stable and not dynamic in brackish sea ice. A further question is whether, provided that the crack grows at critical conditions, the observed growth rate is subcritical (implying that it is creep growth), or is it just *stable* slow critical growth? Creep growth is accompanied by the emission of dislocations (blunting the crack) producing a largish creep zone ahead of the growing crack while no stable growth means no dislocation emission and a small creep zone. A theoretical model by Hui and Riedel (1981), for a slowly growing crack in an elastic- secondary creeping material, shows that it is required that n (the creep exponent) > 3 for creep growth to occur. The Hui and Riedel model works well providing cracking is a result of secondary creep, which is not at all certain for ice. Applying n= 3.2 and $B = 5 \cdot 10^{-25}\,(\mathrm{Pa}^{-3.2}\mathrm{s}^{-1})$ acquired from creep tests on ice from the Gulf of Bothnia and the Barents sea into the Hui and Riedel model, a creep zone size of the order of 10^{-13}m is obtained. The reader immediately notes that this is smaller than the interatomic distance of ice which makes this estimate very uncertain. So, this may seem inconsistent at first glance as *stable* growth is observed,and this should be accompanied by a largish creep zone[7]. However, together with the observations made on the fracture surfaces, which gave evidence of brittle failure, this implies that critical crack growth in *warm* brackish sea ice does not necessarily have to be creep growth but may be slow and stable.

The agreement between this work and previous investigations on porosity effects is not so good. It must be noted that different loading rates, test temperatures and loading geometries were used and that the previous specimens are *probably* sub-sized, yielding

[7]Recent creep tests, using *SENB* on freshwater single crystal ice, by Wei and Dempsey (1991) show a dislocation-free zone (*DFZ*) ahead of the crack tip. Adjacent to the *DFZ* and throughout the width of the specimen a plastic zone was detected. However, even though the specimens were stressed by a constant load for 5 hours, no crack growth was observed.

fracture toughness values that are too large. The work reported in this study shows a much more pronounced brine volume dependence than that of Vaudery (1977), Urabe et al. (1980) and Timco and Frederking (1982) on *columnar* ice. However, a significant aspect of the analysis is that the tests were performed on *warm granular* ice where the crack propagation direction was vertical downwards, i.e., parallel to the growth direction. These results can only therefore be applied to saline granular ice and not to saline columnar ice, since the ice types differ in their fundamental crystal texture. This would go a long way towards explaining the discrepancy in Figure 2.10(b). It might even be possible that another microstructural parameter that is related to brine volume affects the failure process in saline sea ice. This could be the subgrain size, which is defined as the distance between the brine pockets. Urabe and Yositake (1981) investigated this matter and the results in DeFranco et al. (1991) also point in this direction.

The results presented herein support the use of $\sigma_N/\sigma_t < 0.4$ as a specimen size criterion. They are very interesting since they are virtually the same as Dempsey et al. (1992), even though the tests were performed under different conditions.The loading geometries differed (*SRCN* versus *SENB*). The ice types and crack orientation differed (granular brackish sea ice versus freshwater S2 ice investigated for radial cracking). The temperatures differed (-1.2 to -10°C versus -10°C). The grain sizes (1.6 to 100 mm versus 3 mm) and the loading rates differed.

Paper **B**

Specimen geometry effects on the fracture of warm (S1) ice

Lars M. Stehn
Department of Civil and Mining Engineering
Luleå University of Technology
S-951 87 Luleå, Sweden
Samuel J. DeFranco
Amoco Production Co.
P.O. Box 3385
Tulsa, OK 74102–3385, USA
John P. Dempsey
Department of Civil and Environmental Engineering
Clarkson University
Potsdam, N. Y. 13699–5710, USA

This chapter is a version of a paper where the original text has been formatted. The paper has been submitted for publication in:

Stehn L.M., DeFranco S.J. and Dempsey J.P., 1993. Specimen geometry effects on the fracture of warm pond (S1) ice, *ASCE Journal of Engineering Mechanics*

Chapter 3

Geometry effects on the fracture of S1 ice

3.1 Abstract

Fracture toughness tests were performed on S1 type freshwater ice to investigate if similarities exist in the local K_I fields for three different fracture geometries. The ice was tested using a hand-held loading device called the *FIFT* (A Field Instrument for Fracture Toughness Tests on ice). The geometries tested were the Short Rod Chevron Notched (*SRCN*) specimen, the Reverse Tapered (*RT*) specimen and the Square Plate (*SP*) geometry. All tests were performed at -4°C. The results indicate that under comparable conditions (loading rate, temperature, crack orientation and propagation direction), the apparent fracture toughness K_Q is similar for all of the geometries. The toughness was computed assuming the initiation of a stationary macrocrack from linear elastic, isotropic K_I solutions. Scatter of the experimental results is accounted for in part by the large grain size of S1 ice. However, it is important to note that the results may be an artifact of sub–sized tests. Even though the ice was warm, the crack extended unstably in each experiment and the fracture surfaces of the split specimens showed evidence of brittle fracture. The test geometry, had a marked influence on the character of the fracture surface.

3.2 Introduction

Full-scale observations of ice-structure interactions suggest that splitting and fracture events are most prevalent (Blanchet et al., 1989). Global splitting or fracture has been proposed as a possible load limiting mechanism (Blanchet, 1990). Hovewer, the conditions under which fracture events occur have not been well defined. Scale effects also make it difficult to extrapolate laboratory experiments to the full-scale case. For this reason, a joint-industry-agency project "Large-Scale Ice Fracture Experiments" was initiated in 1991 (Kennedy et al., 1993) to provide quantitative measurements of large-scale ice fracture events. Phase 1 consisted of in-situ full thickness lake ice fracture tests in preparation for a more thorough set of experiments on sea ice in Phase 2. The Reverse Tapered (*RT*) and Square Plate (*SP*) geometries studied in this paper were the geometries tested in Phase 1 and 2, respectively.

Ice is ideal for performing in-situ fracture experiments due primarily to its availability and low fracture toughness relative to concrete or metals. This permits the use of portable loading systems capable of providing sufficient failure loads. An immediate consequence is the ability to experimentally verify full-scale fracture loads from laboratory size effect tests. In-line with this discussion, a test system called the *FIFT* (A Field Instrument for Fracture Toughness Tests on ice) has been developed (Stehn, 1990, 1993). The test system operates very satisfactorily in the field. The simple test procedure (hand-held load application and data acquisition systems) makes it possible to obtain representative toughness values directly. Motivation for this study was to jointly combine a small-scale investigation with a large-scale program in the field. By using a field instrument and the *RT* and *SP* specimens, the question of the minimum laboratory specimen size to determine fracture toughness of large-scale tests may then be addressed.

Materials such as concrete, rock, ceramics and ice have an aggregate or grain size that is several orders of magnitude larger than typical metals. Because of this inhomogeneity, these materials do not strictly meet the assumptions of continuum mechanics unless the volume sampled is large enough. That is, the minimum size

of a fracture toughness specimen must be large enough to ensure polycrystalline behavior. Because ice has such a large grain size, the effects of the specimen shape must also be investigated along with specimen size and notch sensitivity effects (Dempsey, 1991; Dempsey et al., 1992 and Parsons et al., 1993) Within the constraints of Linear Elastic Fracture Mechanics (*LEFM*), cracks in two bodies of the same material, but of different configurations, should initiate at a same value of the critical stress–intensity–factor (fracture toughness). This implies that the stress–intensity– factor may rationally be regarded as a *similitude* parameter for the in–plane crack tip stress fields. Therefore, this paper investigates whether similarities exist in the local K_I fields for laboratory scale ice specimens fabricated using three different fracture geometries; these geometries are described in the next section. The geometry effect on the apparent fracture toughness, K_Q, at initiation of a stationary macrocrack was examined on warm (- 4°C) S1 type freshwater ice. The active fracture mechanisms for each specimen type were studied from photographs of the fracture surfaces.

3.3 Loading device and specimen geometries

Field test equipment called the *FIFT* was used in the fracture toughness tests. The loading device consists of a hydraulic piston that is fitted into a groove in a specimen. The piston is expanded by compressing a column of fluid with a threaded piston which itself is driven by a hand-held electric drill. The expansion creates the opening load. The load is measured directly by a 1000 N load-cell mounted in the cylinder housing the piston.

The *FIFT* has previously been calibrated for the Short Rod Chevron Notched (*SRCN*) specimen and was in this work calibrated for the (*RT*) and (*SP*) geometries. In other words, the load–line crack opening displacement, δ_{LLD}, was determined in terms of the specimen compliance $C(a)$ ($\delta_{LLD} = FC(a)$) for a wide range of crack lengths a using polypropylene. This, in turn, gives the relevant expressions for the stress–intensity–factor, $K_I(a)$.

In this study *LEFM* relations were used to calculate the apparent fracture toughness. For each geometry, the ratio of specimen depth to average grain size W/d_{av} (refer to Table 3.1) was chosen as large as possible to satisfy criteria set forth in Dempsey (1991) so that notch *sensitivity* was ensured. In the context of notch sensitivity, an analysis using the *LEFM* approach is valid provided that: a fracture failure occurs, and that the length of the crack and the uncracked ligament are large in comparison with the grain size, and that the specimen size is many times the size of the crack tip energy dissipation zone (process zone).

The shape function for the *SRCN* can be found in Stehn (1993). The geometry was thoroughly investigated and the K_I–expression arises from a full *FIFT* calibration on polypropylene *SRCN* specimens. At fracture initiation, the apparent fracture toughness is

$$K_Q = \frac{F_i}{D\sqrt{W}} Y_{SR}(W/D, \alpha, \alpha_o) \tag{3.1}$$

where D is the diameter, W the specimen length, F_i the (macro)crack initiation load and α the relative crack length, $\alpha = a/W$. For $W/D = 1.45$, Y_{SR} is given as (Stehn, 1993):

$$Y_{SR} = [C_{SR}\frac{(1-\alpha_o)}{(\alpha-\alpha_o)}(12.54 - 45.37\alpha + 44.91\alpha^2)]^{1/2} \tag{3.2a}$$

$$C_{SR} = e^{(25.08\alpha - 45.37\alpha^2 + 29.94\alpha^3)} \tag{3.2b}$$

The value of the relative crack length at fracture initiation is not obvious. Because of the negative energy–release–rate with crack extension $\partial G/\partial a$ behavior, a period of stable crack growth is generated in quasi brittle materials such as rock and concrete under increasing load before the point when $\alpha = \alpha_c$ is reached at which the toughness (for a quasi statically *growing* macrocrack) is evaluated. For a material with a flat R– curve, α_c is a unique value occurring for a minima in Y at the maximum load F_{max}. In this paper, the apparent fracture toughness at the initiation of a macrocrack is sought. The load at initiation, F_i, is not necessarily equal to F_{max}; in fact often $F_{max} > F_i$ as shown in Figure 3.6(a). For a chevron

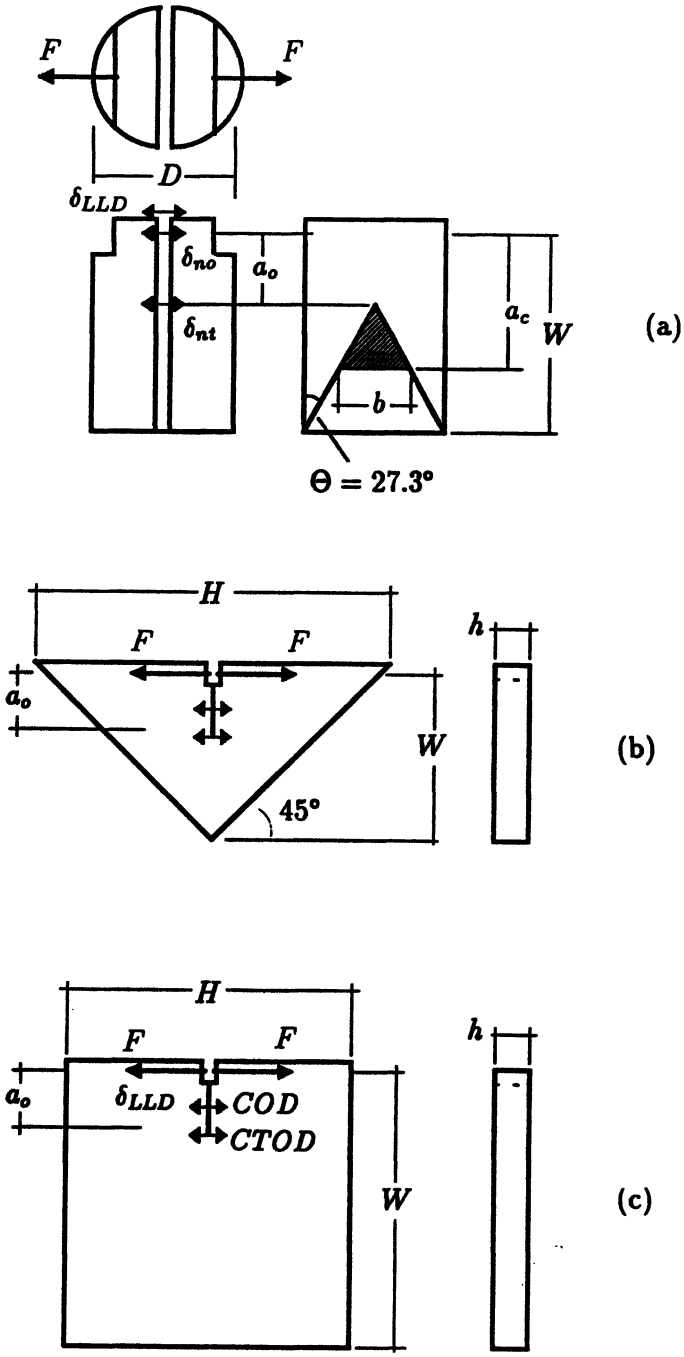

Figure 3.1: Schematic showing the (a) Short Rod Chevron Notched (*SRCN*), (b) Reverse Tapered (*RT*), and (c) Square Plate (*SP*) specimens for the apparent fracture toughness measurements.

notched geometry it is important to note that a stress–intensity–factor is not defined at $\alpha = \alpha_o$ due to the sharp apex of the notch, see Figure 3.1(a). Therefore, the load at the second abrupt load drop (crack initiation event) is used as the F_i, cf. Figure 3.6(a). The first crack initiation event corresponds to the load to generate an initial crack front width b. However, no direct measurements on the corresponding crack length were made. Instead, α is estimated as $(\alpha_c + \alpha_o)/2$. This is the approximate inflection point of the Y vs. α curve where gradually more positive $\partial G/\partial a$ specimen behavior contradicts stable propagation. The reader is referred to e.g. Mai and Atkins (1980) and DeFranco and Dempsey (1993) for details on crack growth stability.

In order to determine the K_I–expressions, linear elastic compliance measurements ($C(a) = \delta_{LLD}/F$) were performed on *RT* and *SP* specimens made of *PMMA* (polymethylmethacrylate). The dimensions of the compliance specimens are shown in Figure 3.2. The crack length was increased in increments to simulate the advancing crack. This was achieved by a band saw in steps of $\Delta\alpha \approx 0.05$ for $0.2 \leq \alpha \leq 0.75$ for the *RT* specimen and $0.2 \leq \alpha \leq 0.8$ for the *SP* specimen. To increase confidence in the compliance measurements (reciprocal slope of the linear load–deflection curve), averages of two different load cycles with zero to peak loading times of approximately 6 seconds were made at each crack length. The specimens were thus calibrated for the *FIFT*, the experiments were performed at -5°C.

The curve that best fit the compliance data plotted in Figure 3.2 for the *RT* was:

$$C_{RT} = \frac{10^2}{E't}\left[8.45\ln[(1-\alpha)^{-1}] - \frac{10.90}{(1-\alpha)} + \frac{2.04}{(1-\alpha)^2} + 8.66\right] \tag{3.3}$$

where t is the specimen thickness (also the crack front width) and E' is the effective elastic modulus (3.93 GPa for *PMMA*, Dempsey et al., 1989). The compliance for the *SP* was similarly found by a least squares curve fit to be:

$$C_{SP} = \frac{10^2}{E't}\left[\frac{1+\alpha}{1-\alpha}\right]^2 (0.14 - 0.55\alpha + 1.24\alpha^2 - 2.86\alpha^4 + 2.23\alpha^5) \tag{3.4}$$

The form of equation (3.3) is similar to that presented in Mai et al. (1975) and equation (3.4) with that in Murakami (1987). Through the Mode I LEFM energy–release–rate relationship

$$G_I = \frac{F^2}{2h}\frac{\partial C}{\partial a} = \frac{K_I^2}{E'} \tag{3.5}$$

K expressions were derived using the derivatives of equation (3.3) and equation (3.4). For the *RT* and *SP* geometries

$$K_Q = \frac{F_i}{t\sqrt{W}}\frac{Y(W/H,\alpha)}{(1-\alpha)^{3/2}} \tag{3.6}$$

for $W/H = 0.45$ (*RT*) and $W/H = 0.93$ (*SP*)

$$Y_{RT} = 5\sqrt{2}[8.45(1-\alpha)^2 - 10.90(1-\alpha) + 4.08]^{1/2} \tag{3.7}$$

$$Y_{SP} = 5[(1+\alpha)(0.02 + 0.56\alpha + 11.02\alpha^2 - 27.84\alpha^3 - \\ - 0.58\alpha^4 + 40.72\alpha^5 - 22.30\alpha^6)]^{1/2} \tag{3.8}$$

3.4 Experimental procedure

Freshwater ice cores and two ice blocks (500×500×450 mm^3) were collected from a pond formed in an abandoned limestone quarry, near Clarkson University, Potsdam, N.Y., during February, 1992. The average ice thickness was 450 mm. An interesting feature of this ice was found in each core and block: at approximately 200 mm from the ice surface a 50 mm thick bubble layer existed. The small bubbles were evenly distributed and made the ice opaque. At this location the ice was evidently saturated with air bubbles and air channels (Frannson and Stehn, 1993) but what caused this is unclear. This layer had some influence on the apparent fracture toughness of the ice, as is discussed later. The very warm ice pieces (air temperature ±0 °C) were wrapped in plastic, transported to a cold room at Clarkson and stored at -15°C to -20°C for between one and two months.

The non-turbulent waters of the pond had produced macrocrystalline S1 ice, as defined by Michel and Ramseier (1971), composed of irregularly shaped columnar crystals with vertical or near-vertical

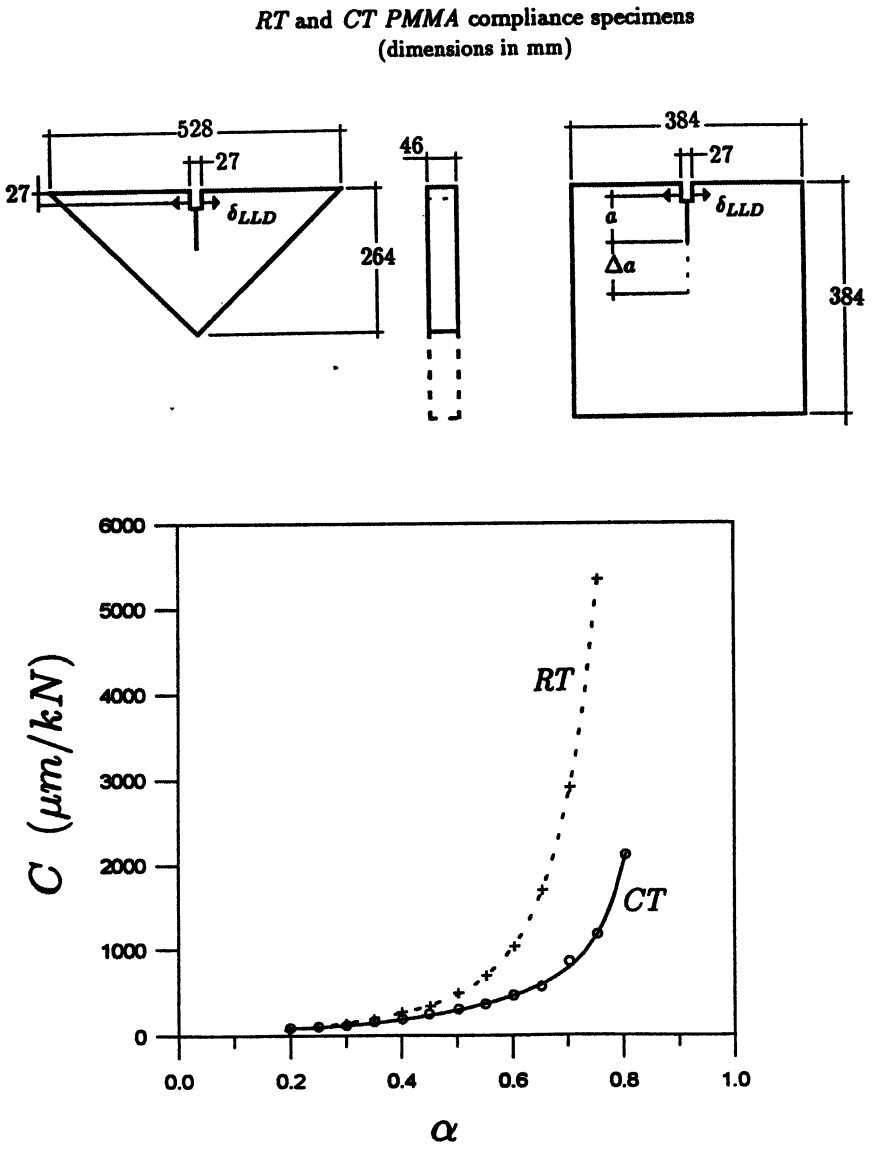

Figure 3.2: Dimensions of *PMMA* specimens and experimental elastic load–line compliance values plotted as compliance versus relative crack length.

c–axis orientation. The grain size showed an increase with depth, from 6.8±0.7 mm at the top (below the approximately 70 mm thick fine grained snow–ice layer) to 10.8±1.6 mm near the bottom. The columnar macro crystalline feature of the natural S1 ice is presented in Figure 3.3 which shows both (a) vertical and (b,c) horizontal thin sections.

The *c*–axis orientation of three different cores was measured at three different depths from horizontal thin sections using a Rigsby universal stage. A stereographic projection at each level of these *c*–axes are shown in Figure 3.4. The first level was approximately 50–70 mm from the top (99 grains measured), the second 120–160 mm from the top (95 grains) and the third was located 180 mm from the top (35 grains). In the first level 73 % of the grains were found to be vertical or near-vertical (to within 20 degrees inclination of the *c*–axis from vertical), in the second level 87 % (to within less than 15 degrees) and in the third level 97 %. Thus, it is evident that the *c*–axis of most grains was randomly and vertically or near–vertically oriented which is, by definition, S1 type ice.

The density was measured at approximately the same levels as the *c*–axis measurements by recording the mass of a known volume. The mass was measured on a digital scale with an accuracy of 0.1 g and volume was measured using digital calipers accurate to 0.01 mm. The average density was 906 ±10 kgm^{-3} at -16°C.

The length and chevron angle for the *SRCN* specimen was formed by a band saw. The *RT* and *SP* specimens were cut from two ice blocks with a chain–saw and made parallel by a planer. Each *RT* and *SP* specimen was formed to final dimensions using a band saw. Just prior to each test, the initial crack length was cut using a band saw. Each finished *SRCN* specimen had a diameter of 198 mm and each *RT* and *SP* specimen was approximately 46 mm thick (Table 3.1). The crack orientation and propagation direction were kept perpendicular to the plane of the ice sheet, i.e., a vertical crack propagating vertically downwards in the direction of crystal growth. In this manner, K_Q^{VV} (Stehn et al., 1993a) values are obtained. The crack initiation depth for the different specimens varied between 130 and 160 mm from the top surface of the ice sheet.

A sharp crack was introduced in each specimen immediately

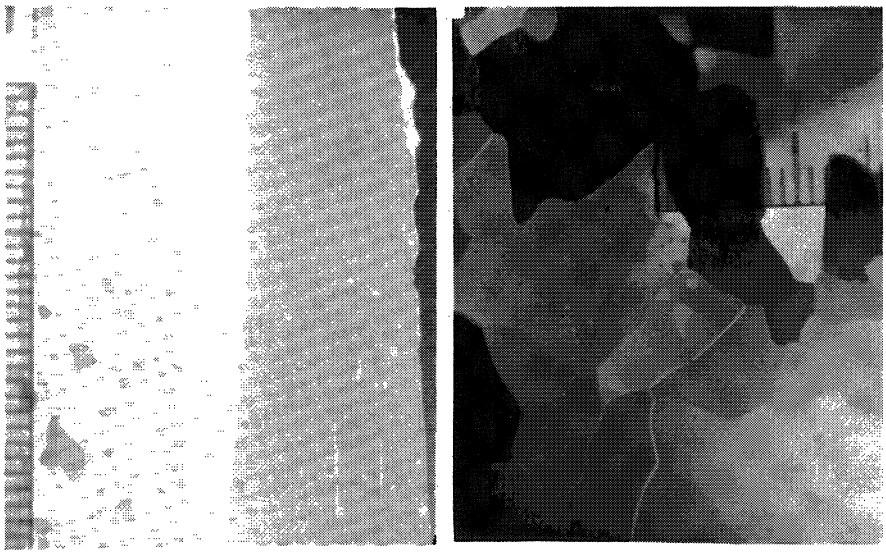

(a) (b)

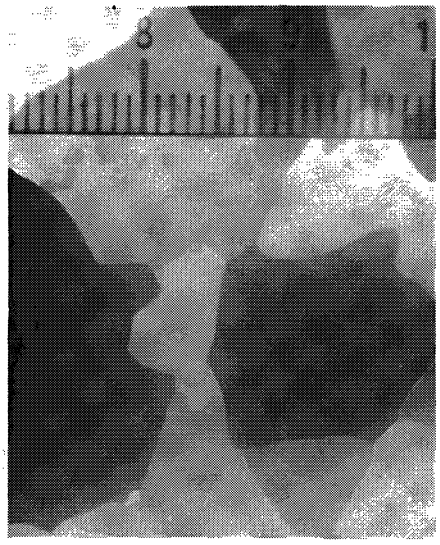

(c)

Figure 3.3: Macro structure of the S1 pond ice: (a) vertical thin section. Horizontal thin sections: (b) near the top, and (c) near the bottom.

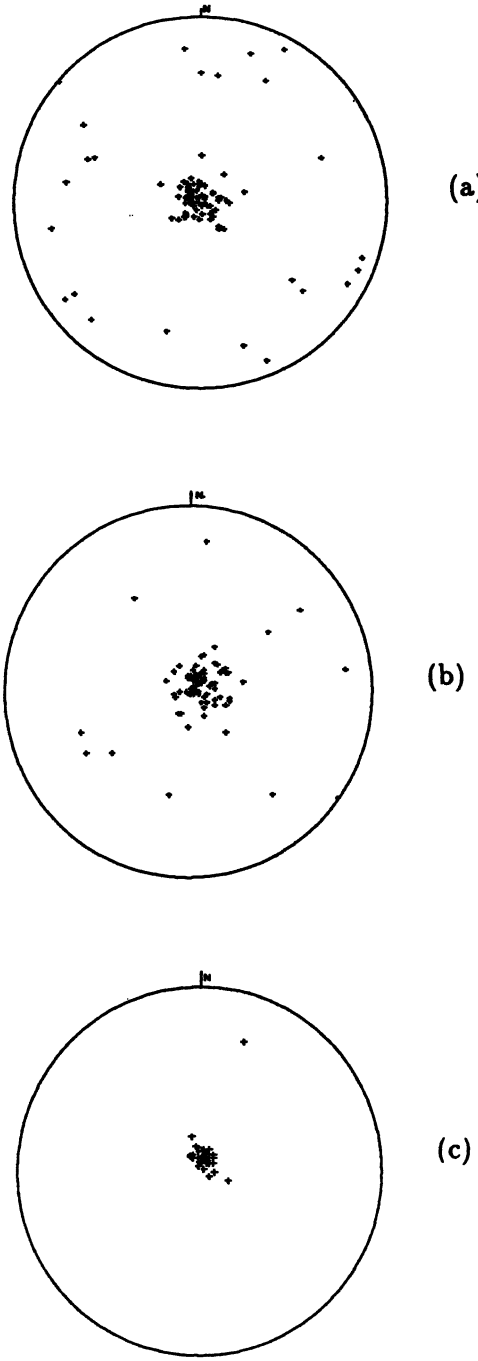

Figure 3.4: Stereographic projection of the c–axes orientation of nine horizontal thin sections: (a) 50–70 mm from the top, (b) 120–160 mm from the top, and (c) 180 mm from the top. A plot in the center indicates a vertical c–axis.

prior to the testing by scribing the band saw cut notch with a razor blade (Wei et al., 1991). This created a sharp, short crack with a wavy front. For the *SRCN* the sharp crack was created approximately 20 minutes prior to the test by scribing the notch with a fine tooth saw-blade. The crack tip opening displacements *CTOD*s and crack opening displacements *COD*s were measured during the fracture experiments using a procedure similar to that described by Wei et al. (1991), in which the error estimates using this technique can be found. A Kaman KD-2810-1U non-contacting displacement gauge (measuring range $25 \pm 0.025\mu$m) was frozen onto the specimen surface ahead of the notch and a Kaman KD-2310-1U measuring the *COD*s (measuring range $1000 \pm 0.1\mu m$) was attached at 27 (*SRCN*), 70 (*RT*) and 72 (*SP*) mm from the front face, see Figure 3.1(a–c). The load line displacements δ_{LLD} were measured using an crack opening displacement extensiometer.

All specimens were machined at between -15 and -27°C and were stored at the test temperature, -4°C, for at least 24 hours before testing. The tests were performed using the *FIFT*. Output signals from the transducers and the *FIFT* load–cell were processed by a Keithly Series 500 analog-to-digital converter connected to a Gateway 2000 model 486/33 microcomputer. Data sampling rates of 600 to 1000 Hz were used depending upon the estimated time to failure.

3.5 Result and discussion

The results of the 22 fracture tests together with specimen size data are presented in Table 3.1. The apparent fracture toughness, K_Q^{VV}, was computed using F_i, the crack initiation load, and equation (3.1) and equation (3.6); the effective elastic modulus was calculated using the initial linear part of the $F - \delta_{LLD}$ curves and equations equation (3.3) and equation (3.4) and equation (8) in Stehn (1993). The crack tip opening displacement at fracture $\delta_c = CTOD_c$, was also measured. The time to failure, t_f, ranged from 0.5 to 3.2 seconds resulting in a stress–intensity rate $\dot{K}$ of 50 to 370 kPa $\sqrt{\text{m}}\,\text{s}^{-1}$. There was no apparent dependence of K_Q^{VV} on t_f. All testing was performed at -4 °C.

Test #	H(or)$D/W/t$ (mm)	a_o/W	W/d_{av} a_o/d_{av} b/d_{av}	t_f (s)	K_Q^{VV} (kPa$\sqrt{\text{m}}$)	E (GPa)	δ_c (μm)
SRCN1	198/285/-	0.37		2.6	174	-	-
SRCN2	198/285/-	0.35		-	152	-	-
SRCN3	198/282/-	0.36		3.2	201	6.8	33
SRCN4	198/287/-	0.36	36	2.6	306	6.7	13
SRCN5	198/286/-	0.35	13	1.8	127	4.0	10
SRCN6	198/286/-	0.36	4	2.3	194	9.0	16
SRCN7	198/286/-	0.37		1.8	138	5.9	11
SRCN8	198/284/-	0.36		1.4	277	5.9	16
SRCN9	198/284/-	0.36		1.0	104	6.8	11
RT1	529/237/52	0.40		1.3	117	-	-
RT2	525/238/44	0.41		1.2	140	9.2	5
RT3	530/238/46	0.41	30	2.4	141	5.7	6
RT4	532/241/46	0.41	13	0.5	139	2.1	6
RT5	525/235/46	0.41	6	0.6	142	6.0	3
RT6	528/238/51	0.41		1.2	145	7.4	7
RT7	530/238/51	0.42		1.2	161	5.3	7
SP1	390/362/41	0.41		1.4	168	11.2	6
SP2	391/364/40	0.40	43	1.6	170	7.8	8
SP3	391/364/43	0.41	17	-	146	-	-
SP4	387/360/49	0.40	5	1.4	129	7.4	4
SP5	367/352/43	0.40		0.6	224	7.1	5
SP6	379/352/46	0.40		0.7	189	6.8	2

Note: b= crack front width; d_{av}= average grain size;
$\delta_c = \delta_{ntc}$ for the *SRCN* specimen.

Table 3.1: Experimental Data and Results.

Specimen type	K_Q^{VV} (kPa$\sqrt{\text{m}}$)		E (GPa)		δ_c (μm)	
	$\overline{x}$	σ_{n-1}	$\overline{x}$	σ_{n-1}	$\overline{x}$	σ_{n-1}
SRCN	186	68	6.4	2	16	8
RT	141	13	6.0	2	6	2
SP	171	33	8.1	2	5	2

Note: $\overline{x}$ = group mean value; σ_{n-1} = standard deviation

Table 3.2: Summary of test results.

Immediately obvious from these results, as can be observed in Table 3.2, is that the apparent fracture toughness is in relatively close agreement for the three fracture geometries tested. For comparable loading rates and same crack orientation/propagation direction and temperature, a statistical 95 % confidence interval for a difference in the mean values of K_Q^{VV} shows no significant differences between the three specimen types.

The K_Q^{VV} values measured using the *RT* specimen are the most consistent while the opposite is true for the E values, see Table 3.2. In all *RT* and *SP* specimens, the above mentioned bubble (snow–ice boundary) layer was present some distance ahead of the crack tip. The distance to this layer was generally much closer to the initial crack for the *RT* specimen, between 10 to 60 mm, and may have affected the modulus and also the crack propagation behavior. The crack extension was essentially planar. In two specific cases the crack extended out of the plane for shorter distances thereby leaving a bulge in one of the fractured specimen halves (the so–called *hill* type fracture, see Dempsey and Wei, 1989), see Figure 3.5(b) and Figure 3.7(e). However, when the propagating crack in all the *RT* and some *SP* specimens did run into the snow–ice layer, it veered away from its path, initially collinear with the notch, and followed the layer instead. This is consistent with a crack impinging on a weak interfacial layer (in this case the porous layer).

Both the *RT* and *SP* specimens show consistent δ_c values with almost the same mean value. The gauges were frozen on the lat-

eral surface of the specimen set at a distance of 5 mm apart, as in Dempsey et al. (1991). For the *SRCN*, the crack most likely propagates through crack jumping before the maximum load is reached (see discussion below); here the *CTOD* is defined for the first crack jump event only. Thus, it is more appropriate to use $\delta_{ntc}\ |_{\Delta a \to 0} \equiv\ CTOD_c$ to represent the *near* crack tip opening displacement at fracture. For the *SRCN* the lateral surface is at a distance of roughly 100 mm from the initial crack tip. It is expected that the measured δ_{nt} values are larger than the *CTOD*s due to the incorporated effect of elastic deformation. In the cases where the load versus COD plots revealed evidence of crack jumping, δ_{nt} was around 3 to 7 μm between each crack jump event.

Dempsey and Wei (1989) point out that variations in grain size and orientation of the variable microstructure of S1 ice are mainly responsible for the observed scatter in K_Q values. Crack initiation in the *SRCN* (having a small crack front width) is likely to be more influenced by the microstructure than the other two geometries. The local surroundings near the tip (grain boundaries and the local c–axis orientation), probably has a large influence on the crack initiation load. This is further accentuated by the high test temperature ($T = 0.98T_m$) that most likely causes the grain boundaries to be much weaker than the grain interior. An example of this is shown in Figure 3.5(a). It is important to note that the *hill* type fracture in Figure 3.5(b) is indicative of notch insensitivity and lack of polycrystallinity.

Typical load versus COD plots are shown in Figure 3.6(a–c). Only in Figure 3.6(a) is there any evidence of sub–peak load crack initiation and *stable* propagation. It is important to note that the ratchets in Figure 3.6(b) and Figure 3.6(c) are not associated with incremental cracking: instead, the appearance of the curves is caused by vibrations introduced by the electric drill during loading with the *FIFT*. In Figure 3.6(a), each abrupt change of slope in the curves is associated with a crack jump and a subsequent crack arrest as described in DeFranco and Dempsey (1990, 1991, 1993) and Stehn et al. (1993b). All tests were monitored using video where these crack jumps might be seen. Three crack jumping events, under decreasing load, are evident from both the δ_{nt} and

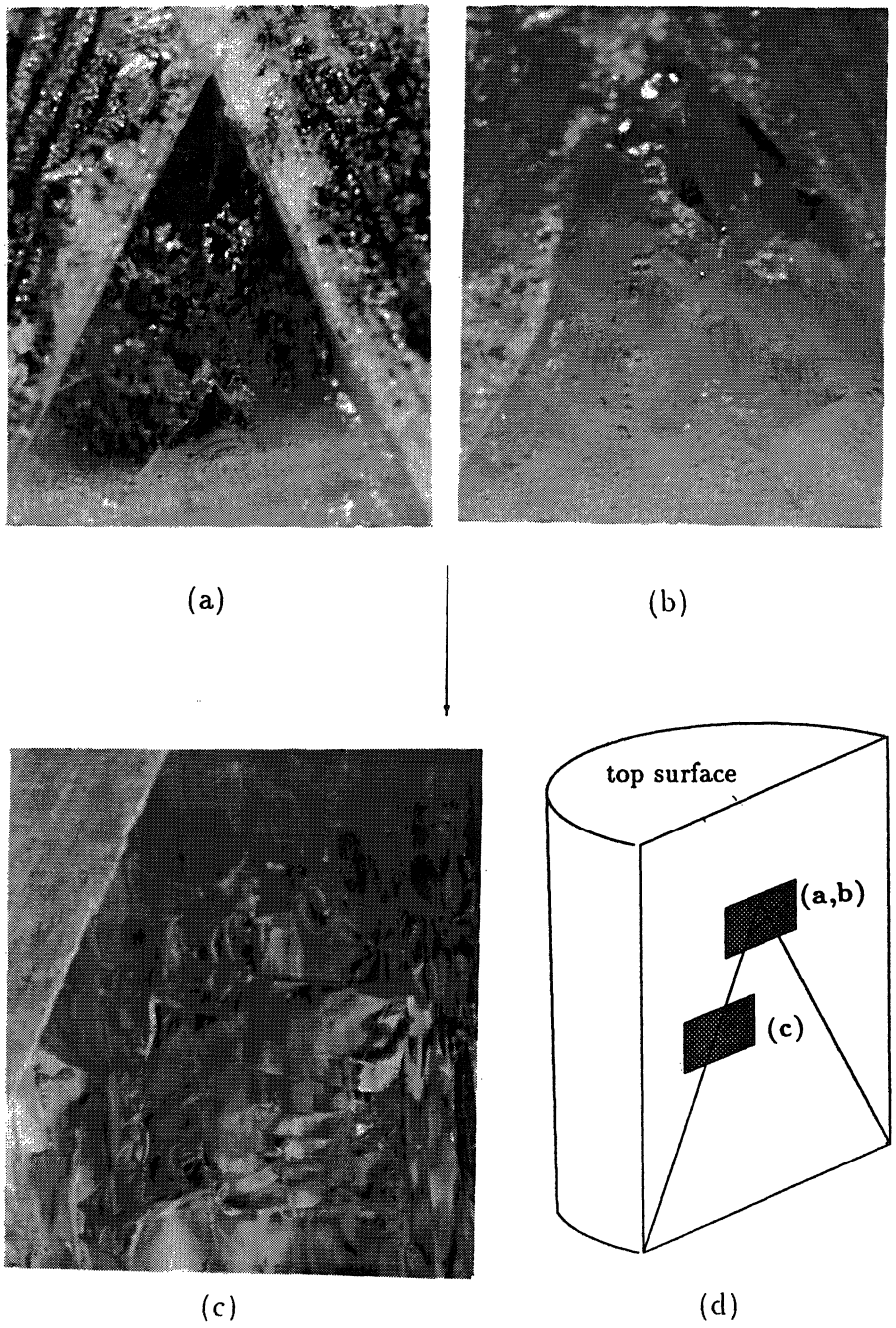

Figure 3.5: Notch tip crack initiation for (a) SRCN8 showing conchoidal in–plane fracture and for (b) SRCN9 where out of plane intergranular, *hill*–type, fracture is visible. (c) SRCN5 fracture surface and (d) schematic showing the position/orientation of each photograph. The arrow indicates the crack propagation direction.

δ_{no} measurements (see Figure 3.6 for notation). A characteristic fracture surface from a *SRCN* specimen is shown in Figure 3.5(c).

The unstable crack propagation behavior in the *RT* specimens, despite its strong geometric stability (DeFranco and Dempsey, 1991; 1993), was expected. Neither the video film nor the COD measurements showed any proof of incremental crack propagation. DeFranco and Dempsey (1991, 1993) achieved incrementally stable, *stick–slip*, crack propagation using a similar vesion of this geometry for cold saline ice. For warm saline ice, however, stable cracking was observed. Since crack growth stability is affected by the compliance of the *FIFT*, the specimen geometry (reflected through its $\partial G/\partial a$ characteristics) and the material (through its *R*-curve behavior), the crack stability apparently cannot be achieved in S1 ice using the *FIFT* without closed loop control. Another possible cause of the absence of stable crack propagation is the above mentioned snow–ice layer which may have prevented crack jumping from occurring. The fracture surface, Figure 3.7(a), shows very large cleavage steps and river patterns along the *whole* width of the initial notch. As the crack front progresses, conchoidal fracture becomes apparent, Figure 3.7(b). Visible on some fracture surfaces were horizontal lines similar to those occuring on the *SRCN* specimens.

No stable crack propagation was expected in the *SP* tests, and as shown in the typical Figure 3.6(c), none was detected during any test. In Figure 3.7(d) cleavage steps and planes are visible. The point(s) at which the radial lines originate is probably the crack initiation site. The rest of the surface is very flat, indicating fast, catastrophic, crack propagation. The strong influence of the microstructure is shown in Figure 3.7(e) where the crack ignored the sharpened notch tip and chose to fracture along a neighboring grain boundary instead.

3.6 Conclusions

- The apparent fracture toughness, K_Q, for the three fracture geometries tested show a reasonable similarity. The toughness was computed assuming the initiation of a stationary macrocrack from linear elastic, isotropic K_I solutions. Because S1

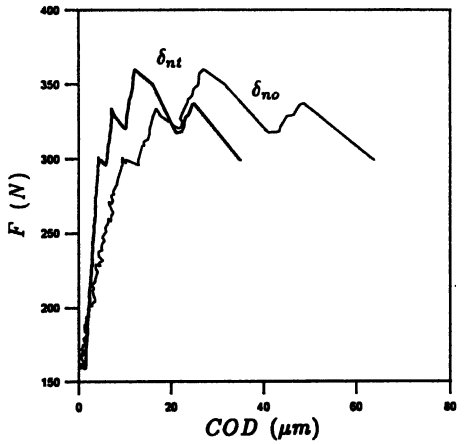

(a)

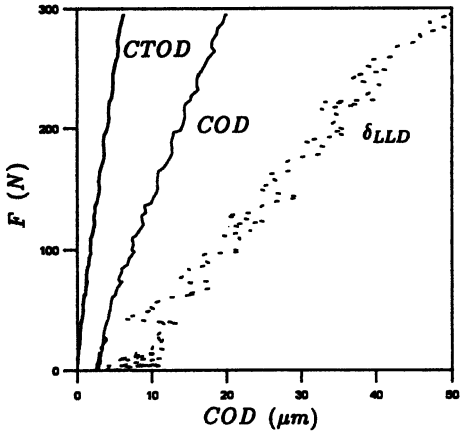

(b)

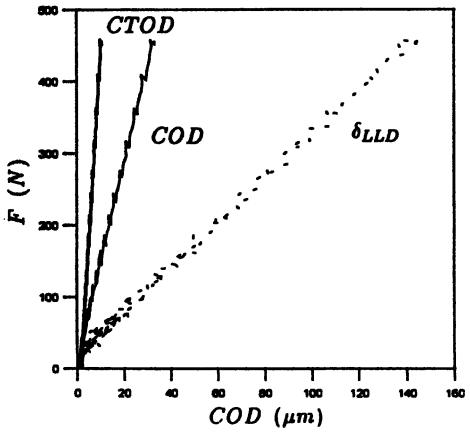

(c)

Figure 3.6: Load versus *COD* plots for (a) the *SRCN* specimen (SRCN9). Note that $\delta_{nt}, \delta_{no}\ |_{\Delta a \to 0} \equiv CTOD, COD$. The index n indicates that it is the *near* crack tip opening and crack opening displacements; (b) the *RT* specimen (RT6), and (c) the *SP* specimen (SP2).

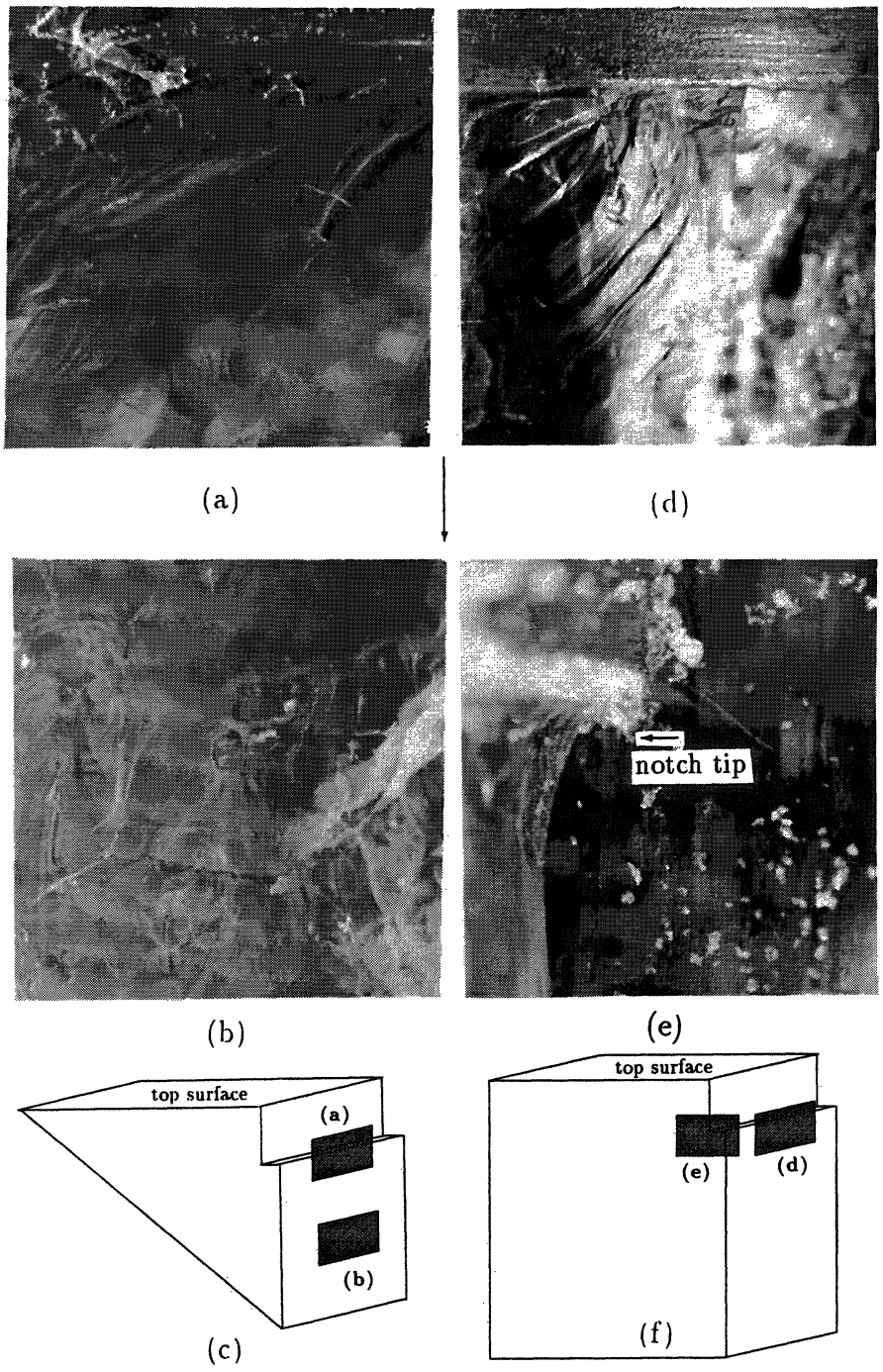

Figure 3.7: Fractography of (a) RT6, (b) RT5, (d) SP6 and (e) SP1 fracture surfaces; (c,f) schematic showing the position/orientation of each photograph. The arrow indicates the crack propagation direction.

ice is anisotropic and further because of its large grain size, *LEFM* size requirements were not fulfilled. However, for the range of specimen size to grain size tested, the K_Q variation is not significant.

- Even though the ice was warm, -4°C, all fractures were of a brittle nature. This is indicated by the short time to fracture and the evidence of cleavage fractures on the fracture surfaces of all specimens. The type of specimen had a marked influence on the character of the fracture surface.

- Due to the large grain size, the specimen size range was not sufficient to reduce the scatter. Even though relatively large $(W, a_o, h)/d_{av}$ ratios were maintained, the specimen size range was probably not sufficient to ensure notch sensitivity and polycrystallinity (Dempsey, 1991; Dempsey et al., 1992). Clear warning signs of sub–sized tests are the *hill* type fractures observed.

Paper **C**

Orientation effects on the fracture of pond (S1) ice

Lars M. Stehn
Department of Civil and Mining Engineering
Luleå University of Technology
S-951 87 Luleå, Sweden

Samuel J. DeFranco
Amoco Production Co.
P.O. Box 3385
Tulsa, OK 74102–3385, USA

John P. Dempsey
Department of Civil and Environmental Engineering
Clarkson University
Potsdam, N. Y. 13699–5710, USA

This chapter is a version of a paper where the original text has been formatted. The paper has been submitted for publication in:

Stehn L.M., DeFranco S.J. and Dempsey J.P., 1993. Orientation effects on the fracture of pond (S1) ice, *International Journal of Rock Mechanics and Mining Science & Geomechanics Abstracts*

Chapter 4

Orientation effects on the fracture of S1 ice

4.1 Abstract

The influence of structural anisotropy on the fracture toughness of S1 type freshwater ice was investigated by fabricating and testing three different fracture geometries from a single ice core. The ice was tested at -16°C using the Chevron Edge Notch Round Bar in Bending (*CENRBB*), a Chevron Notched Tension (*CNT*) specimen and the Semi Circular Bend (*SCB*) specimen. By this procedure, a complete anisotropic apparent fracture toughness (K_Q) characterization is possible from one core. The specimens can be prepared with very little machining. This approach is therefore suitable for both field and, as in this work, laboratory studies. Three models are presented for computation of the stress–intensity–factor expressions for these specimens. There is a wide scatter in the K_Q results and the apparent fracture toughness was higher for cracks perpendicular than for crack parallel to the c–axis and the columnar grains. Possible explanations for this ambiguous behavior are discussed in terms of microstructural influences and specimen size effects.

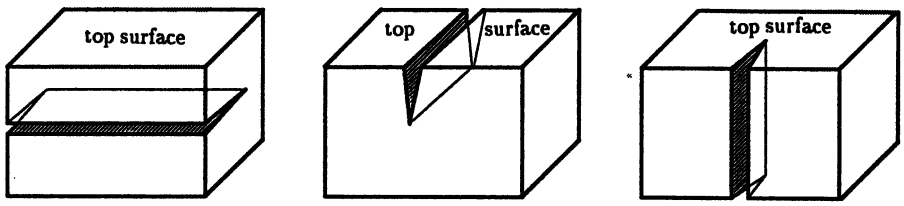

HH
horizontal orientation
horizontal propagation

VV
vertical orientation
vertical propagation

VH
vertical orientation
horizontal propagation

Figure 4.1: Notation for the three principal crack orientation and crack propagation directions.

4.2 Introduction

There are several mechanisms of ice fracture in an ice-structure interaction event: spalling, radial or circumferential cracking, non-elastic buckling and the flexural mode of failure. These fracture modes represent independent cracking cases with variations in the crack plane and crack propagation direction relative to the texture (shape of the grains) and fabric (orientation of the grains) of the ice. These crack plane and crack propagation directions are defined in Figure 4.1 according to the convention in Parsons et al. (1986). The first letter identifies that the crack plane is either (H) horizontal or (V) vertical; the second letter identifies that the direction of crack propagation is either (H) horizontal or (V) vertical.

Unseeded ice and often natural ice, formed in calm non-turbulent waters, forms so called S1 ice (Michel and Ramsier, 1971). This ice is composed of irregularly shaped columnar grains where there is a tendency for the average grain diameter to increase with depth due to the squeezing out of unfavorable oriented grains. The crystals have a preferred crystallographic orientation with a vertical or near-vertical c–axis.

The influence of anisotropy on fracture toughness of S1 freshwater ice has not received much attention in the literature (Kollé, 1981; Danilenko, 1985; Dempsey et al., 1988; Dempsey and Wei, 1989). Furthermore, it can only be speculated that the scatter typically observed in S1 ice testing is due both to specimen size effects and crack tip location versus the contiguous microstructure prior to initiation. When the fracture specimen is too small with respect to Linear Elastic Fracture Mechanics (*LEFM*) constraints and relative to the grain size, it is *notch insensitive* and a representative fracture event is not measured (Dempsey, 1989; Dempsey et al., 1992). When there are too few grains in the notch cross–section, the full confining effect imposed by neighboring grains (polycrystallinity) is not mobilized. Additionally, if the initial notch ends within a grain, the local orientation, not the global *c*–axis orientation measured over the whole aggregate, of that grain may in large part determine the energy needed to initiate and propagate a crack. This is specially important for large grained S1 ice.

Comparisons involving results from the literature concerning the influence of anisotropy on the fracture toughness of ice are difficult; this is mainly due to the variety of testing techniques, loading rates, test temperatures and ice types. However, a brief survey of previous investigations which have examined orientation (O'n) effects on the fracture toughness of S1 ice is presented. Kollé (1981) measured the influence of crystallographic anisotropy on freshwater S1 ice using three–point (3pt) bending specimens. A significant difference in fracture toughness was found between the hard-fail VV O'n and the HH O'n. The latter tests were performed on relatively small specimens where the b/d_{av}, crack front width to average grain size ratio, was only 2.5.

Danilenko (1985) used small sized compact tension specimens on fine grained S1 ice. However, no difference could be found among the six different directions studied. A limited number of tests per direction and a very low loading rate ($\dot{K} = 0.1$ to 2 kPa$\sqrt{\text{m}}\,\text{s}^{-1}$) is a possible explanation for the scattered data.

Dempsey and Wei (1989) addressed the issue of microstructural and textural effects on the fracture toughness of S1 ice tested using the 3pt bend geometry. The specimen sizes, $b/d_{av} = 1$ to 16, were

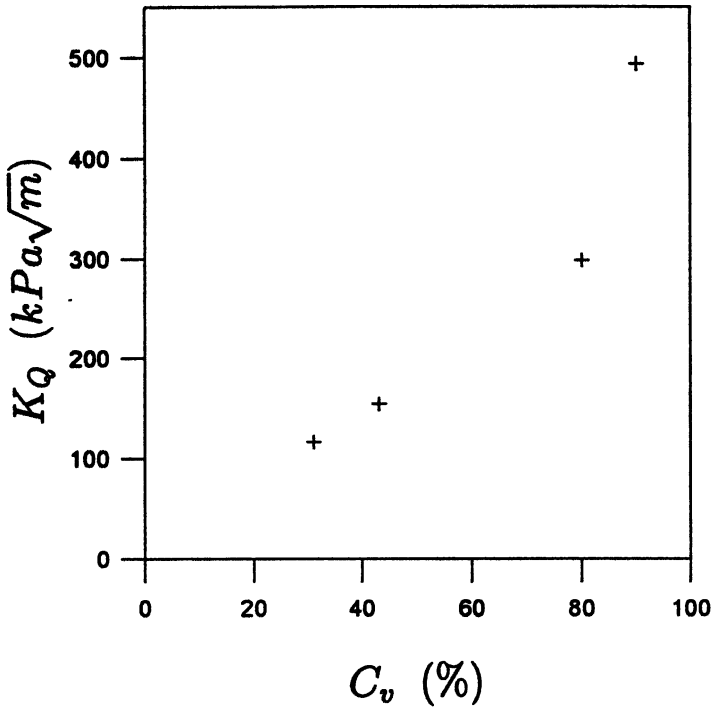

Figure 4.2: Effects of c–axis inclination on K_Q^H for freshwater S1 ice at -10°C. C_v is the percentage of grains having a vertical c–axis.

not large enough to reduce scatter although the authors reported lower K_Q for smaller grain sizes (brittle cleavage) and higher values for larger grain sizes (decohesive rupture). For cracking in the H O'n the apparent fracture toughness was found to have a pronounced dependence on the percentage of vertical c–axes. These results are shown in Figure 4.2. This paper investigates the influence of the structural anisotropy on the apparent fracture toughness corresponding to the initiation of a macrocrack using three different fracture specimens and freshwater S1 ice at -16 °C. Of real importance for field studies is the development of a fracture methodology using core specimens.

4.3 Fracture geomeries

A common feature of all of the above studies is the necessity to cut the specimens both horizontally and vertically in order to investigate the influence of structural anisotropy. In the field, this is a difficult and possibly dangerous procedure and requires thick ice for the specimens to be of a large size. This lead to the development of a method using core-based fracture geometries: the Chevron Edge Notch Round Bar in Bending (*CENRBB*), the Chevron Notched Tension(*CNT*), and the Semi Circular Bend (*SCB*), see Figure 4.3 (a–c). The concept originates from the ISRM (1988) suggested methods for determining the fracture toughness of rock. The idea is to minimize the amount of handling and machining by using specimens that are readily fabricated from core pieces. Consequently, a complete investigation of the influence of anisotropy on the fracture toughness can be made using easily obtained cores of ice. In the following, it is assumed that the core is vertically oriented. For each chosen core, the testing proceeds by i) fracturing the *CENRBB* that is a 3pt bend specimen with a chevron notch cut perpendicular to the core axis (the *HH* O'n); ii) from the remaining halves two *CNT* specimens are manufactured which have chevron notches cut parallel to the core axis (the *VV* O'n); iii) from the broken short rod halves, at least four *SCB* specimens can be fabricated. The 3pt bending configuration of the *SCB* has a straight notch cut that is perpendicular to the notches in both of the other specimens (the *VH* O'n). In this way, the three principal crack O'ns, outlined in Figure 4.1, can be obtained from one ice core.

The shape function for the standard short rod chevron notched specimen can be found in e.g. Matsuki et al. (1991), but is not known for the *CNT* because the different mode of loading. The *SCB* geometry was apparently first investigated by Chong et al. (1987a). The latter authors, however, did not describe or present a thorough fracture mechanics analysis of the *SCB*. Furthermore, the span/diameter ratio for the *CENRBB* was too small to utilize existing expressions. In order to investigate the influence of the structural anisotropy of S1 ice on the fracture toughness values associated with the *CENRBB, CNT* and *SCB*, the K_I–expressions

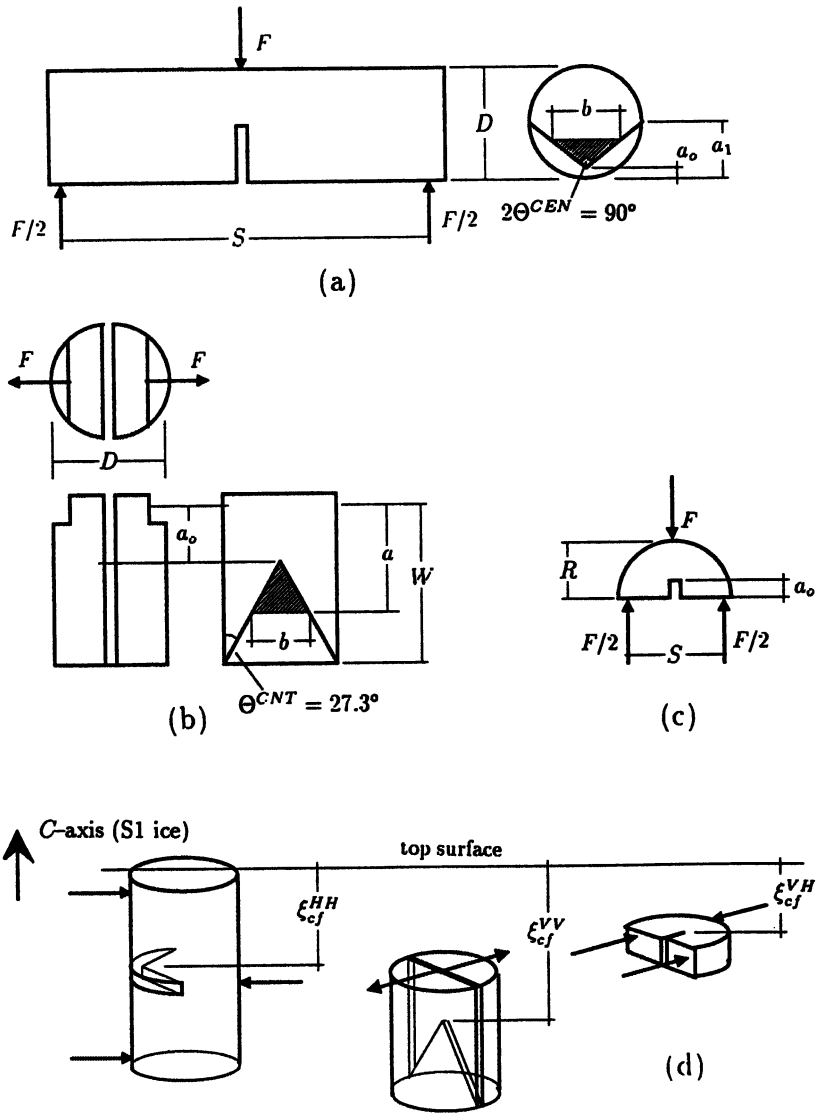

Figure 4.3: (a) Chevron Edge Notched Round Bar in Bending (*CENRBB*), (b) Chevron Notched Tension (*CNT*) specimen, and (c) Semi Circular Bend (*SCB*) specimen; (d) Schematic showing the specimen orientation relative to the crystallographic orientation.

were determined by a combination of an analytical beam model based on Kanninen's spring foundation model (Kanninen, 1973), the finite element method and the weight function method. Inherent in these *LEFM* expressions are the assumptions that the material is homogeneous, elastic and isotropic.

Caution should be exercised in applying isotropic theory to estimate anisotropic material performance. In anisotropic materials, the critical stress–intensity–factor is dependent on the crack orientation, Wu (1967). To apply the *LEFM* concept to the prediction of fracture in ice, the crack must be oriented along the principal direction of elastic symmetry. The direction(s) in which K_{Ic} is minimum is then always constant, i.e., the critical orientation of the crack is known. Furthermore, the direction of crack propagation must be essentially planar and collinear with the original crack.

For this reason, the *apparent fracture toughness* is determined here instead of the plane strain fracture toughness (or K_{Ic}). Note that these distinctions are not necessary if the initiation of crack growth is identified in terms of the critical energy release rate (G_{Ic}), but only if the latter is deduced specifically through the specimen compliance.

4.4 Experimental procedure

Freshwater ice cores were collected from a pond formed in an abandoned limestone quarry, near Clarkson University, Potsdam, N.Y., during March, 1992. The average ice thickness was 450 mm. An interesting feature of this ice was found in each core; at approximately 200 mm from the ice surface a 50 mm thick bubble layer existed. The small bubbles were evenly distributed and made the ice opaque. At this location the ice was evidently saturated with air bubbles and air channels (Fransson and Stehn, 1993) but what caused this is unclear. This layer had a strong influence on the fracture behavior in the *HH* O'n, as is discussed later. The very warm ice cylinders (air temperature +2 °C) were wrapped in plastic, transported to a cold room at Clarkson and stored at -15°C to -20°C for approximately two months.

The non-turbulent waters of the pond had produced macrocrys-

talline S1 ice, as defined by Michel and Ramseier (1971), composed of irregularly shaped columnar crystals with vertical or near-vertical c–axis orientation. The grain size showed an increase with depth, from 6.8±0.7 mm at the top (below the approximately 70 mm thick fine grained snow–ice layer that was removed before machining the specimens) to 10.8±1.6 mm near the bottom. The columnar macrocrystalline feature of the natural S1 ice is presented in Figure 3.3 which shows a vertical and horizontal thin sections from specimen CNT3g.

The c–axis orientation on three different cores at three different depths was measured by a universal stage on horizontal thin sections. A stereographic projection at each level of these c–axes are shown in Figure 3.4. The first level was approximately 50– 70 mm from the top (99 grains measured), the second 120–160 mm from the top (95 grains) and the third was located 180 mm from the top (35 grains). In the first level 73 % of the grains were found to be vertical or near-vertical (to within 20 degrees inclination of the c–axis from vertical), in the second level 87 % (to within less than 15 degrees) and in the third level 97 %. Thus, it is evident that the c–axes of most grains was randomly and vertically or near–vertically oriented which is, by definition, S1 type ice.

The density was measured on different cores at approximately the same levels as the c–axis measurements by recording the mass of a known volume. The mass was measured on a digital scale with an accuracy of $0.1g$ and volume was measured using digital calipers accurate to 0.01 mm. The average density was 906 ±10 kgm^{-3} at -16°C.

The *CNT* specimens were cut from the ice cores so that the above mentioned bubble layer not ended up within the notch section (uncracked ligament). This is also the case for the it SCB specimens that were formed from broken *CNT*s. The *CENRBB* were made using the whole core length. For the latter, the chevron notch was, in all cases, cut within the bubble layer. The lengths and chevron angles for the *CENRBB* and *CNT* specimens were formed by a band saw. The proper notch angles, 90° (Figure 4.3a) and 27.3° (Figure 4.3 b), respectively, were ensured by using simple notch cutting fixtures similar to that described in the ISRM (1988). The special

groove in the front face of the *CNT* specimens was milled by a 20 mm vertical endmill. The *SCB* specimens were formed from broken *CNT* specimens and the straight face, originally the uneven crack plane of the *CNT*, was planed with a planer–joiner.

A sharp crack was introduced in each specimen immediately prior to the testing by scribing the notch with a razor blade (Wei et al., 1991). This created a sharp, short crack with a wavy front. The crack tip opening displacement s *CTOD*s and crack mouth opening displacement s *CMOD*s were measured during the fracture experiments using a procedure similar to that described by Wei et al. (1991), in which the error estimates using this technique can be found. A Kaman KD-2810-1U non-contacting displacement gauge (measuring range $25 \pm 0.025 \mu m$) was frozen onto the specimen surface ahead of the notch and for the *CENRBB* and *CNT* specimens, a Kaman KD-2310-1U measuring the *CMOD*s (measuring range $1000 \pm 0.1 \mu m$) was also attached near the crack mouth.

All specimens were machined and tested at -16°C. The tests were performed on an Instron 8500 testing frame with crosshead velocities of 0.01 (*CNT*), 0.02 (*SCB*) and 0.04 (*CENRBB*) mm s^{-1}. The transducers' output signals were processed by a Keithly Series 500 analog-to-digital converter connected to a Gateway 200 model 486/33 microcomputer. Data sampling rates of 300 to 600 Hz were used depending upon the stroke rate.

4.4.1 The Cevron Edge Notch Round Bar in Bending (CENRBB)

The (*CENRBB*) has been used by Ouchterlony (1982) for fracture toughness, crack resistance, *R*–curve behavior, and *J*–integral resistance measurements on rock. The uncracked ligament of the notched specimen has the form of a *V* or chevron (Figure 4.3 a). Because the *CENRBB* exhibits a negative energy-release-rate with crack extension $\partial G/\partial a$[1] behavior, a period of stable crack growth

[1]Crack growth stability requires the equality of the crack driving force and the crack growth resistance and also that the rate of change in the resistance of fracture is greater or equal to the rate of change in the crack driving force, i.e., $G = R$ and $\partial G/\partial a \leq \partial R/\partial \Delta a$

is generated in quasi brittle materials such as rock and concrete under increasing load before the point at which the toughness (for a quasi statically growing macrocrack) is evaluated. The compliance calibrations for the *CENRBB* shape functions were determined by Ouchterlony (1984) from systematic experiments on aluminum specimens and recently by Matsuki et al. (1991) using a boundary element method.

The aim of this paper was to use the standard specimen configuration for the *CENRBB* specimen in the ISRM (1988) suggested methods. However, the total ice thickness made it impossible to maintain a S/D (span/diameter) ratio of 3.33, so the ratio of S/D=1.7 used in this study required a new shape function.

The calibration was made by a 3–D finite element analysis using the general finite element program *ANSYS*. A *CENRRB* specimen was modeled with dimensions according to Table 4.1 with D = 1m and E' = 1GPa. Only half of the specimen was analyzed, taking into account the symmetry. The thickness of the chevron notch was 0.03D which is the thickness of the band saw cut. The notch was modeled using 10 volumes, each of several elements, with baselines perpendicular to the line of loading, see Figure 4.4. The top volume was $0.128D$ high, the other nine volumes $0.078D$ high. The complete FE mesh was made of nearly 3800, four–node, 3–D solid tetrahedron elements. The average stress–intensity–factor K_I was determined using the compliance method. For each specified relative crack length (α^{CEN}), a load of 1 kN was applied, the load–line displacement was averaged from nodal displacements and the compliance C was computed. The nodes in the top volume was not included due to the proximity of the concentrated load. The crack length was then increased by removing a volume of elements in the notch. In this way, an incremental increase in the crack length of $\Delta\alpha^{CEN} = 0.078$ was modeled. A new mesh was then generated. This method was repeated for nine relative crack lengths, $\alpha_o^{CEN} \leq \alpha^{CEN} \leq 0.8$ where $\alpha^{CEN} = a/D$ (a is the crack length); in terms of the load–line displacement (δ_{LLD}) the compliance $C = \delta_{LLD}/F$ where F is the load. From the potential energy release rate and the *LEFM* relationship $G = K^2/E'$

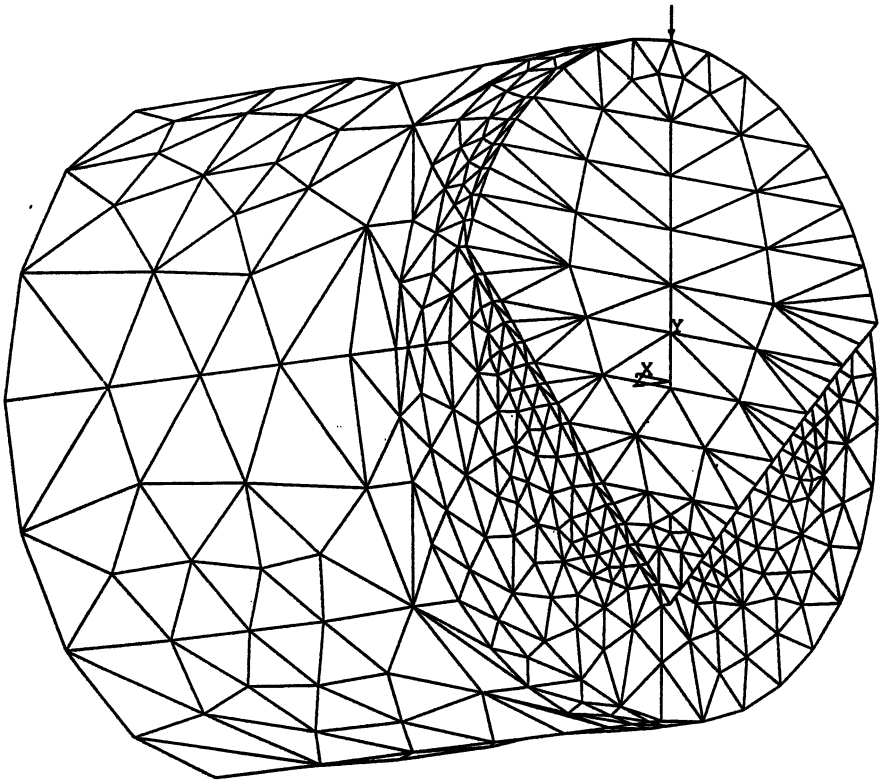

Figure 4.4: The 3–D finite element *CENRBB* mesh

$$G_I = \frac{K_I^2}{E} = \frac{F^2}{2b} \cdot \frac{\partial C}{\partial a} \tag{4.1}$$

where b is the actual crack front width $= 2D(\alpha^{CEN} - \alpha_o^{CEN})$ and $E' = E$ for plane stress and $E/(1-\nu^2)$ for plane strain, an average K_I value is obtained in the form:

$$K_I = \frac{F}{D^{3/2}} Y_{CEN}(\alpha_o^{CEN}, \alpha^{CEN}) \tag{4.2a}$$

$$Y_{CEN} = \left[\frac{1}{4}\frac{\partial \hat{C}}{\partial \alpha^{CEN}} \frac{1}{(\alpha^{CEN} - \alpha_o^{CEN})}\right]^{0.5} \tag{4.2b}$$

Here $\hat{C} = CE'D$ is the non–dimensional compliance. The compliance data obtained from the FE modeling is shown in Figure 4.5. $\hat{C}$ was determined as a function of crack length using a curve fitting technique after Ouchterlony (1984). The curve that best fit the compliance data in Figure 4.5 was:

$$\hat{C} = 25.2 + 47.7\alpha^{2.5} + 246\alpha^{6.5} + 1104\alpha^{16} \tag{4.3}$$

From equation (4.2) and equation (4.3) the apparent fracture toughness is ultimately evaluated as:

$$K_Q^{HH} = \frac{F_i}{D^{3/2}} 5.46 \left[\frac{\alpha^{1.5} + 13.4\alpha^{5.5} + 148\alpha^{15}}{(\alpha - \alpha_o)}\right]^{0.5} \tag{4.4}$$

here F_i is the crack initiation load. In this paper the apparent fracture toughness at initiation of a macrocrack is sought. For a chevron notched geometry it is important to note that a stress–intensity–factor is not defined at $\alpha = \alpha_o$ because of the sharp apex of the notch, see Figure 4.3(a,b). In these tests, the maximum load, corresponding to the *second* crack initiation event, is used as the crack initiation load. The first crack initiation, the pop–in Figure 4.6(a), generates an initial crack font width b. However, no direct measurements on the corresponding crack length were made. Instead, α is arbitrarily estimated so a minima in Y_{CEN} is obtained. This occurs for $\alpha \approx 0.331$. It is worth to notice that, for a material with a flat R–curve, the α corresponding to a minima in Y (often denoted α_c) is a unique value occurring at the maximum load F_{max}.

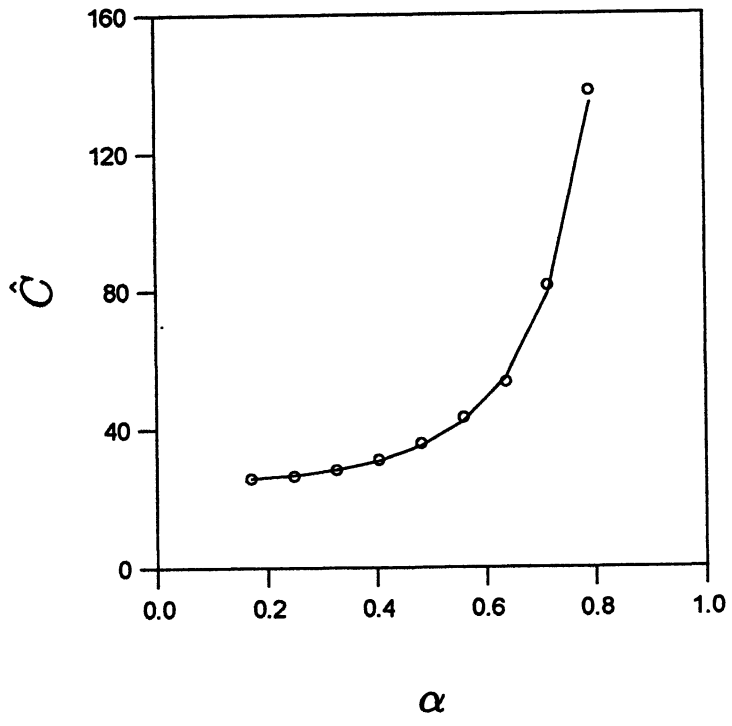

Figure 4.5: Elastic load–line compliance values obtained from the *FE* model plotted as dimensionless compliance ($\hat{C}$) versus relative crack length.

Test Type O'n	Dimensions	D (mm) t (mm)	No. of Tests
CENRBB HH	S=1.7D a_o=0.17D a_1=0.64D $2\Theta^{CEN} = 90°$	198	4
CNT VV	W=1.44D a_o=0.46D $2\Theta^{CNT} = 54.6°$	198	6
SCB VH	S=0.8D a_o=0.14D	198 54-58	13

Note: A small variation in the dimensions exists as a result of the specimen fabrication

Table 4.1: Specimen dimensions

To determine the apparent fracture toughness for the HH O'n in S1 ice, K_Q^{HH}, four tests were performed using this geometry, see Figure 4.3(a) and Table 4.1 for dimensions.

4.4.2 The short rod Chevron Notched Tension specimen (CNT)

The (*CNT*) specimen was first used, in a parallel research effort, by Stehn et al. (1993b). The complete details of these tests and the evaluation of the results are presented in the latter paper. The standard Short Rod Chevron Notched specimen *SRCN* was first proposed by Barker (1977, 1978). Barker used the *SRCN* for fracture toughness determination of aluminum and rocks, and later, Nixon (1984) and Nixon and Smith (1987) used it to measure the fracture toughness and effects of reinforcement on freshwater ice.

The *beam–like* character of the *CNT* specimen was conveniently modeled by a one– dimensional beam on elastic foundation model (Kanninen, 1973). The Winkler foundation is used to model the uncracked area of the specimen which allows the determination of

a theoretical compliance function. The geometry, boundary conditions and stress–intensity– factor solution are presented in Stehn et al. (1993b). The K_I–expression for the *CNT* is ultimately given by:

$$K_Q^{VV} = \frac{F_i}{R^{3/2}} \left(\frac{0.991}{(\alpha^{CNT} - \alpha_o^{CNT})^{1/2}} [Y_F - Y_M] \right) \tag{4.5}$$

where R is the core radius, W the specimen length and $\alpha^{CNT} = a/W$. The two functions $Y_F(\alpha^{CNT}, W/R)$ and $Y_M(\alpha^{CNT}, W/R)$ are given as:

$$Y_F = \alpha(W/R)C_3C_1 + C_2(\eta=-1) \tag{4.6}$$

$$Y_M = \left(\frac{\alpha^2(W/R)^2C_3^2 + 2\alpha(W/R)C_3C_2(\eta=1) + C_1}{2\alpha(W/R)C_3 + 2C_2(\eta=1)} \right) C_1 \tag{4.7}$$

in which

$$C_1 = \frac{\sinh^2 \lambda c + \sin^2 \lambda c}{\sinh^2 \lambda c - \sin^2 \lambda c} \tag{4.8a}$$

$$C_2(\eta) = \frac{\sinh \lambda c \cosh \lambda c + \eta \sin \lambda c \cos \lambda c}{\sinh^2 \lambda c - \sin^2 \lambda c} \tag{4.8b}$$

$$C_3 = 1.760 \tag{4.8c}$$

In equations (4.8a,b) $\lambda c = 1.760(1-\alpha)(W/R)$; α is the current relative crack length. This specimen promotes stable crack extension, crack jumping, over uncharacteristically large portions of the initial uncracked ligament. By the *COD* measurements, each crack jump identified on the fracture surface could be correlated to the current load and crack length. By the same arguments, about the chevron notch stress–intensity–factor, as before; the load at the second abrupt load drop (crack initiation event), cf. Figure 4.6(b), is used as the initiation load corresponding to the K_Q^{VV} value. The first crack jump event corresponds to the load to generate an initial crack front width b.

A total of six *CNT* tests were performed using the geometry in Figure 4.3(b) and Table 4.1. The cracking O'n was vertical and the propagation direction was vertical downwards and parallel to the c–axis yielding K_Q^{VV} values.

4.4.3 The Semi Circular Bend specimen (SCB)

The Semi Circular Bend (*SCB*) specimen was introduced by Chong et al. (1987a and b) for fracture studies on oil-shale. The *SCB* specimen is a single edge notch beam loaded in 3pt bending as shown in Figure 4.3(c). It has also been used for mixed mode fracture studies, Chong and Kuruppu (1988), with the edge crack cut at an angle to the loading direction.

In a recent paper by Adamson et al. (1993), a stress–intensity–factor solution for all crack lengths ($\alpha_o^{SCB} \leq \alpha^{SCB} \leq 1$) for the *SCB* is presented using the weight function method. In the weight function method the stress–intensity–factor for a body is determined from a reference stress–intensity–factor and reference crack face displacement that is generated (or known) for a reference load case. A specific stress–intensity–factor is than obtainable for any type of loading. In Adamson et al. (1993), an FEM analysis was conducted to get the stress distributions for the 3pt bending loading case. The reference stress–intensity–factor and reference crack face displacement were obtained by examining limiting cases of known solutions and by curve fitting results found using the general finite element program *ABAQUS* *J*–contour calculations. The reader is referred to Adamson et al. (1993) for details. The K_I–expression for the *SCB* for $S/R = 1.6$ is given by:

$$K_Q^{VH} = \frac{F}{tR^{1/2}} \frac{(\pi\alpha^{SCB})^{1/2}}{(1-\alpha^{SCB})^{3/2}} Y_{SCB} \tag{4.9}$$

here $\alpha^{SCB} = a/R$, t is the specimen thickness and

$$\begin{aligned} Y_{SCB} \;=\; & (2.724 - 11.299\alpha + 50.105\alpha^2 - \\ & -158.231\alpha^3 + 313.312\alpha^4 - 362.563\alpha^5 + \\ & +222.599\alpha^6 - 55.713\alpha^7) \end{aligned} \tag{4.10}$$

A total of 13 tests were performed to determine, K_Q^{VH}, the apparent fracture toughness for a vertical crack propagating horizontally and parallel to the c–axis using the *SCB* geometry, see Figure 4.3(c) and Table 4.1 for dimensions.

ID			F_t	K_Q			δ_c		
#	O'n	ξ_{cf}	(N)	(kPa$\sqrt{\text{m}}$)	$\overline{x}$	s	(μm)	$\overline{x}$	s
CEN1a			2619	190			-		
CEN2b			3169	230			21		
CEN3c	HH	150	2172	158	270	157	13	22	8
CEN4d			6902	501			33		
CNT1e		125	1296	215			44		
CNT2f		120	737	97			14		
CNT3g	VV	195	579	78	111	58	26	33	11
CNT4h		145	553	74			37		
CNT5i		120	441	59			40		
CNT6j		140	979	142			38		
SCB1e		160	993	130			4.0		
SCB2e		160	1642	197			4.2		
SCB3e		215	912	128			3.7		
SCB4e		215	846	108			2.3		
SCB5f		185	1842	212			7.0		
SCB6f		245	910	114			3.6		
SCB7h	VH	215	663	85	126	41	2.2	3.3	1.5
SCB8h		265	734	89			3.2		
SCB9i		135	940	123			0.7		
SCB10i		195	1084	141			4.1		
SCB11j		195	596	75			1.8		
SCB12j		190	1053	138			3.9		
SCB13j		245	787	95			2.5		

Note: $\overline{x}$ = group mean value; $s = \sigma_{n-1}$ = standard deviation

Table 4.2: Test data and results

4.5 Results and discussion

The experimental results are summarized in Table 4.2 where each test is identified by a specimen type letter, a sequence number and the core from which the specimen was made. O'n is the orientation of the crack plane and crack propagation direction, ξ_{cf} is the approximate crack initiation depth (mm) from the top surface (Figure 4.3d), F_t is the crack initiation load used to calculate K_Q in equation (4.4), equation (4.5) and equation (4.9)and $\delta_c = CTOD_c$ is the crack tip opening displacement at fracture. To facilitate comparisons of the different crack orientation and propagation di-

rections, the mean values and standard deviations of the different specimens are presented. All testing was performed at -16 °C and the crack front width to average grain size b/d_{av} ratios varied as 4 (*CENRBB* and *CNT*) and 8 (*SCB*). The time to failure ranged from 3 to 23 seconds resulting in an approximate stress- intensity rate $\dot{K}$ of 5 to 50 kPa $\sqrt{\text{m}}\,\text{s}^{-1}$.

In each case the crack propagated along an essentially straight line collinear with the original crack. Hence, the stress–intensity–factors determined for an isotropic case are applicable.

The typical *F–CTOD* plots reveal a clear difference in fracture behavior between the *CENRBB*, Figure 4.6(a), the *CNT*, Figure 4.6(b) and *SCB*, Figure 4.6(c). For the *SCB*, the initiation of a stationary macrocrack was followed by unstable fracture. The load versus time plots were linear and the maximum load could be identified in each case at the instability point. The *bump* in Figure 4.6(a) is probably a pop–in (crack initiation), but no further crack extension is visible. This behavior of the *CENRBB* specimen is ambiguous and will be discussed later. However, the *CNT* responded completely differently. Figure 4.6(b) shows the F versus δ_{nt} plot for specimen CNT3g. In this case $\delta_{nt}\,|_{\Delta a \to 0} \equiv CTOD$ is defined as the *near* crack tip opening displacement since the gauges were attached to the specimen surface at a distance of 100 mm from the initial crack tip. The changes of slope in this curve is associated with crack jumps where the crack extension occurs under decreasing load. This definite change in slope is also evident in the F–time and δ_{nt}–time spaces. An unstable fracture never occurred; the incremental crack extension took place along the whole notched ligament. A complete discussion and analysis of the results using the *CNT* specimen is enlarged upon in Stehn et al. (1993b).

A statistical 95% confidence interval for a difference in means showed, surprisingly, a significantly *lower* apparent fracture toughness for the–with respect to the c–axis orientation–hard fail O'ns VH and VV with respect to the HH O'n.

The unexpected behavior, probably caused by a too small specimen span, of the *CENRBB* specimen must be taken into account. The small S/D ratio induced higher shear stresses in the specimen. The significant increase in specimen stiffness is clearly evident from

the finite element analysis. Compared to the *ISRM* (1988) standard specimen configuration, Matsuki et al. (1991), the small S/D ratio gave a 68 % lower value of K_I, and a 6 % decrease in the compliance at the critical crack length. In addition, there was only weak evidence, by the *CTOD* and the *CMOD* measurements, of pop–in features on the *F–CTOD* plots indicating crack growth prior to unstable cracking. No crack growth could be visually detected. Because the *CENRBB* exhibits a negative $\partial G/\partial a$ behavior, a period of stable crack growth could be expected.

It is important to note that these preliminary tests include too few tests for the observed trends to be statistically valid. It is recognized that a larger amount of data is needed. The two size effects (mentioned in the introduction and emphasized by Dempsey and Wei, 1989) are predominantly responsible for the scatter. An intriguing possibility is that the ambiguous (crystallographic) anisotropy behavior found is caused by another microstructual effect; namely, the bubble layer. As mentioned before, this layer was very close to the notch for the *CENRBB* specimens. It can be speculated that the bubble layer increase the deformation capability of the ice specimen; so that, in a sense, it shields the crack so that the effective stress–intensity–factor is reduced. Thus, the apparent macroscopic fracture toughness characterizes a tougher material than that which the crack tip experiences. In fact, two specimens, not included in these results, did not break at the notch but suffered a shear–like failure, originating from the supports, instead, i.e., the specimens did not *feel* the notch. It is also possible that the size and configuration of a specimen influences the results so that the value of K_Q becomes more or less dependent on the anisotropy of the ice properties.

The affect of c–axis inclination (the percentage of grains having a vertical c–axis) on K_Q is notable. The *SCB* results are on average higher and more consistent, i.e., having lower standard deviation, than the *CNT*. This is probably caused by the difference in crack initiation depths. For the latter, the initiation is generally higher up in the ice sheet where the c–axis is not so predominantly vertical as it is further down.

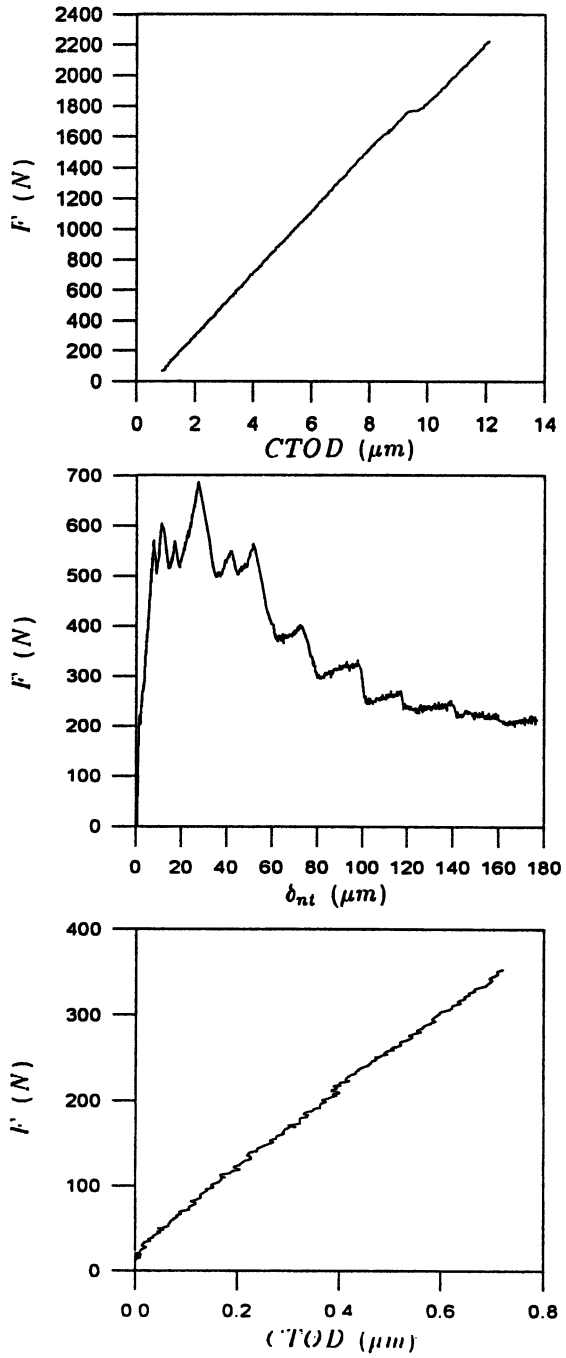

Figure 4.6: Load versus *CTOD* plots for (a) the *CENRBB* specimen (`CEN2b`), (b) the *CNT* specimen (`CNT3g`). Note that $\delta_{nt}\ |_{\Delta a \to 0} \equiv CTOD$; and (c) the *SCB* specimen (`SCB9i`).

4.6 Conclusions

- A new methodology using three different core based fracture specimens was developed. The amount of handling and machining can be minimized and therefore it is suited for field studies, especially on warm ice. For ice thicker than 660 mm, eleven specimens of large size can be manufactured from one ice core. In this manner all three principal O'ns may easily be investigated.

- K_I–expressions were determined for the Chevron Notched Tension *CNT* specimen, the Semi Circular Bend *SCB* specimen and the Chevron Edge Notch Round Bar in Bending *CENRBB* for a span/diameter ratio of 1.7.

- A statistical 95 % confidence interval for a difference in means showed a significantly *lower* apparent fracture toughness for the–with respect to *c*–axis orientation–hard fail O'ns VH and VV with respect to the HH O'n. In other words, cracking was found to be easier parallel than perpendicular (parallel to the *basal planes*) to the *c*–axis. Two different microstrucural effects can be possible explanations for this ambiguous behavior. The specimen size range was not sufficient to reduce the scatter and ensure notch sensitivity and polycrystallinity because of the large grain size. Further, the bubble layer present in the HH O'n tests may have shielded the crack from the bending (tensile) stresses and increased the *macroscopic* apparent fracture toughness. It is recognized that this investigation includes too few tests for the results to be statistically valid.

Paper **D**

Fracture resistance determination of freshwater ice using a chevron notched tension specimen

Lars M. Stehn
Department of Civil and Mining Engineering
Luleå University of Technology
S-951 87 Luleå, Sweden

Samuel J. DeFranco
Amoco Production Co.
P.O. Box 3385
Tulsa, OK 74102–3385, USA

John P. Dempsey
Department of Civil and Environmental Engineering
Clarkson University
Potsdam, N. Y. 13699–5710, USA

This chapter is a slightly extended version of a paper where the original text has been formatted. The paper has been submitted for publication in:

Stehn L.M., DeFranco S.J. and Dempsey J.P., 1993. Fracture resistance determination of freshwater ice using a chevron notched tension specimen, *International Journal of Fracture*

Chapter 5

Fracture resistance of freshwater ice

5.1 Abstract

Crack growth resistance (R-curve behavior) measurements on large grained S1 type freshwater ice were conducted in the Ice Mechanics Research Laboratory at Clarkson University. To overcome previous difficulties in obtaining stable cracking in freshwater ice, a new crack geometry was developed. The short rod Chevron Notched Tension (*CNT*) specimen was found to be extremely favorable in the sense of promoting stable, *stick–slip*, crack growth over a large portion of the uncracked ligament. A negative fracture resistance K_R–curve was evaluated for this ice at -16°C.

5.2 Introduction

During an ice/structure interaction several ice failure mechanisms are possible. This wide range of behaviors complicates the prediction of ice forces. Field observations show that there is extensive fracturing of ice caused by environmental forces or interactions with a stationary structure. In fact, ice around an offshore structure often presents a chaotic picture of multifariously fractured sheets and blocks, and when an icebreaker passes through an ice sheet there is a great deal of ice cracking. Here, fracture appears to be the

dominant failure mode in nature. Global splitting or fracture has been proposed as a possible load limiting process (Blanchet, 1990). However, the conditions under which fracture events occur have not been well defined and the influence of variations in fracture toughness, tensile strength and the geometrical size scale needs to be addressed. Practical application of fracture mechanics to the study of the failure of ice can incorporate the effects of fracturing into engineering ice load calculations and provide parameters for both the classification and the description of the mechanical behavior of ice.

Ice forms, of course, when water freezes. Only one type of ice is formed at atmospheric pressure and temperature, the so–called ordinary ice I_h which has a hexagonal close packed structure. The atomic structure of the ice builds on the geometry of the water molecule: each oxygen atom is bonded by two hydrogen atoms to four other oxygen atoms. The oxygen atoms become well bonded in layers of hexagonal symmetry but only one bond across to the next layer. This defines a basal plane (the preferred slip plane), parallel to the layer structure. The number of molecular bonds to be broken for deformation, e.g., creep or fracturing, parallel to the basal planes are less than in other directions. The axis of symmetry, perpendicular to the basal plane, is called the c–axis; this axis also coincides with the optical axis of each ice crystal, see e.g. Dempsey et al. (1992). Depending on the stress rate and the orientation of the basal plane with the stress direction ice displays a combination of responses: it shows elastic response but also immediately begins to creep; in addition, ice exhibit ductile deformation mechanisms but is also an extremely brittle material if the applied stress or stress rate is sufficiently high. For instance, it can fracture in a brittle manner, even very near the melt temperature.

There exist a growing number of measurements on the fracture toughness of ice reported in the literature. Recent reviews are found in Dempsey (1989) and Parsons (1990). Materials such as concrete, rock, ceramics and ice have an aggregate or grain size that is several orders of magnitude larger than typical metals. Because of this inhomogeneity, these materials do not strictly meet the assumptions of continuum mechanics in the sense that a suitable

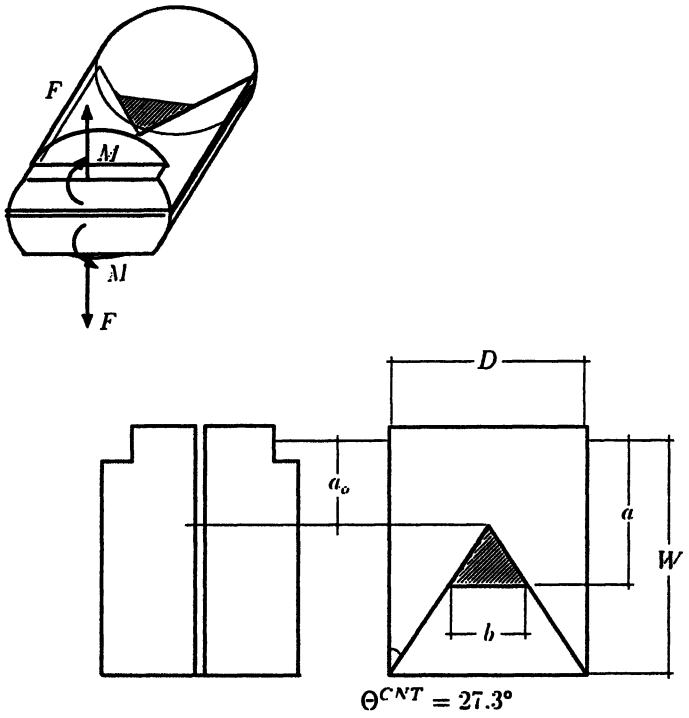

Figure 5.1: The Chevron Notched Tension (*CNT*) geometry.

large specimen size must be tested in order that polycrystallinity is mobilized. However, many previous fracture toughness investigations adopt the discipline of linear elastic fracture mechanics (*LEFM*) without ensuring the case of small–scale yielding (ASTM, 1985). The *LEFM* approach is valid provided that: the crack tip is sharp; the crack length is large in comparison with the grain size (polycrystallinity); and the specimen size (width, crack length and uncracked ligament) is sufficiently large in comparison with the crack tip process zone for the stress and deformation fields surrounding the crack to be grossly elastic.

To date, the emphasis has been on determining the fracture toughness corresponding to the initiation of a stationary macrocrack. For toughness tests without the consideration of crack growth stability, only the determination of K_{Ic} (the plane strain fracture toughness) is possible. Crack stability and crack growth in ice have received attention only recently (Dempsey et al., 1986; Bentley,

1988; Parsons et al., 1988 and 1989; DeFranco and Dempsey, 1990, 1991 and 1993; Stehn, 1993 and Stehn et al., 1993). The stable crack growth characteristic of sea ice and freshwater ice is desirable for a number of reasons: it permits the crack growth resistance, R, to be determined as a function of crack velocity, $\dot{a}$, and amount of crack growth, Δa; it is possible to study the crack initiation characteristics and it permits the design of controlled experiments. Even more important, in some cases during an ice/structure interaction a limited amount of slow crack growth may occur under increasing load before unstable crack formation and crack propagation and a dramatic drop in the ice load on the structure. This type of fracture cannot be quantified solely by K_{Ic}; instead, a different approach based on the energy absorption capability of the ice with crack growth is necessary (DeFranco and Dempsey, 1993). It is therefore apparent that a methodical investigation on the fracture resistance behavior of ice is needed. For this purpose, the short rod Chevron Notched Tension (*CNT*) geometry, see Figure 5.1, was developed. Fracture toughness tests were performed using the new crack geometry and freshwater S1 ice at -16°C. The test results were evaluated from the viewpoint of a characterization of the fracture resistance K_R–curve.

5.3 Crack growth stability

Many different concepts are invoked by the use of the word stable. The meaning of stable crack growth is different depending on the particular material: in metals stable crack extension occurs following local yielding, void growth and coalescence in the fracture process zone; for quasi brittle materials (concrete, rocks, ceramics) stable crack propagation is due to microcrack formation and crack branching. In addition, the above mentioned studies on crack growth stability in ice report incremental or so-called *stick–slip* cracking as opposed to continuous quasi static crack growth. *Stick–slip* cracking consists of crack initiation followed by an unstable crack propagation and a sudden crack arrest. To restart cracking, the applied load must be increased. The principles of crack arrest are discussed in Broek (1986). Of primary interest here is

that *stick–slip* behavior may be explained by: the microstructure (the large grain size); the fracture resistance (ice is rate sensitive that implies that the stress needed for crack growth may be lower than for crack initiation) and the experimental geometry (method of loading and total system compliance).

Crack propagation can only occur when the energy–release–rate (or crack driving force) G is just equal to crack resistance to fracture R; written as $G(A) = R(\Delta A)$ where $A = a \cdot b$ is the projected crack surface *area* (a is the crack length and b the crack front width). The fracture resistance is usually a function only of the amount of crack area extension ΔA and independent of the crack area width. If G is larger than R fracture instability occurs. For a crack to grow stably the equality of the energy–release–rate and the fracture resistance must be maintained and also the rate of change of crack driving force be less than the rate of change of fracture resistance. This implies that

$$G = R \qquad \text{and} \qquad \frac{\partial G}{\partial A} \leq \frac{\partial R}{\partial \Delta A} \tag{5.1}$$

for stable crack growth at the current crack area. For geometries with constant crack front width, the requirement for stable crack growth equation (5.1) is differentiated with respect to the crack length and amount of crack growth at the current crack length $a = a_o + \Delta a$. The $(\partial R/\partial \Delta A)$ term is the material property concerning the variation of toughness with crack growth and $(\partial G/\partial \Delta A)$ is the rate of change of the test geometry energy–release–rate. The next sections will focus on the characteristics and requirements of equation (5.1) for fracture resistance measurements on ice.

The shape of the R–curve depends on specimen thickness (that is, the crack front width) for metals. For thick plates under plane strain it is a horizontal line while thin plates under plane stress show a rising R–curve. This is commonly known as the thickness effect where the thickness of the specimen determines the state of stress at the crack tip. Maximum constraint is obtained under plane strain. Using a chevron notch geometry the crack front width is increased from zero to the full specimen width during crack extension. The crack front can be written as:

$$b = D\left(\frac{\alpha - \alpha_o}{1 - \alpha_o}\right) \tag{5.2}$$

where D is the specimen diameter, α is the relative crack length a/W, see Figure 5.1. Thus, as the crack extends in the region $a_o \leq a \leq 1$ in the chevron notch a transition of the state of stress at the crack tip exists. Furthermore, if the uncracked ligament is too short, for instance as an effect of accumulated crack growth, the closeness of the stress-free boundaries may significantly affect the stress field by reducing specimen constraints on the crack tip (Knott, 1973). However, for ice it is not yet determined whether cracking is accompanied by the same degree of lateral contraction as that observed in the fracture of metals. For rock, there is apparently no transition to a different deformation pattern in plane stress compared to plane strain (Ouchterlony, 1982). It has already been discussed that the stable crack growth observed on freshwater ice has always been incremental. This implies that the $\partial R/\partial \dot{a}$ ($\dot{a}$ is the crack velocity) behavior is negative. Further, the proposed negative R–curve in DeFranco and Dempsey (1990) clearly points out that stable incremental crack growth can only occur in geometries in which $\partial G/\partial a$ is sufficiently negative to satisfy the crack growth stability expressions given in equation (5.1). To obtain stable crack growth in ice DeFranco and Dempsey (1993) found it necessary to design a test geometry with a very negative *geometric stability factor* or *GSF* (Mai and Atkins, 1980). The *GSF* may be obtained for any fracture geometry by manipulation of equation (5.1) and the relationship between the energy-release–rate and the compliance of the geometry. The reader is referred to DeFranco and Dempsey (1993) for a more comprehensive description of energetic stability in (ice) fracture testing.

5.4 The short rod Chevron Notched Tension specimen (CNT)

The standard Short Rod Chevron Notched specimen *SRCN* was first proposed by Barker (1977) and (1978). The stability of the

initial crack growth in the *SRCN* specimen has been observed in many materials (metals, ceramics and rocks).

An important feature of the new *CNT* geometry is the external reduction of excess released strain energy achieved through the Reverse Direct Tension Device (see next section). By not using a ball–joint system, a negative (closing) moment is generated that oppose the opening load, in the sense of reducing the K_I–factor, and thus increases the specimen stability.

Figure 5.1 shows the schematic of the *CNT* geometry. The *beam–like* configuration of the *CNT* specimen is conveniently modeled using a one–dimensional beam on elastic (Winkler) foundation model in Kanninen (1973). The Winkler foundation is used to model the uncracked area of the specimen which allows the determination of a theoretical compliance function valid over the range $0 \leq \alpha \leq 1$. The geometry and boundary conditions used in this analysis is shown in Figure 5.2. Due to the special loading arrangement, the load can be decomposed into an opening load F and a closing end moment *M(F)*. For a linear elastic homogeneous material, superposition can be used to treat the combined loading as the sum of two separate load cases.

The governing differential equation for the beam deflection $w(x)$ is

$$\frac{d^4w}{dx^4} + 4\lambda^4(x)H(x)w = 0 \tag{5.3}$$

where $H(x)$ is the Heaviside step function. For a chevron notch b increases with increasing x, or alternative $(\alpha - \alpha_o)$ as shown in equation (5.2). Using the definitions in Kanninen (1973) of λ and k, the foundation modulus, given that the initial crack length $\alpha_o = 0.332$, $\lambda(x)$ is derived as:

$$\lambda = \frac{1.922}{R}\left(\frac{x}{W}\right)^{1/4} \tag{5.4}$$

where R is the core radius and W the specimen length.

Unfortunately, equation (5.3) has no unique solution and it is therefore necessary to apply some numerical technique to solve it. In this study, a constant value of $\lambda(x)$ was taken as a approximation

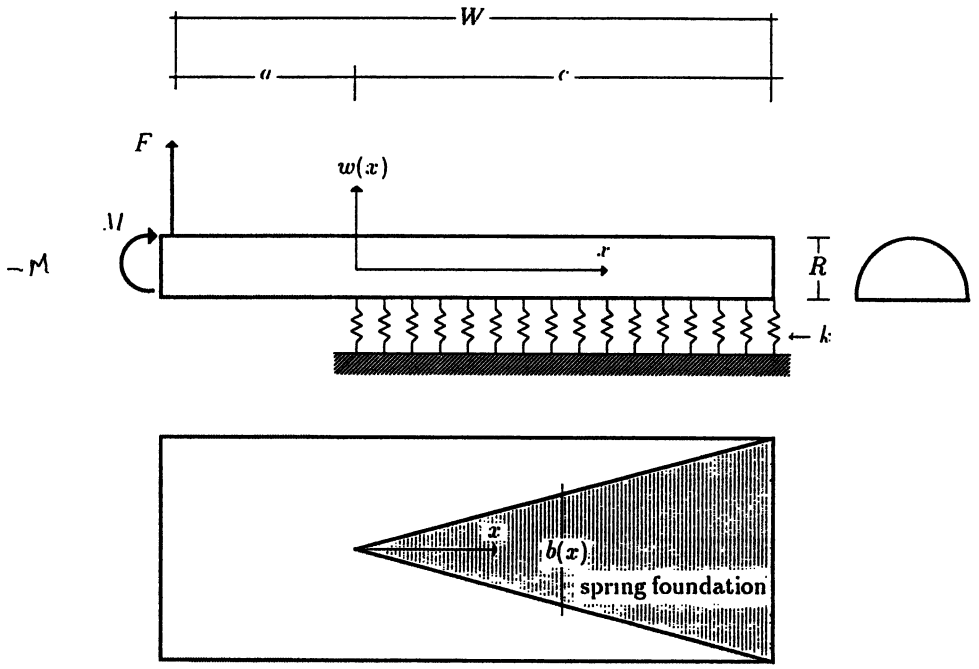

Figure 5.2: Beam on elastic foundation model of *CNT* specimen.

to estimate the stress–intensity–factor and the compliance for the *CNT* specimen. A closed form solution of equation (5.3) can then be obtained. The $(\alpha - \alpha_o)$ dependence is incorporated in a more arbitrary way, described below, by computing a function Y_b based on known specimen compliance properties.

Applying the boundary conditions in Figure 5.2, the specimen compliance, $C_{CNT} = \phi/(E'R)$, is derived. ϕ is a non–dimensional compliance function and E' the effective elastic modulus. Then by using the *LEFM* relationships between the energy-release-rate and the compliance of the specimen, $G = F^2(dC/da)/2b$, and the equivalence between the stress–intensity–factor and the energy–release–rate, $K^2 = GE'$, the net stress–intensity–factor is given by the sum of contributions due to the opening load and the closing moment load as:

$$K_I^{CNT} = K_F^{CNT} - K_M^{CNT} \tag{5.5}$$

The K_I–expression for the *CNT* is ultimately given by:

$$K_I^{CNT} = \frac{F}{R^{3/2}} \left(\frac{0.908}{Y_b \bar{\lambda} (\alpha - \alpha_o)^{1/2}} [Y_F(\alpha, w/R) - Y_M(\alpha, w/R)] \right) \tag{5.6}$$

The two shape functions $Y_F(\alpha, w/R)$ and $Y_M(\alpha, w/R)$ are given as:

$$Y_F = \alpha(w/R) C_3 C_1 + C_2(\eta=-1) \tag{5.7}$$

$$Y_M = \left(\frac{\alpha^2 (w/R)^2 C_3^2 + 2\alpha(w/R) C_3 C_2(\eta=1) + C_1}{2\alpha(w/R) C_3 + 2C_2(\eta=1)} \right) C_1 \tag{5.8}$$

in which

$$C_1 = \frac{\sinh^2 \lambda c + \sin^2 \lambda c}{\sinh^2 \lambda c - \sin^2 \lambda c} \tag{5.9a}$$

$$C_2(\eta) = \frac{\sinh \lambda c \cosh \lambda c + \eta \sin \lambda c \cos \lambda c}{\sinh^2 \lambda c - \sin^2 \lambda c} \tag{5.9b}$$

$$C_3 = 1.922 \bar{\lambda} \tag{5.9c}$$

In equation (5.9a) and equation (5.9b) $\lambda c = C_3(1 - \alpha)(w/R)$ and $\bar{\lambda}$ is the estimated constant value of $(x/W)^{1/4}$.

It is easily seen that if the Y_M term is excluded an ordinary (*SRCN*) test is modeled. So a convenient way to estimate $\bar{\lambda}$ is to

normalize $Y_F(\alpha)$ with respect to a reference function $Y_{SRCN}(\alpha)$ and make certain that the ratio when these two functions are minimum[1] is unity for the same relative crack lengths. The dimensionless stress–intensity–factor determined by Matsuki et al. (1991) was used as the reference function. A multiple regression analysis was used assuring the above while at the same time minimizing the sum of squares of the residuals. The best regression estimate of $\bar{\lambda}$ was found to be,

$$\bar{\lambda} = 0.916 \tag{5.10}$$

with an estimated standard deviation of 0.032. Furthermore, a constant $\bar{\lambda}$ value is associated with a straight notch, i.e., a constant b, and therefore must the derivatives of the compliancies C_{CNT} and C_{SRCN} must be related as (Ouchterlony, 1984):

$$\frac{dC_{SRCN}}{da} < \frac{dC_{CNT}}{da} \quad \text{for} \quad \alpha_o \leq \alpha < 1 \tag{5.11a}$$

$$\frac{dC_{SRCN}}{da} = \frac{dC_{CNT}}{da} \quad \text{for} \quad \alpha = 1 \tag{5.11b}$$

To fulfill the requirements in equation (5.11), Y_b was estimated from the normalized shape function with the following polynomial approximate

$$Y_b = 10.14(1 - 6.46\alpha + 17.41\alpha^2 - 20.96\alpha^3 + 9.50\alpha^4) \tag{5.12}$$

as the best fit.

Figure 5.3 shows the non-dimensional stress–intensity–factors as a function of crack length for the *CNT* geometry and, dashed line, K_F^{CNT}, for an aspect ratio $W/R = 2.9$. The figure clearly reveals the dependence in the *CNT* geometry on α. For short crack lengths, $\alpha \leq 0.4$, the curve decreases steeply for increasing crack lengths and stable crack propagation should be expected

[1]For a *SRCN* specimen the fracture toughness is computed for a minima in the shape function Y occurring at a critical crack length α_c. For a material with flat R–curve α_c is a unique value. It is worth to notice that $K \sim Y \sim (dC/da)^{1/2}$.

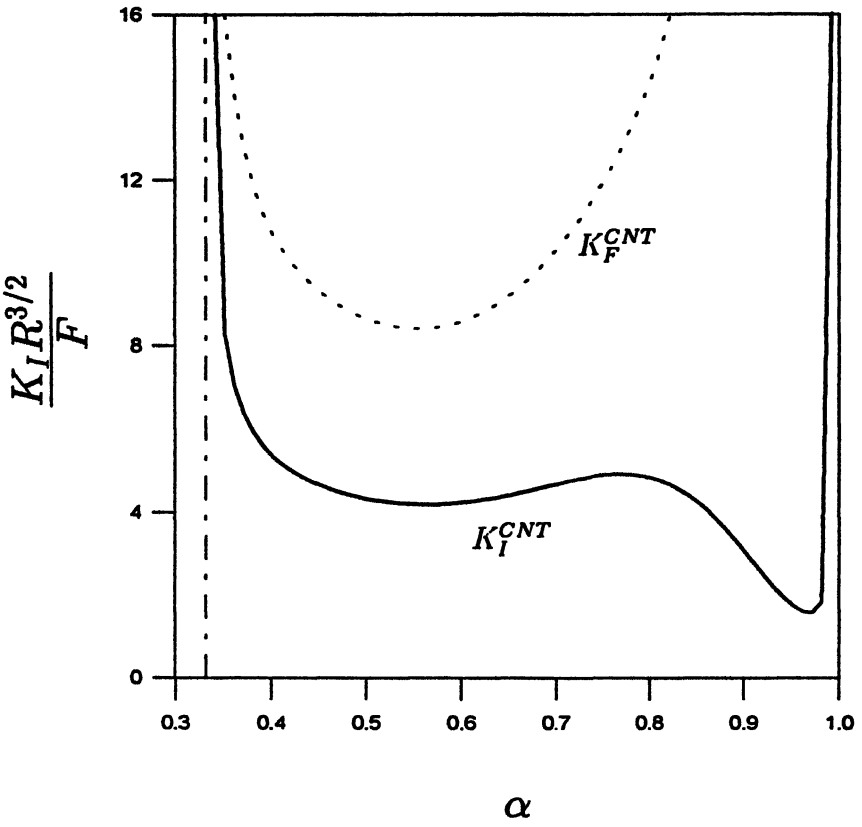

Figure 5.3: Non-dimensional stress–intensity–factors as a function of crack length for the *CNT* geometry and, dashed line, K_F^{CNT} for an aspect ratio $W/R = 2.9$.

through the very negative $\partial G/\partial a$. In the intermediate regime of crack lengths, $0.45 \leq \alpha \leq 0.75$, the curve gradually changes slope to a slight increase and a propagating crack is expected to arrest. For longer crack lengths, $\alpha \geq 0.8$, a decreasing portion of the curve is entered which indicates a second regime of possible stable crack growth. For very long crack lengths, the effect of the closing moment is maximum and for a material with a flat R– curve, equation (5.6) predicts a high value of F necessary for continued cracking. Since the specimen at this point is very compliant, a large force is difficult to obtain quickly in a controlled test situation, and a propagating crack will arrest.

This interpretation of the K_I analysis is possible if the theoretical range of validity, i.e., the interval $0 \leq \alpha \leq 1$, is true. However, as was found out in the experiments, see below, questions about the accuracy of the model for long crack lengths can be raised. Nevertheless, the *CNT* geometry is greatly improved, in the sense of promoting stable crack growth, compared with the ordinary *SRCN* specimen, represented by the dashed curve in Figure 5.3. For the latter, stable crack growth is only possible when $\alpha \leq 0.55$, where after the positive $\partial G/\partial a$ encountered contradicts stable propagation.

Proceeding just as above, ϕ was also obtained. This makes it possible to determine the normalized *GSF* for the *CNT* for the case of displacement control as (DeFranco and Dempsey, 1993):

$$GSF = \frac{W}{G}\frac{\partial G}{\partial a} = \frac{\partial^2 \phi/\partial \alpha^2}{\partial \phi/\partial \alpha} - 2\frac{\partial \phi/\partial \alpha}{\phi} \tag{5.13}$$

without consideration of the compliance of the loading device. The normalized *GSF*s for the *CNT*, the Double Torsion (*DT*) geometry (Parsons et al., 1989) and the Reverse Tapered Crack Line Wedge Loaded (*RTCLWL*) geometry (DeFranco and Dempsey, 1993) are shown in Figure 5.4. All geometries show negative *GSF*s for all crack lengths. However the *RTCLWL* (for long crack lengths) and the *CNT* (both for short and long crack lengths) are extremely favorable in the sense of promoting crack growth stability even for *stick–slip* cracking materials. Similar theoretical predictions of the fracturing behavior of the *CNT* can be made from Figure 5.4.

5.5 The S1 ice microstructure

Freshwater ice cores were collected from a pond formed in an abandoned limestone quarry, near Clarkson University, Potsdam, NY, during February, 1992. The average ice thickness was 450 mm. An interesting feature of this ice was found in each core: at approximately 200 mm from the ice surface a 50 mm thick bubble layer existed. The small bubbles were evenly distributed and made the ice opaque. At this location the ice was evidently saturated with air bubbles and air channels (Fransson and Stehn, 1993) but what

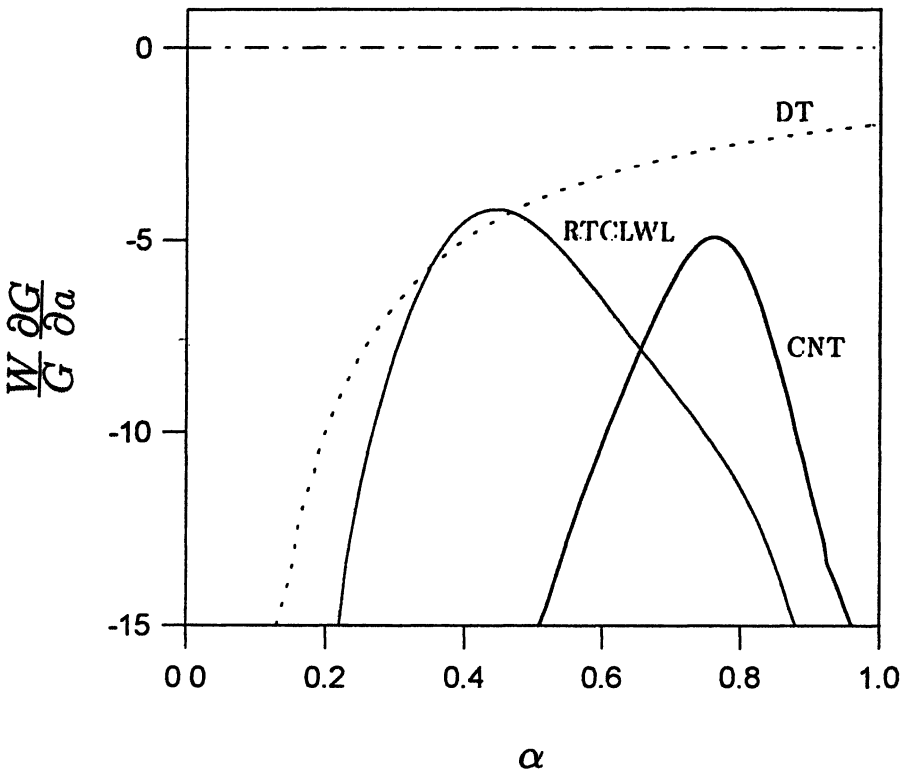

Figure 5.4: Normalized geometry stability factors (*GSF*)s for the *DT*, *RTCLWL* and *CNT* fracture geometries.

caused this is unclear. Nevertheless, this layer did not cause any obvious influence on the ice properties. The very warm ice pieces (air temperature ±0 °C) were wrapped in plastic, transported to a cold room at Clarkson and stored at -15°C to -20°C for two months.

The non-turbulent waters of the pond had produced macro crystalline S1 ice, as defined by Michel and Ramseier (1971), composed of irregularly shaped columnar crystals with vertical or near-vertical *c*–axis orientation. The grain size showed an increase with depth, from 6.8±0.7 mm at the top (below the approximately 70 mm thick fine grained snow–ice layer) to 10.8±1.6 mm near the bottom. The columnar macrocrystalline feature of the natural S1 ice is presented in Figure 3.3 which shows both (a) vertical and (b,c) horizontal thin sections.

The *c*–axis orientation of three different cores was measured at three different depths from horizontal thin sections using a Rigsby universal stage (Langway, 1958). A stereographic projection at each level of these *c*–axes are shown in Figure 3.4. The first level was approximately 50–70 mm from the top (99 grains measured), the second 120–160 mm from the top (95 grains) and the third was located 180 mm from the top (35 grains). In the first level 73 % of the grains were found to be vertical or near-vertical (to within 20 degrees inclination of the *c*–axis from vertical), in the second level 87 % (to within less than 15 degrees) and in the third level 97 %. Thus, it is evident that the *c*–axes of most grains was randomly and vertically or near–vertically oriented which is, by definition, S1 type ice.

The density was measured at approximately the same levels as the *c*–axis measurements by recording the mass of a known volume. The mass was measured on a digital scale with an accuracy of 0.1 g and volume was measured using digital calipers accurate to 0.01 mm. The average density was 906 ±10 kgm^{-3} at -16°C

5.6 Experimental setup

The ice pieces were removed from the storage freezers and placed in the specimen preparation cold room at -16°C (which was also the specimen preparation temperature). The length and chevron

Test #	D/W (mm)	a_o/W	$(W, a_o)/d_{av}$
CNT1	198/287	0.32	32,10
CNT2	198/285	0.33	32,11
CNT4	198/285	0.33	25,8
CNT5	198/285	0.33	30,10
CNT6	198/284	0.34	32,11
CNT7	198/286	0.30	30,9

Table 5.1: *CNT* test data

angle for the *CNT* was formed by a band saw. The proper angle, 27.3°, was ensured by using a simple notch cutting fixture similar to that described in ISRM (1988). Each finished specimen had a diameter D= 198 mm and a length of approximately $W = 1.44D$ (Table 5.1). The crack orientation and propagation direction were kept perpendicular to the plane of the ice sheet, i.e., a vertical crack propagating vertically downwards in the direction of crystal growth. The special groove, to fit the endcaps of the test device, in the front face of the specimen was milled by a 20 mm vertical endmill.

The *CNT* experiments were performed using an apparatus based on the reverse direct stress testing system of Cole and Gould (1990). The original concept of Cole and Gould was modified for testing ice plates instead of ice cores; this development and implementation of the modified reverse direct tension device (*RDTD*) was conducted by the third author (JPD) and coworkers at Clarkson University over the past three years. The experimental setup is shown in Figure 5.5.

The *RDTD* has a distinct advantage over typical ball–joint systems used by others in that the direction of applied stress can be cycled with no backlash (Cole and Gould, 1990). Additionally, inevitable specimen misalignment is accounted for in this setup. These advantages are accomplished through a three part apparatus (Figure 5.5): i) the collet assembly (arrow **A**); ii) the circumferential clamp (arrow **B**); and iii) the endcap (arrow **C**).

Two collet assemblies are each fixed to the testing frame (ram

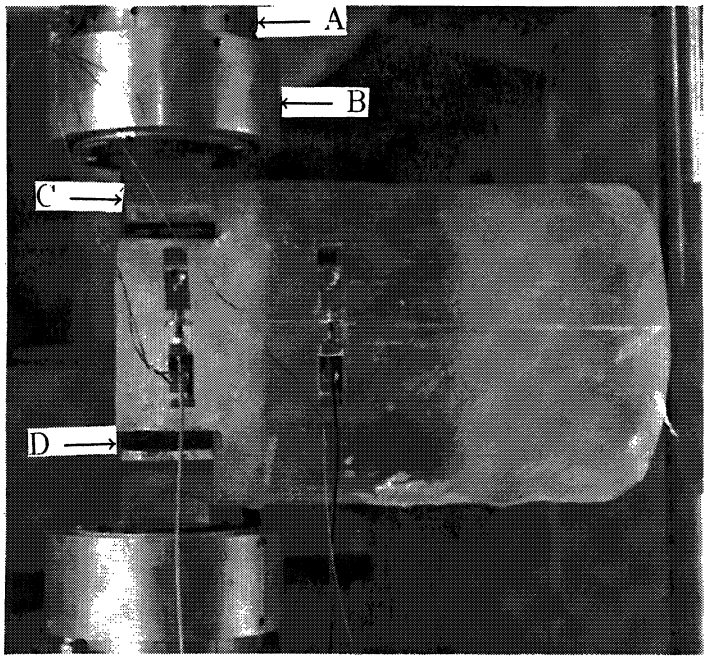

Figure 5.5: The experimental setup. A *CNT* specimen is ready for testing using the Reverse Direct Tension Device *RDTD*.

and load cell) and have individual plates which are compressed against the bearing race by circumferential hydraulic clamps. The clamps each have four inner O rings and four outer *PVC* retainer rings (rectangular cross section) which compress against the collets when pressure is applied. A spherical bearing in the endcap corrects for misalignment of the specimen once the endcap/specimens are installed. System pressure is applied by an Enerpac hand–operated hydraulic pump. The reader is referred to Cole and Gould (1990) for specific details of the *RDTD*.

In this study, the endcaps were affixed to the ice plates by the following method: the phenolic plates (arrow **D** in Figure 5.5) were initially soaked in room temperature water (note that the phenolic is permanently bonded to the aluminum endcaps). The endcaps were then placed in the cold room for approximately 5 to 15 minutes in order to cool. Very cold fresh water ($\approx$ 0°C) was jetted by an eyedropper onto the phenolic of one endcap which was immediately attached to a *CNT* specimen. A very good bond formed after a few second (interestingly, the bond could only be broken by melting the cracked specimen after each test). The attached endcap was then placed in the lower collet (already mounted on an Instron 8500 testing frame). Attaching the upper endcap was slightly more difficult. The upper endcap was placed in the upper collet and the crosshead was lowered so that the phenolic and *CNT* specimen were very close. Contact was made using the manual positioning of the ram; no loading was applied to the specimen during this phase. After contact was made, cold water was jetted around the phenolic in order to form the upper bind. No specimen broke at this bond.

A sharp crack was created approximately 20 minutes prior to the test by scribing the notch with a fine tooth saw–blade. The crack tip opening displacements *CTOD*s and crack opening displacements *COD*s were measured during the fracture experiments using a procedure similar to that described in Wei et al. (1991), in which the error estimates using this technique can be found. A Kaman KD-2810-1U non-contacting displacement gauge (measuring range $25 \pm 0.025 \mu$m) was frozen onto the specimen surface ahead of the notch and a Kaman KD-2310-1U measuring the *COD*s (measuring range $1000 \pm 0.1 \mu m$) was positioned so the line of measurement

of the Kaman gauge coincided with the line of loading for the end caps (at approximately 30 mm from the front face). Thus, the *COD* coincides with the load line displacement δ_{LLD}.

The load and transducers readings were processed by a Keithly Series 500 analog-to-digital converter connected to a Gateway 200 model 486/33 microcomputer. Data was received at the rate of 600 Hz for test times ranging from 20 to 60 seconds. All tests were performed on an Instron 8500 digital testing system under stroke control. The stroke rate for each test was 0.01 mm s^{-1} and the test temperature -16°C.

5.7 Test results

Figure 5.6(a) to Figure 5.11(a) shows the F versus δ_{nt} plot for specimens CNT1 to CNT7. In this case $\delta_{nt}\,|_{\Delta a \to 0} \equiv CTOD$ is defined as the *near* crack tip opening displacement since the gauges were attached to the specimen surface at a distance of 100 mm from the initial crack tip. It is thus expected that the measured δ_{nt} values are larger than true *CTOD*s due to the incorporated effect of elastic deformation. The changes of slope are associated with crack jumps where the crack extension occurs under decreasing load. This definite change in slope is also evident in the F–time and δ_{nt}–time spaces (Figure 5.6(b) to Figure 5.11(b)). The non–zero (positive) intercept on the F–axis of each linear portion in the F–δ_{nt} plots indicates the presence of crack closure forces.

This specimen promotes stable crack extension over uncharacteristically large portions of the initial uncracked ligament; in one case (CNT4), as many as 15 crack jump events were visible and an unstable fracture never occurred. This is contrary to previous attempts (DeFranco and Dempsey, 1990) where only a few crack jumps was observed and then for very long crack lengths. The crack extension was in all cases essentially planar. Only the first third (20 or 30 seconds) of the experiments are shown in the Figures. For very long crack lengths ($\alpha \geq 0.85$) slow, almost continuous, cracking with short crack jumps was observed. At this point, a specimen is very compliant so the necessary load to completely split the specimen could only be reached by increasing the stroke

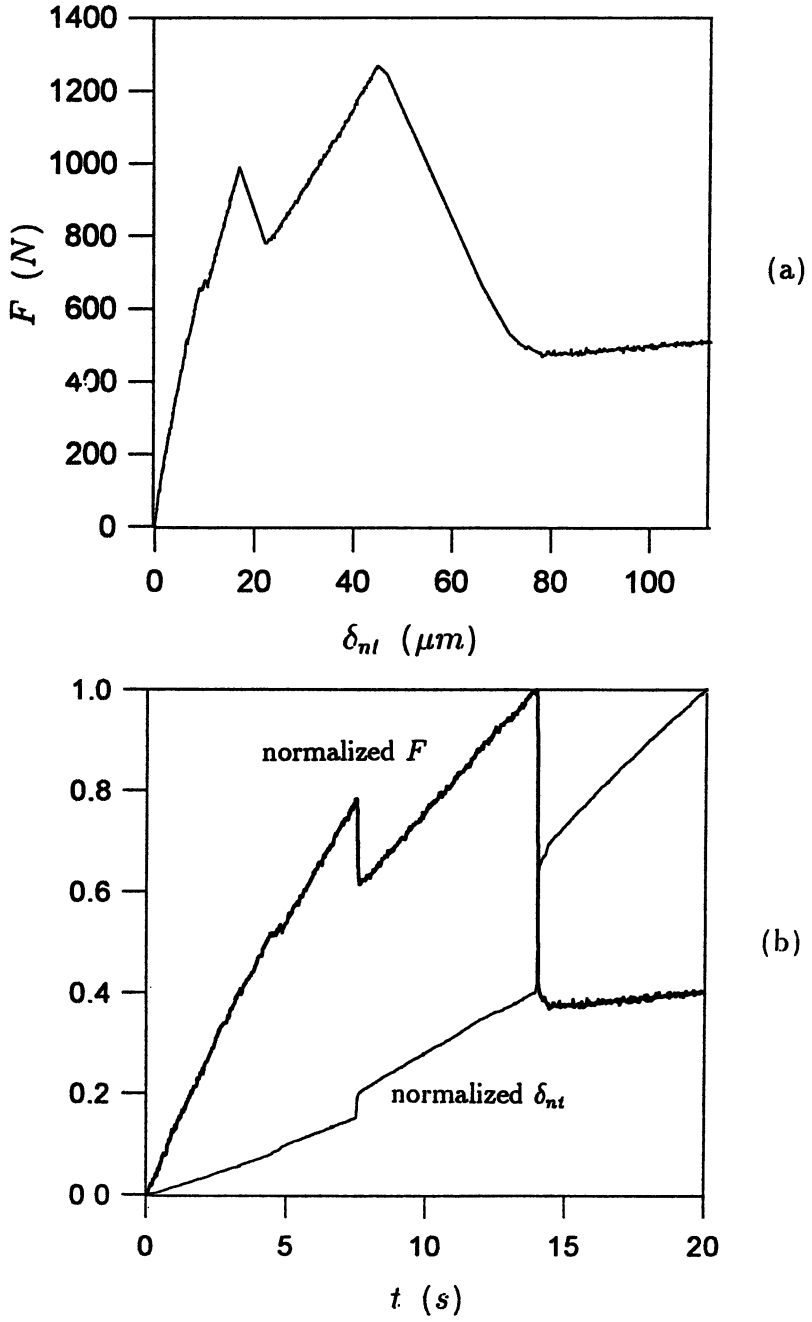

Figure 5.6: (a) Load versus δ_{nt} plot (CNT1). Note that $\delta_{nt}\,|_{\Delta a \to 0} \equiv CTOD$; and (b) Normalized load ($F/F_{\max}$) and normalized *near* crack tip opening displacement ($\delta_{nt}/\delta_{nt\max}$) versus (test) time.

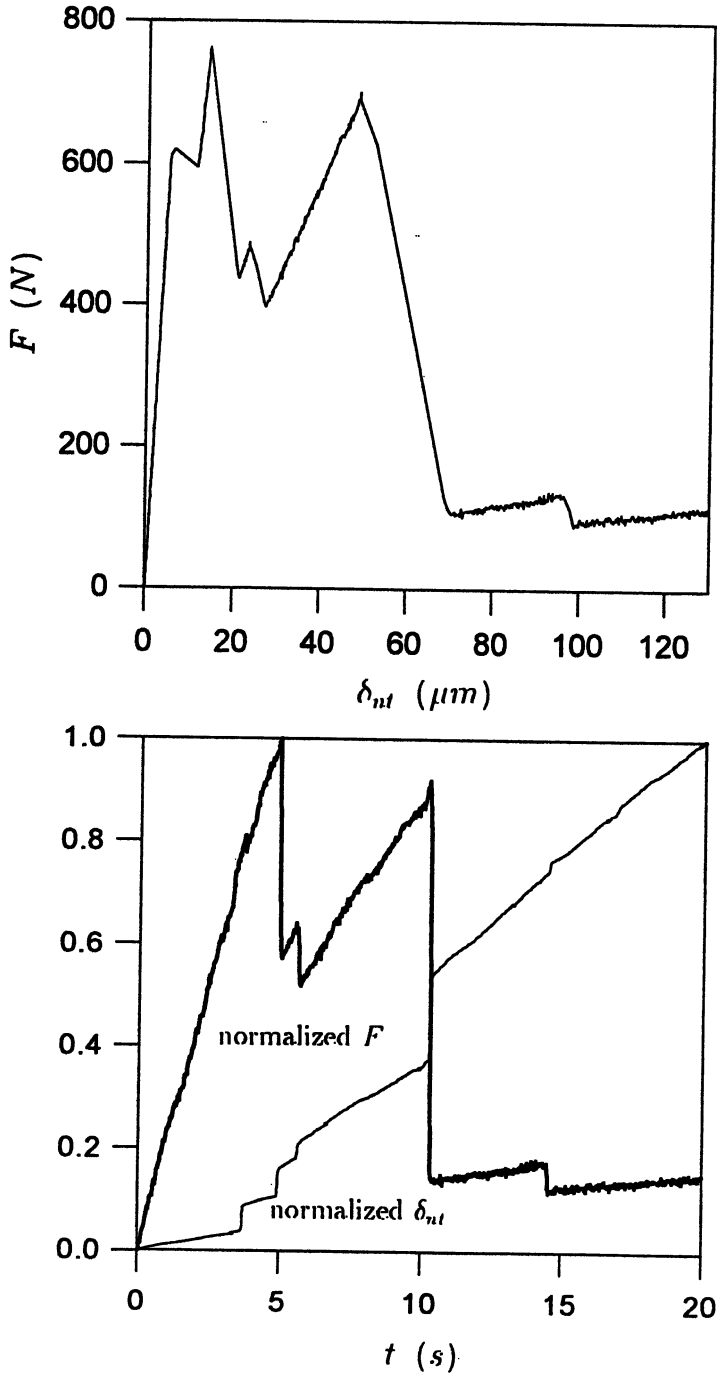

Figure 5.7: (a) Load versus δ_{nt} plot (CNT2). Note that $\delta_{nt}\,|_{\Delta a \to 0} \equiv CTOD$; and (b) Normalized load ($F/F_{\max}$) and normalized *near* crack tip opening displacement ($\delta_{nt}/\delta_{nt\max}$) versus (test) time.

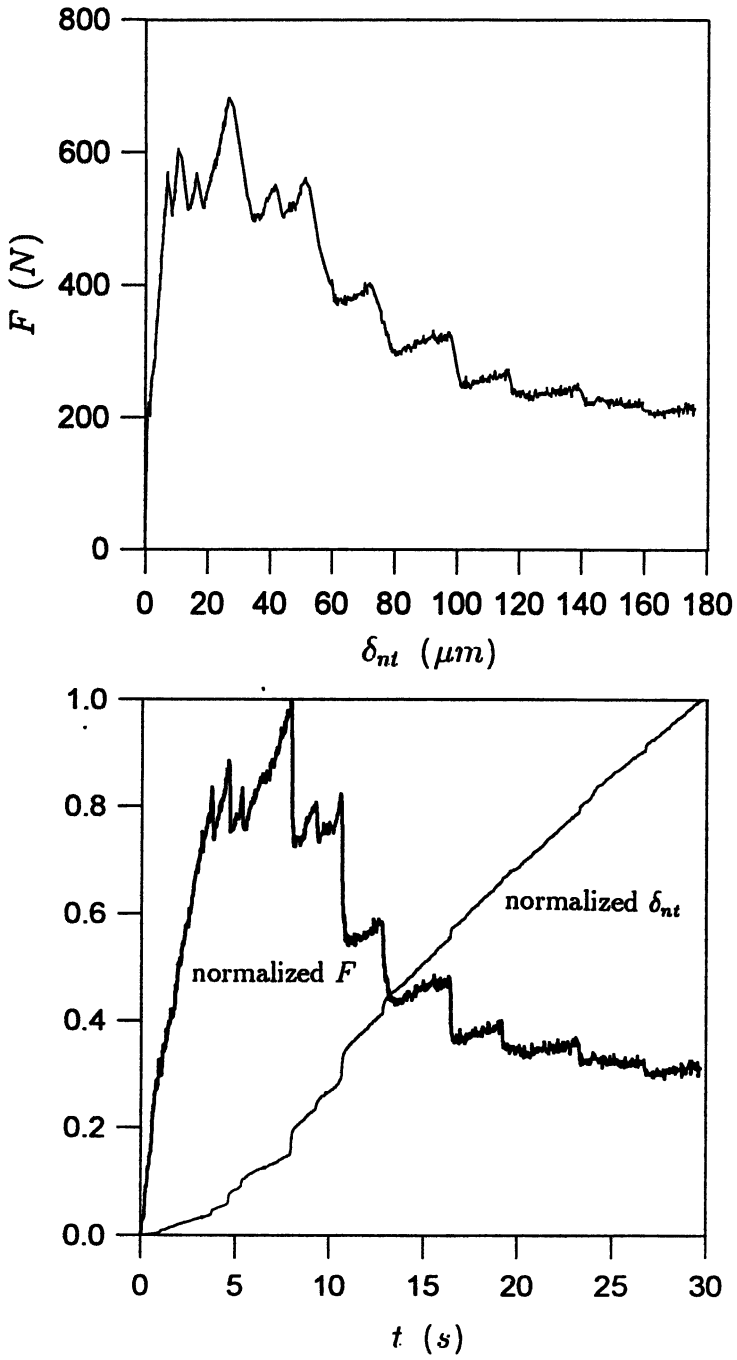

Figure 5.8: (a) Load versus δ_{nt} plot (CNT4). Note that $\delta_{nt}\,|_{\Delta a \to 0} \equiv CTOD$; and (b) Normalized load ($F/F_{\max}$) and normalized *near* crack tip opening displacement ($\delta_{nt}/\delta_{nt\max}$) versus (test) time.

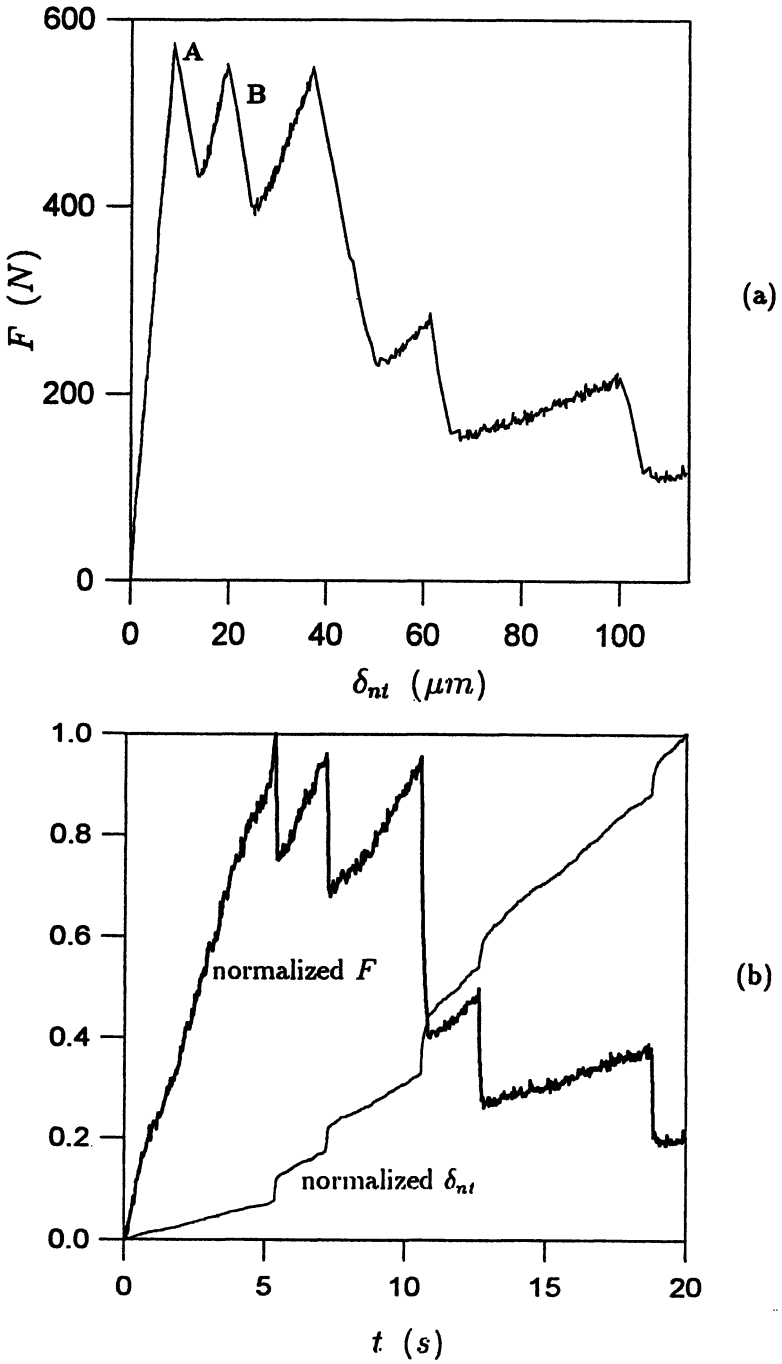

Figure 5.9: (a) Load versus δ_{nt} plot (CNT5). Note that $\delta_{nt}\,|_{\Delta a \to 0} \equiv CTOD$; and (b) Normalized load ($F/F_{\max}$) and normalized *near* crack tip opening displacement ($\delta_{nt}/\delta_{nt\max}$) versus (test) time.

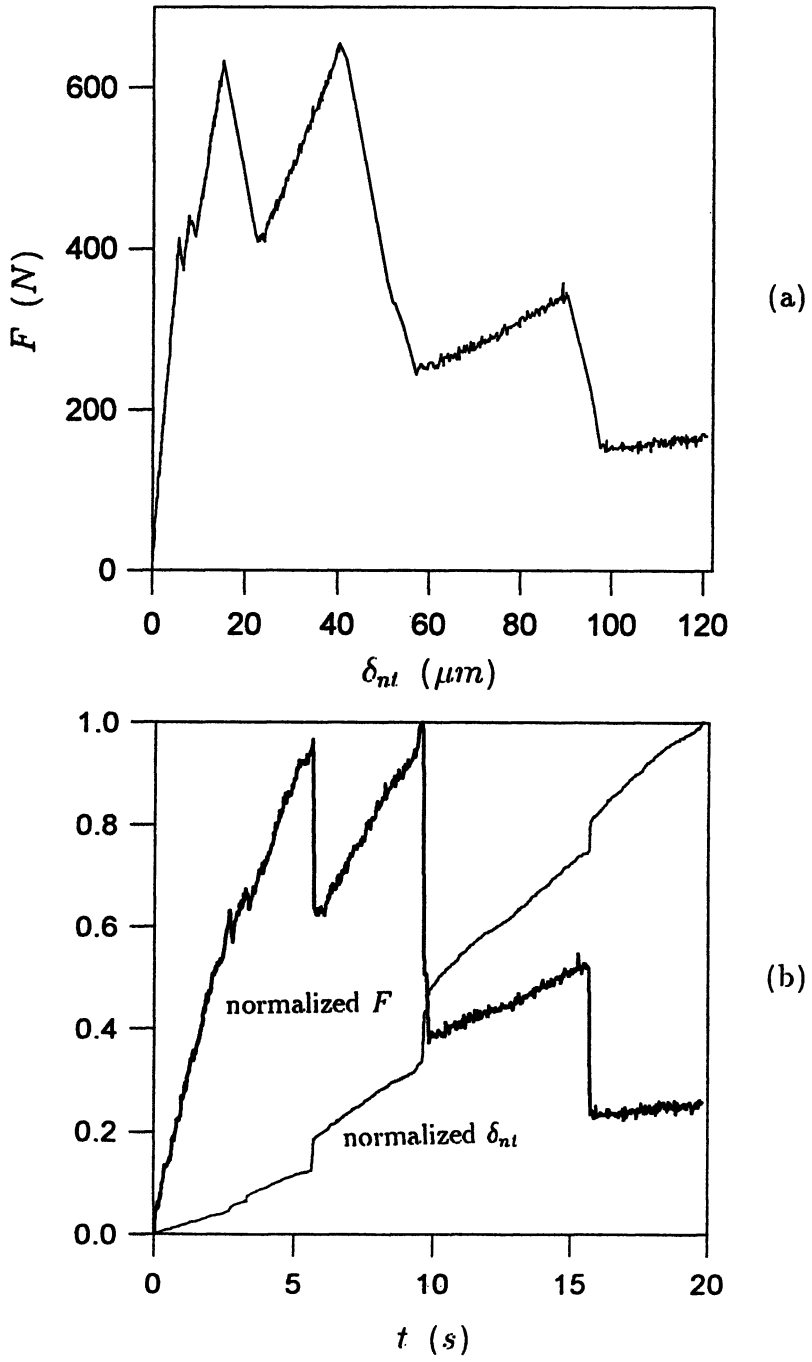

Figure 5.10: (a) Load versus δ_{nt} plot (CNT6). Note that $\delta_{nt}\,|_{\Delta a \to 0} \equiv CTOD$; and (b) Normalized load ($F/F_{\max}$) and normalized *near* crack tip opening displacement ($\delta_{nt}/\delta_{nt\max}$) versus (test) time.

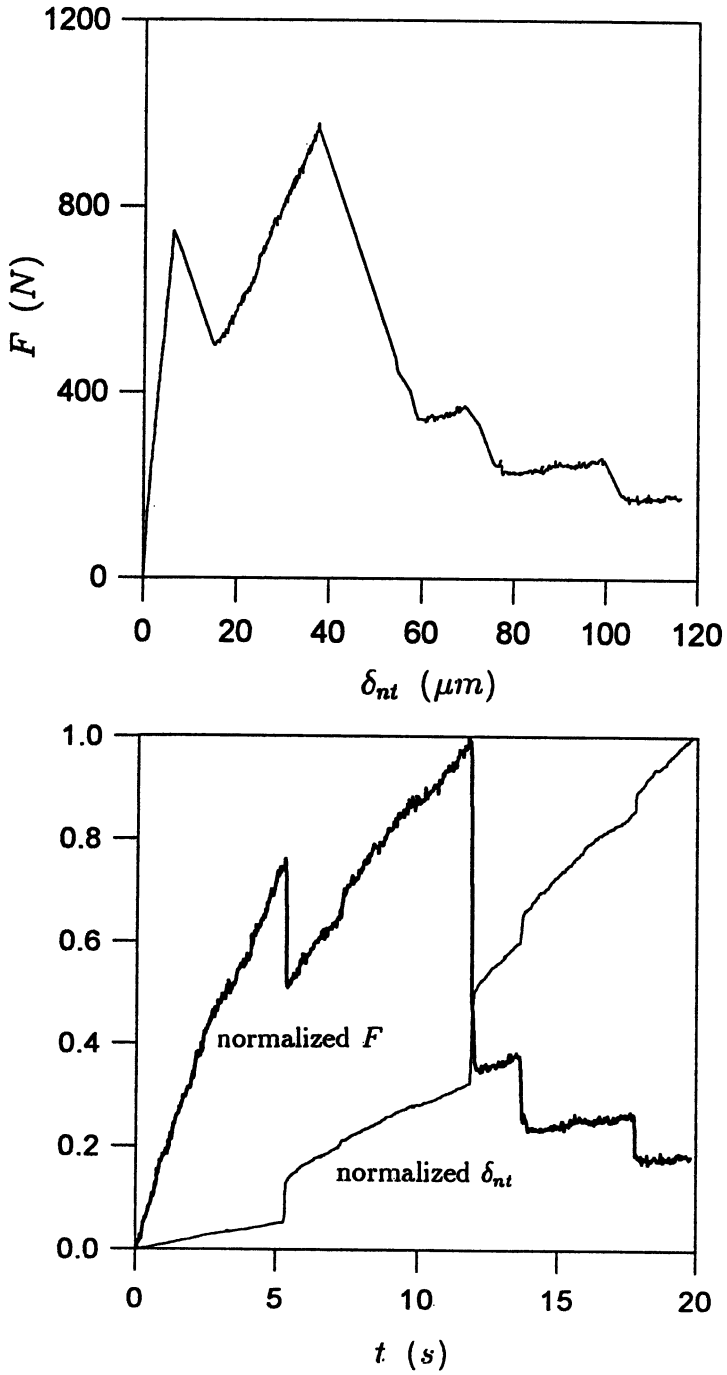

Figure 5.11: (a) Load versus δ_{nt} plot (CNT7). Note that $\delta_{nt}\,|_{\Delta a \to 0} \equiv CTOD$; and (b) Normalized load ($F/F_{\max}$) and normalized *near* crack tip opening displacement ($\delta_{nt}/\delta_{nt\max}$) versus (test) time.

rate to 0.1 mm s^{-1} and then only after approximately 40 seconds.

By taking the first linear slope, C_o, of the load–load line displacement curves, the effective elastic modulus was obtained (Table 5.2); the values were computed as $E' = \phi_o/(C_o R)$. The approximate initial stress–intensity rate $\dot{K}$ varied between 20 to 90 kPa $\sqrt{\text{m}}\,\text{s}^{-1}$.

Visual crack length measurements on freshwater ice can relatively easily be performed because of its transparency. In general, visual methods have two main disadvantages: the limited accuracy and that only the traction free crack length can be measured. In this study, the traction free crack length was used, hence, the process zone attached to the crack tip is considered to be of negligible size. In support of this are the linear F–δ_{nt} plots and the apparent affinity of the rotation axis and the crack tip for freshwater ice at these loading rates (Weber and Nixon, 1991).

The S1 freshwater ice tested was very clear, with the exception of the above mentioned 50 mm thick bubble layer. Before each test, the specimens were polished by gently melting the surface to obtain transparency. The crack growth was slow enough to be visually observed; each crack jumps could clearly bee seen during the test and the length was marked on the specimen surface. The accuracy of these marks are probably ±1mm. The fracture surfaces were then visually examined. The surface was fairly smooth with lines, perpendicular to the crack propagation direction, extending over the whole width of the notch. These lines represent crack arrest/initiation lines and by correlating the marks on the specimen surface with the matching crack arrest/initiation line, the crack length could be obtained. By the *CTOD* measurements, each crack jump identified on the fracture surface could then be correlated to the current load. On one split specimen (CNT4), a fracture replica was made by dropping a solution (4% Formar in ethylene dicloride) on the fracture surface. Formvar solutions have previously been used (Wei and Dempsey, 1991) to duplicate the surfaces of ice. Fractographic examinations were then conducted on the replica were the crack arrest/initiation lines could be identified by a distinct line from where river pattern extended. Figure 5.12 shows a section of the replica photographed at 13X with an Olympus zoom

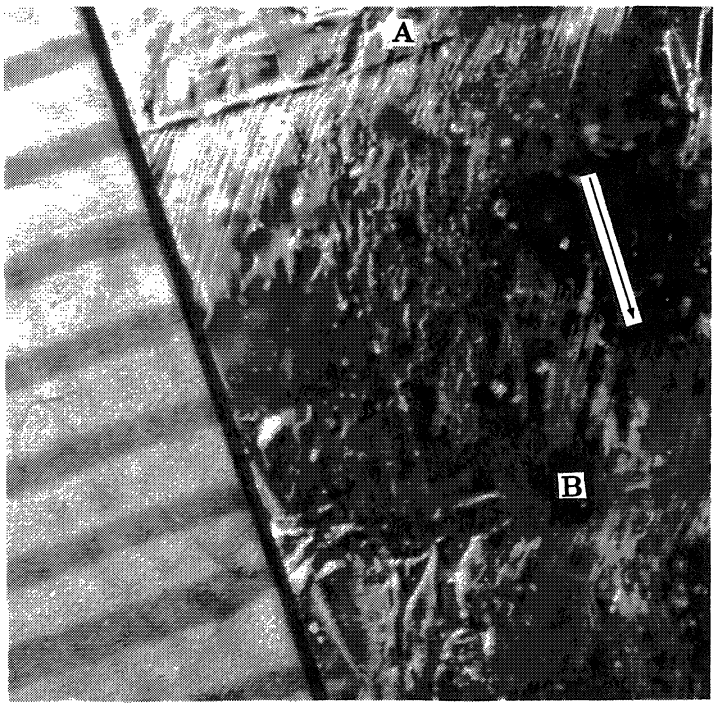

Figure 5.12: The characteristic of *stick–slip* cracking of *CNT* fracture photographed using an optical microscope on a replica of a fracture surface (**CNT4**); crack arrest and initiation lines (**A** and **B**) are identified. A crack jump of roughly 5 mm (scale in mm) is visible. The arrow indicate the crack propagation direction.

stereo SZ-PT microscope. River patterns form because of the multiple cleavage steps that is created when an extending crack passes a grain boundary or when an arrested crack is re–initiated because the crack may have to propagate in a slightly different orientation, Broek (1986). The crack jump lengths were then measured using the optical microscope and were found to coincide almost exactly with the visually measured lengths. At this point it is important to point out that scatter and uncertainties in the results are expected due to the large grain size of the S1 ice. This is indicated by the small ratio of specimen size to average grain size (Table 5.1) obtained in these tests. It can be speculated that the scatter typi-

cally observed in S1 ice testing is due both to specimen size effects and crack tip location vs. the contiguous microstructure prior to crack initiation. When the fracture specimen is too small with respect to *LEFM* constraints and relative to the grain size, it is *notch insensitive* and a representative fracture event is not measured (Dempsey, 1989; Dempsey et al., 1992; and Parsons et al., 1993). When there are too few grains in the notch cross–section, the full confining effect imposed by neighboring grains (polycrystallinity) is not mobilized. Additionally, if the initial notch or arrested crack ends within a grain, the local orientation of that grain may in large part determine the energy needed to initiate and propagate a crack.

5.8 Fracture resistance of S1 ice

The experimental results are summarized in Table 5.2 where F_I is the crack initiation load used in equation (5.6) to calculate the initiation fracture resistance K_{RI} and F_A is the crack arrest load that corresponds to K_{RA}. The *stick–slip* fracture behavior was similar for all specimens and is in agreement with that observed previously on freshwater ice (DeFranco and Dempsey, 1990) and on cold sea and saline ice (Parsons et al., 1988, 1989; and DeFranco and Dempsey, 1993). In all cases the slope of the F-δ_{nt} curve is linear up to the initiation load where crack initiation occurs causing a crack jump, i.e., an unstably propagating crack, and a subsequent crack arrest at a lower load. It is interesting to note the similarity of the crack length and crack jump length between the individual specimens (Table 5.2) and that these coincide well with the theory (Figure 5.3 and Figure 5.4).

The fracture resistance K_R–curves for all specimens are shown in Figure 5.13. Immediately obvious from these curves is the overall decreasing trend of K_R with amount of crack growth. In other words, a negative K_R–curve is observed. However, there are two points that need to be specified concerning the interpretation of the test results: First, for a chevron notched geometry it is important to note that a stress–intensity–factor is not defined at $\alpha = \alpha_o$ due to the sharp apex of the notch, see Figure 5.1. Therefore, the load at the second abrupt load drop (shown as **B** in Figure 5.9a) is

#	E' (GPa)	$a/\Delta a$ (mm)	F (N)		K_R (kPa$\sqrt{\text{m}}$)	
			I	A	I	A
CNT1	10.9	112/0	1296		215	
		204/92		476		72
CNT2	15.4	154/0	737		97	
		212/58	481	437	74	68
		242/88	701	396	55	31
CNT4	10.0	146/0	579		78	
		165/19	621	525	82	70
		190/44	575	531	82	76
		201/55	704	525	106	79
		212/66	561	510	87	79
		226/80	575	525	89	81
		232/86	409	379	61	57
CNT5	9.1	146/0	553		74	
		164/18	550	390	73	52
		200/54	287	230	43	34
		217/71	162	155	25	24
		233/87	219	150	33	22
CNT6	11.4	152/0	441		59	
		154/2	634	415	84	55
		189/37	651	408	93	58
		217/65	333	333	52	52
		232/80	343	244	52	37
CNT7	10.9	126/0	979		142	
		220/94	447	447	70	70
		241/115	374	342	52	47

Note: I:initiation; A:arrest

Table 5.2: *CNT* fracture resistance results

used as the first initiation load F_I corresponding to the first K_R value in the plots in Figure 5.13. The first crack initiation event (shown as **A** in Figure 5.9a) corresponds to the load to generate an initial crack front width b. Typically, these first crack jumps were 40 mm long. Secondly, the practical limits of equation (5.6) for longer crack lengths is undetermined. By first analyzing all data it was found that for crack lengths longer than $\alpha \approx 0.85$ K_R decreased very steeply with increasing Δa leveling out at values in the order of 10 kPa$\sqrt{\text{m}}$, and in some cases, even less. This abrupt change of slope in the K_R– curve is not likely caused by any material behavior; instead, the range of validity for equation (5.6) was probably exceeded.

Due to these reasons; the first crack initiation event and all events occurring for relative crack lengths greater than $\alpha \approx 0.85$ are not included in this paper.

5.9 Conclusions

To overcome previous difficulties in obtaining stable cracking in freshwater ice, a new crack geometry was developed. The short rod Chevron Notched Tension (*CNT*) specimen was found to be extremely favorable in the sense of promoting stable *stick–slip* crack growth on freshwater ice at -16°C over a large portion of the uncracked ligament. Unstable fracture never occurred; the incremental crack extension took place along the whole notched ligament. For very long crack lengths ($\alpha \geq 0.85$) slow, almost continuous cracking with short crack jumps was observed. A characterization of the fracture resistance curve was therefore possible. In all cases, the slope of the F–δ_{nt} curve was linear up to the initiation load where crack initiation occurred causing a crack jump, i.e., an unstably propagating crack, and a subsequent crack arrest at a lower load. To re–initiate the crack again, a higher load was needed. However, the re–initiation loads declined with continued crack growth indicating a negative K_R versus Δa behavior as shown in Figure 5.13.

The brittle (cleavage) *stick–slip* fracture behavior was studied by fractography and is in agreement with that observed previously on

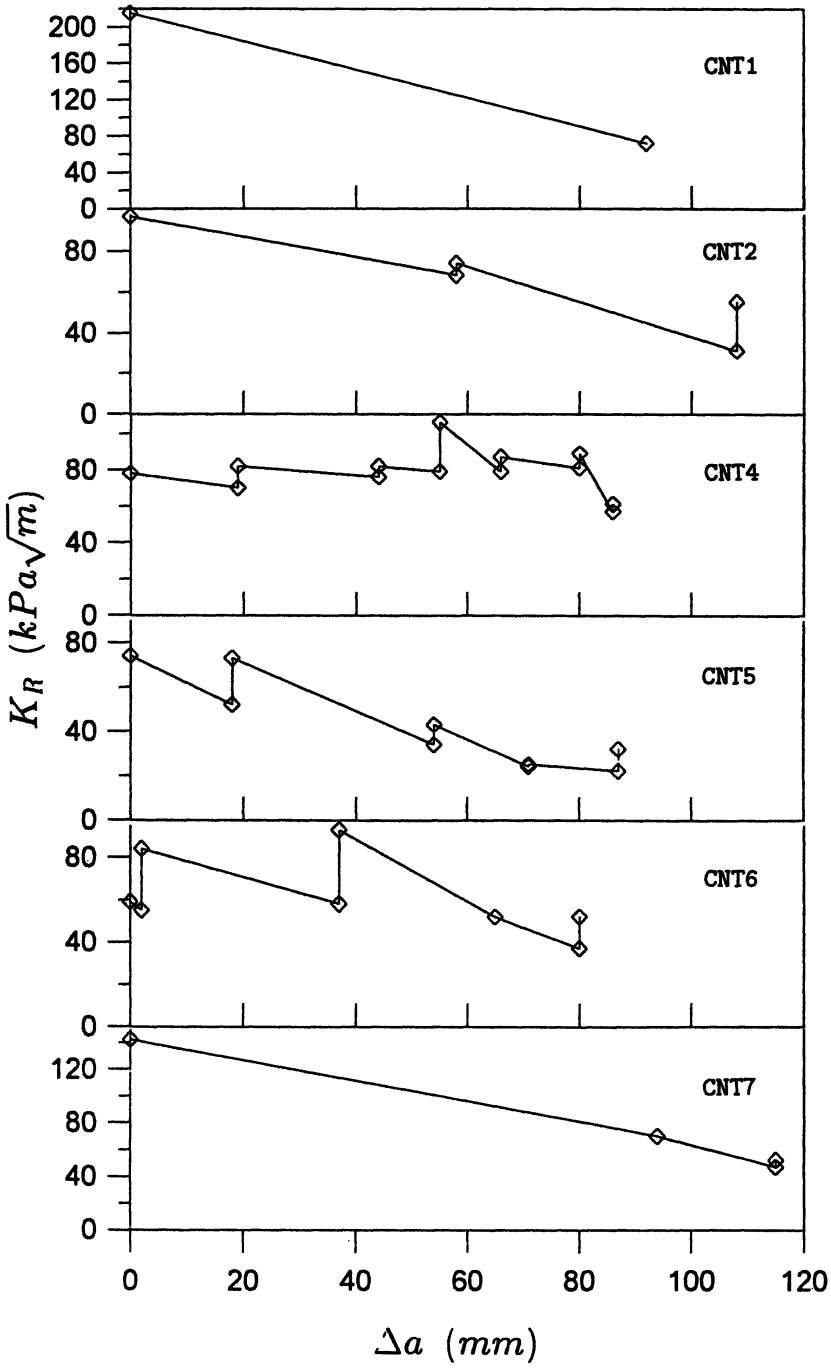

Figure 5.13: The K–resistance curves (fracture resistance, K_R, versus amount of crack growth, Δa) for freshwater ice at -16°C.

freshwater ice (DeFranco and Dempsey, 1990) and on cold sea and saline ice (Parsons et al., 1988, 1989; and DeFranco and Dempsey, 1993). The reasons that incremental cracking is observed on cold ice could be explained by the negative K_R–curve found in these tests. The difficulties of obtaining stability to date may be due to the inability of the previous fracture geometries (including possibilities of a too compliant loading system) to accommodate the negativity of the K_R–curve. However, the positive K_R–curve reported in DeFranco and Dempsey (1993) indicates that stable cracking in warm sea ice and saline ice (a model sea ice) may more easily be achieved.

Due to the large grain size, the specimen size range (Table 5.1) was probably not sufficient to reduce the scatter and ensure notch sensitivity and polycrystallinity.

References

Adamson R.M., Mulmule S. and Dempsey J.P., 1993. The SCB fracture geometry, *Int. J. Rock Mech. Min. Sci. & Geomech. Abstr.*, (submitted for publication).

ASTM E 399-85, 1985. Standard test method for plane–strain fracture toughness of metallic materials, *American Society for Testing and Materials Standards*, pp. 547–582.

Barker L.M., 1977. A simplified method for measuring plane strain fracture toughness, *Engineering Fracture Mechanics*, Vol. 9, pp. 361–369

Barker L.M., 1978., Short rod K_{Ic} measurements of Al_2O_3, *Fracture Mechanics of Ceramics*, Edited by Bradt R.C., Hasselman D.P.H. and Lange F.F, Vol. 3, pp. 483–494.

Bentley D.L., 1988.Fracture of freshwater and urea model ice, *Ph.D. Thesis*, Clarkson University, Potsdam, NY August 1988.

Bergdal L., 1978. Thermal Ice Pressure in Lake Ice Covers, *Ph.D. Thesis* Rep. Ser A:Z, Dept. Hydraulics, Chalmers University of Technology, Göteborg.

Billfalk L., 1982. Ice cover formation and brake up of solid covers on rivers, *Ph.D. Thesis*, no. 0349-4489:113, KTH, Stockholm.

Blanchet D.,1990. Ice design criteria for wide arctic structures, *Canadian Geotechnical Journal*, Vol. 27, pp. 701–725.

Blanchet, D. Churcher A.C., Fitzpatric J.P. and Badra-Blanchet P. 1989. An analysis of observed ice failure mechanisms for laboratory, first–year and multi year ice, Working Group on Ice Forces, 49th State-of-the-Art Report, U.S. Army Cold Regions Research and Engineering Laboratory, Hanover, NH, Special Report 89–5, pp. 77–124.

Broek D., 1986. Elementary engineering fracture mechanics, Martinus Nijhoff Publishers, Dordrecht 1986, p. 516,

Brown S.D., Biddulph R.B. and Wilcox P.D., 1964. A strength-porosity relation involving different pore geometry and orientation, *Journal of the American Ceramic Society*, Vol. 47, No. 7, pp. 320-322.

Bubsey R.T., Munz D., Pierce W.S. and Shannon Jr. J.L., 1982. Compliance calibration of the short rod chevron-notched specimen for fracture toughness testing on brittle materials, *International Journal of Fracture*, Vol. 18, No. 2, pp. 125-133.

Cederwall K, 1981. Behaviour of reinforced ice–cover with regard to creep, *proceedings of the 6th International Conference on Port and Ocean Engineering under Arctic Conditions, POAC-81*, Quebec, Vol. 1, pp. 562–570.

Cole D.M. and Gould L.D., 1990. Reversed direct–stress testing of ice: Equipment and examples results, *Cold Regions Science and Technology*, Vol. 18, No. 3, pp. 295–302.

Chong K.P., Kuruppu M.D. and Kuszmaul J.S. 1987a. Fracture toughness determination of rocks with core-based specimens, *SEM/RILEM International Conference on Fracture of Concrete and Rock*, Edited by Shah S.P. and Swartz S.E., pp. 3421–3428.

Chong K.P., Kuruppu M.D. and Kuszmaul J.S. 1987b. Fracture toughness determination of layerd materials, *Engineering Fracture Mechanics.*, Vol. 28, pp. 43–54.

Chong K.P. and Kuruppu M.D. 1988. Mixed mode fracture analysis using new semi–circular specimens, *Computers and Structtures*, Vol. 30, No. 4, pp. 905–908.

Cox G.F.N. and Weeks W.F., 1983. Equations for determining the gas and brine volumes in sea-ice samples, *Journal of Glaciology*, Vol. 29, No. 102, pp. 306-316.

Currier J.H. and Schulson E.M., 1982. The tensile strength of ice as a function of grain size, *Acta Metal.*, Vol. 30, pp. 1511-1514.

Danilenko, V.I. 1985. Determination of crack resistance (K_Ic) of freshwater ice, *Mechanics of Solids*, vol. 20, No. 5, pp.131–136.

DeFranco S. and Dempsey J.P., 1990. Crack growth stability in S2 ice, *Proceedings of the 10th IAHR International Symposium on Ice, IAHR-90*, Espoo, Vol. 1, pp. 168-181.

DeFranco S. and Dempsey J.P., 1991. Crack growth stability in saline ice, *Mechanics of Creep Brittle Materials 2*, Edited by Cocks A.C.F. and Ponter A.R.S., Elsevier Applied Science, New York, pp. 25-36.

DeFranco S. and Dempsey J.P., 1993. Crack propagation and fracture resistance in saline ice, *Journal of Glaciology*, (in press)

DeFranco S.J., Wei Y. and Dempsey J.P., 1991. Notch acuity effects on the fracture toughness of saline ice, *Annals of Glaciology*, No. 15, pp. 230-235.

Dempsey J.P., 1989. The fracture toughness of ice, *Ice-structure interaction, IUTAM Symposium St. John's*, Edited by S.J. Jones, R.F. McCenna, J. Tillotoson and I.J. Jordaan, Springer-Verlag, Berlin Heidelberg, 1991, pp. 109-145.

Dempsey J.P., Bentley D.L. and Sodhi D.S., 1986. Fracture toughness om model sea ice, *proceedings of the 8th IAHR International Symposium on Ice*, Vol. 1,pp. 365–376.

Dempsy J.P., Nigam D. and Cole D.M.,1988. The flexure and fracture of macrocrystalline S1 type freshwater ice, *Proceedings of the 7th International Conference on Offshore Mechanics and Arctic Engineering, OMAE 1988.*, Vol. IV, pp. 39–46.

Dempsey J.P. and Wei Y., 1989. Fracture toughness K_Q and fractography of S1 type freshwater ice, *Advances in Fracture Research*, edited by K. Salama, K. Ravi-Chandar, D.M.R. Taplin and P. Rama Rao, Vol. 5, pp. 3421-3428.

Dempsey J.P., Wei Y. and DeFranco S., 1990. Notch acuity effects on the CTOD and K_Q of ice, *Micromechanics of Failure of Quasi-Brittle Materials*, Edited by S.P. Shah, S.E. Swartz and M.L. Wang, Elsevier Applied Science, pp. 333-342.

Dempsey J.P., Wei Y. and DeFranco S.J., 1991. Fracture resistance to cracking in ice: Initiation and growth, *Proceedings of the 6th International Speciality Conference Cold Regions Engineering*, Edited by D.S. Sodhi , ASCE, New York, pp. 579–594.

Dempsey J.P., Wei Y. and DeFranco S.J., 1992. Notch sensitivity and brittleness in fracture testing of S2 columnar freshwater ice, *International Journal of Fracture*, Vol. 53, pp. 101-120.

Fransson L., 1984. Load-carrying Capacity of a Floating Ice Cover. Analytical Models and Experimental Studies of Natural Ice and of Ice Strengthened with Reinforcement. *Licentiate Thesis 1984:012L*, Division of Structural Engineering, LuleåUniversity of Technology, 137 p.

Fransson L. 1988. Thermal Ice Pressure on Structures in Ice Covers. *Ph.D. Thesis 1988:67D*, Division of Structural Engineering, LuleåUniversity of Technology, 161 p.

Fransson L., Stehn L., Åström L., Håkansson B. and Omstedt A., 1989a. Variations of ice properties in an ice area of 1x2 km in the Gulf of Bothnia, Mars 1988, *Proceedings of the 10th International Conference on Port and Ocean Engineering Under Arctic Conditions, POAC-89*, Luleå, Vol. III, pp. 1348-1357.

Fransson L., Stehn L., Åström L. and Danielsson G., 1989b. Ice strength of level ice, part of the Bothnian testing program of the icebreaker Oden, *Project Report 63223-2*, Division of Structural Engineering, Luleå University of Technology, Luleå, p. 20.

Fransson L., Olofsson T. and Sandqvist J., 1991. Observations of the failure process in ice blocks crushed by a flat indentor, *Proceedings of the 11th International Conference on Port and Ocean Engineering Under Arctic Conditions, POAC-91*, St. John's, Vol. 1, pp. 501-514.

Fransson L. and Stehn L., 1993. Porosity effects on measured strength of warm ice, *proceedings of the 12th International Conference on Port and Ocean Engineering under Arctic Conditions, POAC-93*, Hamburg, Vol. 1, pp. 23–36.

Goldstein R.V. and Osipenko N.M., 1991. Some questions on ice and ice cover fracture in compression, *Ice-structure interaction, IUTAM Symposium St. John's*, Edited by S.J Jones, R.F. McCenna, J. Tillotoson and I.J. Jordaan, Springer-Verlag, Berlin Heidelberg, 1991, pp. 251-266.

Gurney C. and Ngan K.M., 1971. Quasi static crack propagation in nonlinear structures, *Proceedings of the Transactions of the Royal Society*, London, Vol. A325, pp. 207-222.

Hillerborg A., Modeer M. and Petersson P.E., 1976. Analysis of crack formation and crack growth in concrete by means of fracture mechanics and finite elements, *Cement and Concrete Research*, Vol. 6, pp. 773-782.

Hui C.Y. and Riedel H., 1981. The asymptotic stress and strain field near the tip of a growing crack under creep conditions, *International Journal of Fracture*, Vol. 17, No. 4, pp. 409-425.

Ingraeffa A.R., 1984. Three dimensional finite-element analysis of chevron-notched fracture specimens, *Chevron-Notched Specimens*, edited by J.H. Underwood, S.W. Frieman and F.I. Baratta, ASTM Special Publication 855, Philadelphia, pp. 32-48.

ISRM, 1988. International Society for Rock Mechanics Commission on testing methods, suggested methods for determining the fracture toughness of rock, *Int. J. Rock Mech. Sci. & Geomech. Abstr.*, Vol. 25, No. 2, pp. 71-96.

Kanninen M.F. 1973. An augmented double cantilever beam model for studying crack propagation and arrest, *International Journal of Fracture.*, Vol. 9, No. 1, pp. 83–92.

Kennedy K.P., Blanchet D., Prodanovic A., Dempsey J.P., DeFranco S.J., Spencer P.A. and Masterson D.M., 1993. Large-scale ice fracture experiments:Phase1,*Proc. 12th Int. Conf. on Port and Ocean Eng. Under Arctic Conditions, POAC-93*, Hamburg, Vol. 2, pp. 527–536.

KnottJ.F., 1973. Fundamentals of Fracture Mechanics, Butterworth, London 1973, pp. 135

Knudsen F.P., 1959. Dependence of mechanical strength of brittle polycrystalline specimens on porosity and grain size, *Journal of the American Ceramic Society*, Vol. 42, No. 8, pp. 376-387.

Kollé J.J. 1981. Fracture toughness of ice; crystallographic anisotropy, *Proceedings of the 6th International Conference on Port and Ocean Engineering Under Arctic Conditions, POAC-81*, Vol. 1, pp. 366–374.

Kristic V.D. and Ericson W.H., 1987. A model for the porosity dependence of Young's modulus in brittle solids based on crack opening displacement, *Journal of Materials Science*, No. 22, pp. 2881-2886.

Langway C.C., 1958. Ice fabrics and the universal stage, Technical report 62, *(Snow Ice and Permafrost Research Establishment), U.S. Army Cold Regions Research and Engineering Laboratory*, Hanover, pp. 1–16.

Löfquist B., 1944. Lifting forces and bearing capacity of an ice cover. *Teknisk Tidskrift*, "4 juni 1944, pp.761–768.

Löfquist B., 1952. Ice pressure against dams. Studies of the effects

of temperature variations, *Americal Society of Civil Engineers*, Vol. 78, No. 160.

Mai Y-W., Atkins A.G. and Caddell R.M., 1975. On the stability of cracking in wedge tapered DCB specimens, *International Journal of Fracture*, Vol. 11, pp. 939-953.

Mai Y.W. and Atkins A.G., 1980. Crack stability in fracture toughness testing, *Journal of Strain Analysis*, Vol. 15, No. 2, pp. 63-74.

Matsuki K., Matsune S. and Takahasi H., 1991. Boundary element analysis for standard specimen configuration in the ISRM suggested methods for determining fracture toughness for rock, *Int. J. Rock Mech. Min. & Geomech. Abstr.*, Vol. 28, No. 5, pp. 355-363.

Mellor M., 1983. Mechanical behavior of sea ice, *CRREL Monograph No. 83-1*, 105 p.

Michel B. and Ramseier R.O., 1971. Classification of river and lake ice, *Canadien Geotechnical Journal*, Vol. 8, pp. 35–45.

Murakami Y., 1987. Stress intensity Factor Handbook, Vol. 1, Pergamon press.

Nixon W.A., 1984. Some aspects of the engineering properties of ice, Ph.D. Thesis, Cambridge University, U.K., Chapter 2, 67p.

Nixon W.A. and Smith R.A., 1987. The fracture toughness of some wood–ice composites, it Cold Regions Science and Technology, Vol. 14, pp. 139–145.

Ouchterlony F., 1982. Review of fracture toughness testing of rock, *Solid Mechanics Archives*, Vol. 7, pp. 131-211.

Ouchterlony F. 1984. Compliance calibration of a round fracture toughness bend specimen with chevron edge notch, *Report DS 1984:8, Swedish Detonic Research Foundation*, Stockholm, p 72.

Ouchterlony F., 1985. Evaluation formulas for rock fracture toughness testing with standard core specimens, *Report DS 1985:2, Swedish Detonic Research Foundation*, Stockholm, p. 82.

Ouchterlony F., 1989a. Fracture toughness testing of rock with core based specimens, the development of an ISRM standard, *Fracture Toughness and Fracture Energy-test methods for concrete*

and rock, edited by Mihasi H., Takahasi H. and Wittmann F.H., Balkema, Rotterdam, 1989, pp. 231-249.

Ouchterlony F., 1989b. On the background to the formulae and accuracy of rock fracture toughness measurements using ISRM standard core specimens, *Int. J. Rock Mech. Min. & Geomech. Abstr.*, Vol. 26, No. 1, pp. 13-23.

Parsons B.L., 1990. Behavior of ice in the brittle range–a review, *Proceedings of the 43rd Canadian Geotechnical Conference*, Vol. 1, pp. 377-386.

Parsons B.L., Snellen J.B. and Hill B. 1986. Physical modeling and the fracture toughness of sea ice, *Proceedings of the 5th International Conference on Offshore Mechanics and Arctic Engineering, OMAE 1986.*, Vol. IV, pp. 358–364.

Parsons B.L., Snellen J.B. and Hill B., 1987. Preliminary measurements of terminal crack velocity in ice, *Cold Regions Science and Technology*, Vol. 13, pp. 233-238.

Parsons B.L., Snellen J.B. and Muggeridge D.B., 1988. The initiation and arrest stress intensity factors of first year sea ice, *Proceedings of the 9th IAHR International Symposium on Ice, IAHR-88*, Sapporo, Vol. 1, pp. 502-512.

Parsons B.L., Snellen J.B. and Muggeridge D.B., 1989. The double torsion test applied to fine grained freshwater columnar ice and sea ice, *Mechanics of Creep Brittle Materials*, edited by Cocks A.C.F. and Ponter A.R.S., Elsevier Applied Science, pp. 188-200.

Parsons B.L., Williams F.M., Everad J. and Slade T., 1993. Notch sensitivity of first–year sea ice, *Journal of Engineering Mechanics*, Vol. 119, pp. 1303–1313.

Rice R.W., 1977. Microstructure dependence of mechanical behvior, *Properties and Microstructure, Treatsie on materials science and technology*, edited by R.K. MacCrone, Academic press, New York, 1977, Vol. 11, pp. 20-369.

Rice R.W., Freiman S.W., Pohanka R.C., Mecholsky J.J. and Wu C.Cm., 1978. Microstructural dependence of fracture mechanics parameters in ceramics, *Fracture Mechanics of Ceramics, Crack growth and Microstructure*, edited by R.C. Brandth, D.P.H. Has-

selman and F.F. Lange, Vol. 4, Plenum Press, New York, 1978, pp. 849-876.

Sanderson T.J.O., 1988. Ice mechanics–risks to offshore structures, *Graham and Trotman Ltd.*, London, 253 p.

Shannon Jr. J.L., Bubsey R.T. and Perce W.S., 1982. Extended range stress intensity factor expressions for chevron-notched short bar and short rod fracture toughness specimens, *International Journal of Fracture*, Vol. 19, No. 3, pp. R55-R58.

Shannon J.L. and Munz D.G., 1984. Specimen size and geometry effects on fracture toughness of aluminum oxide measured with short-rod and short-bar chevron-notched specimens, *Chevron-Notched Specimens*, edited by J.H. Underwood, S.W. Frieman and F.I. Baratta, ASTM Special Publication 855, Philadelphia, pp. 270-280.

Sigl L.S., 1991. On the stability of cracks in flexure specimens, *International Journal of Fracture*, No. 51, pp. 241-254.

Stehn L., 1990. Fracture toughness of sea ice, Development of a test system based on chevron notched specimens, *Licentiate thesis 1990:11L*, Division of Structural Engineering, Luleå University of Technology, Luleå, p. 88.

Stehn L., 1991. Fracture toughness of low salinity sea ice using short rod chevron notched specimens, *Proceedings of the 11th International Conference on Port and Ocean Engineering Under Arctic Conditions, POAC-91*, St. John's , Vol. I, pp. 541-555.

Stehn L., 1992. Fracturing and crack growth velocity of brackish sea ice, *Proceedings of the 11th IAHR International Symposium on Ice, IAHR-92*, Banff, Vol. 2, pp. 1155-1166.

Stehn L., 1993. Fracture toughness and crack growth of brackish ice using chevron notched specimens, *Journal of Glaciology*, (in press).

Stehn L. and Fransson L., 1989. A field instrument for fracture toughness testing on ice, *Proceedings of the 10th International Conference on Port and Ocean Engineering Under Arctic Conditions, POAC-89*, Luleå, Vol. I, pp. 300-310.

Stehn, L.M., DeFranco, S.J. and Dempsey, J.P. 1993a. Orientation effects on the fracture of pond (S1) ice, *International Journal of*

Rock Mechanics and Mining Science & Geomechanics Abstracts, (submitted for publication).

Stehn, L.M., DeFranco, S.J. and Dempsey, J.P. 1993b. Fracture resistance determination of freshwater ice using a chevron notched tension specimen. *International Journal of Fracture*, (submitted for publication).

Timco G.W. and Frederking R.M.W., 1982. Flexural strength and fracture toughness of sea ice, *Cold Regions Science and Technology*, Vol. 8, pp. 35-41.

Urabe N., Iwasaki T. and Yoshitake A., 1980. Fracture toughness of sea ice, *Cold Regions Science and Technology*, Vol. 3, pp. 29-37.

Urabe N. and Yoshitake A., 1981. strain rate dependent fracture toughness (K_{Ic}) of pure ice and sea ice, *Proceedings of the IAHR International Symposium on Ice, IAHR-81*, Quebec, Vol. 2, pp. 551-563.

Vaudery K.D., 1977. Ice engineering- study related properties of floating sea-ice and summary of elastic and viscoelastic analyses, *Technical Report No. R860*, Civil Engineering Laboratory, Port Hueneme, California 93043, p. 81.

Weber L.J. and Nixon W.A., 1991. Crack opening and propagation in S2 freshwater ice, *proceedings of the 10th International Conference on Offshore Mechanics and Arctic Engineering, OMAE, ASME*, Vol. IV, pp. 245–252.

Weeks W.F. and Ackley S.F., 1982. The growth, structure and properties of sea ice, *CRREL Monograph 82–1*, 130 p.

Wei Y. and Dempsey J.P., 1991. Dislocation movement at a crack tip of single crystals of ice, *Mechanics of Creep Brittle Materials 2*, edited by Cooks A.C.F. and Ponter A.R.S., Elsevier Applied Science, New York, pp. 62-74.

Wei Y. and Dempsey J.P., 1991b. Fractographic examinations of fracture in polycrystalline S2 ice, *Journal of materials science*, Vol. 26, pp. 5733–5740.

Wei Y., DeFranco S.J. and Dempsey J.P. 1991. Crack fabrication techniques and their effects on the fracture toughness and CTOD for freshwater columnar ice, *Journal of Glaciology*, Vol. 37, pp.

270–280.

Wu E.M., 1967. Application of fracture mechanics to anisotropic plates, *Journal of Applied Mechanics*, Vol. 34, No. 4, pp. 967–974.

Doctoral and Licentiate Theses from the Division of Structural Engineering.
Luleå University of Technology

Doctoral Theses

1980 Ulf Arne Girhammar: Dynamic Fail-safe Behaviour of Steel Structures. *Doctoral Thesis 1980:06D, 309 p.*

1983 Kent Gylltoft: Fracture Mechanics Models for Fatigue in Concrete Structures. *Doctoral Thesis 1983:25D, 210 p.*

1988 Lennart Fransson: Thermal Ice Pressure on Structures in Ice Covers. *Doctoral Thesis 1988:67D, 161 p.*

1989 Mats Emborg: Thermal Stresses in Concrete Structures at Early Ages. *Doctoral Thesis 1989:73D, 2nd Ed, 1990, 285 p.*

1993 Lars Stehn: Tensile Fracture of Ice, Test Methods and Fracture Mechanics Analysis*Doctoral Thesis 1993:129D, 136 p.*

Licentiate Theses

1984 Lennart Fransson: Bärförmåga hos ett flytande istäcke. Beräkningsmodeller och experimentella studier av naturlig is och av is förstärkt med armering. (Load-carrying Capacity of a Floating Ice Cover. Analytical Models and Experimental Studies of Natural Ice and of Ice Strengthened with Reinforcement.) *Licentiate Thesis 1984:012L, 2nd Ed, 1988, 137 p.*

1985 Mats Emborg: Temperature Stresses in Massive Concrete Structures. Viscoelastic Models and Laboratory Tests. *Licentiate Thesis 1985:011L, 2nd Ed, 163 p.*

1987 Christer Hjalmarsson: Effektbehov i bostadshus. Experimentell bestämning av effektbehov i små- och flerbostadshus. (Heating Demand in Single and Multi Family Houses. A Comparison of Models for Calculation and Methods for Measurements.) *Licentiate Thesis 1987:009L, 72 p.*

1990 Björn Täljsten: Förstärkning av betongkonstruktioner genom pålimning av stålplåtar. (Concrete Structures Strengthened by Externally Bonded Steel Plates). *Licentiate Thesis 1990:06L, 205 p.*

1990 Ulf Ohlsson: Fracture Mechanics Studies of Concrete Structures. *Licentiate Thesis 1990:07L, 66 p.*

1990 Lars Stehn: Fracture Toughness of Sea Ice. Development of a Test System Based on Chevron Notched Specimens. *Licentiate Thesis 1990:11L, 88 p.*

1992 Per Anders Daerga: Some Experimental Fracture Mechanics Studies in Mode I of Concrete and Wood. *Licentiate Thesis 1992:12L, 2nd Ed, 76 p.*

1993 Henrik Gabrielsson: Shear Capacity of Beams of Reinforced High Performance Concrete. *Licentiate Thesis 1993:21L, 111 p.*

Rock Mechanics and Mining Science & Geomechanics Abstracts, (submitted for publication).

Stehn, L.M., DeFranco, S.J. and Dempsey, J.P. 1993b. Fracture resistance determination of freshwater ice using a chevron notched tension specimen. *International Journal of Fracture*, (submitted for publication).

Timco G.W. and Frederking R.M.W., 1982. Flexural strength and fracture toughness of sea ice, *Cold Regions Science and Technology*, Vol. 8, pp. 35-41.

Urabe N., Iwasaki T. and Yoshitake A., 1980. Fracture toughness of sea ice, *Cold Regions Science and Technology*, Vol. 3, pp. 29-37.

Urabe N. and Yoshitake A., 1981. strain rate dependent fracture toughness (K_{Ic}) of pure ice and sea ice, *Proceedings of the IAHR International Symposium on Ice, IAHR-81*, Quebec, Vol. 2, pp. 551-563.

Vaudery K.D., 1977. Ice engineering- study related properties of floating sea-ice and summary of elastic and viscoelastic analyses, *Technical Report No. R860*, Civil Engineering Laboratory, Port Hueneme, California 93043, p. 81.

Weber L.J. and Nixon W.A., 1991. Crack opening and propagation in S2 freshwater ice, *proceedings of the 10th International Conference on Offshore Mechanics and Arctic Engineering, OMAE, ASME*, Vol. IV, pp. 245–252.

Weeks W.F. and Ackley S.F., 1982. The growth, structure and properties of sea ice, *CRREL Monograph 82–1*, 130 p.

Wei Y. and Dempsey J.P., 1991. Dislocation movement at a crack tip of single crystals of ice, *Mechanics of Creep Brittle Materials 2*, edited by Cooks A.C.F. and Ponter A.R.S., Elsevier Applied Science, New York, pp. 62-74.

Wei Y. and Dempsey J.P., 1991b. Fractographic examinations of fracture in polycrystalline S2 ice, *Journal of materials science*, Vol. 26, pp. 5733–5740.

Wei Y., DeFranco S.J. and Dempsey J.P. 1991. Crack fabrication techniques and their effects on the fracture toughness and CTOD for freshwater columnar ice, *Journal of Glaciology*, Vol. 37, pp.

270–280.

Wu E.M., 1967. Application of fracture mechanics to anisotropic plates, *Journal of Applied Mechanics*, Vol. 34, No. 4, pp. 967–974.

Doctoral and Licentiate Theses from the Division of Structural Engineering.
Luleå University of Technology

Doctoral Theses

1980 Ulf Arne Girhammar: Dynamic Fail-safe Behaviour of Steel Structures. *Doctoral Thesis 1980:06D, 309 p.*

1983 Kent Gylltoft: Fracture Mechanics Models for Fatigue in Concrete Structures. *Doctoral Thesis 1983:25D, 210 p.*

1988 Lennart Fransson: Thermal Ice Pressure on Structures in Ice Covers. *Doctoral Thesis 1988:67D, 161 p.*

1989 Mats Emborg: Thermal Stresses in Concrete Structures at Early Ages. *Doctoral Thesis 1989:73D, 2nd Ed, 1990, 285 p.*

1993 Lars Stehn: Tensile Fracture of Ice, Test Methods and Fracture Mechanics Analysis*Doctoral Thesis 1993:129D, 136 p.*

Licentiate Theses

1984 Lennart Fransson: Bärförmåga hos ett flytande istäcke. Beräkningsmodeller och experimentella studier av naturlig is och av is förstärkt med armering. (Load-carrying Capacity of a Floating Ice Cover. Analytical Models and Experimental Studies of Natural Ice and of Ice Strengthened with Reinforcement.) *Licentiate Thesis 1984:012L, 2nd Ed, 1988, 137 p.*

1985 Mats Emborg: Temperature Stresses in Massive Concrete Structures. Viscoelastic Models and Laboratory Tests. *Licentiate Thesis 1985:011L, 2nd Ed, 163 p.*

1987 Christer Hjalmarsson: Effektbehov i bostadshus. Experimentell bestämning av effektbehov i små- och flerbostadshus. (Heating Demand in Single and Multi Family Houses. A Comparison of Models for Calculation and Methods for Measurements.) *Licentiate Thesis 1987:009L, 72 p.*

1990 Björn Täljsten: Förstärkning av betongkonstruktioner genom pålimning av stålplåtar. (Concrete Structures Strengthened by Externally Bonded Steel Plates). *Licentiate Thesis 1990:06L, 205 p.*

1990 Ulf Ohlsson: Fracture Mechanics Studies of Concrete Structures. *Licentiate Thesis 1990:07L, 66 p.*

1990 Lars Stehn: Fracture Toughness of Sea Ice. Development of a Test System Based on Chevron Notched Specimens. *Licentiate Thesis 1990:11L, 88 p.*

1992 Per Anders Daerga: Some Experimental Fracture Mechanics Studies in Mode I of Concrete and Wood. *Licentiate Thesis 1992:12L, 2nd Ed, 76 p.*

1993 Henrik Gabrielsson: Shear Capacity of Beams of Reinforced High Performance Concrete. *Licentiate Thesis 1993:21L, 111 p.*